Professional Report 126

THE ~400 YR B.P. ERUPTION OF HALF CONE, A POST-CALDERA COMPOSITE CONE WITHIN ANIAKCHAK CALDERA, ALASKA PENINSULA

Brandon L. Browne, Christina Neal, and Charles R. Bacon

Published by
STATE OF ALASKA
DEPARTMENT OF NATURAL RESOURCES
DIVISION OF GEOLOGICAL & GEOPHYSICAL SURVEYS
2022

THE ~400 YR B.P. ERUPTION OF HALF CONE, A POST-CALDERA COMPOSITE CONE WITHIN ANIAKCHAK CALDERA, ALASKA PENINSULA

Brandon L. Browne, Christina Neal, and Charles R. Bacon

Professional Report 126

State of Alaska
Department of Natural Resources
Division of Geological & Geophysical Surveys

STATE OF ALASKA
Mike Dunleavy, Governor

DEPARTMENT OF NATURAL RESOURCES
Corri A. Feige, Commissioner

DIVISION OF GEOLOGICAL & GEOPHYSICAL SURVEYS
David L. LePain, State Geologist and Director

Publications produced by the Division of Geological & Geophysical Surveys (DGGS) are available for free download from the DGGS website (dggs.alaska.gov). Publications on hard-copy or digital media can be examined or purchased in the Fairbanks office:

Alaska Division of Geological & Geophysical Surveys
3354 College Rd., Fairbanks, Alaska 99709-3707
Phone: (907) 451-5010 Fax (907) 451-5050
dggspubs@alaska.gov | dggs.alaska.gov

DGGS publications are also available at:
Alaska State Library,
Historical Collections & Talking Book Center
395 Whittier Street
Juneau, Alaska 99811

Alaska Resource Library and Information Services (ARLIS)
3150 C Street, Suite 100
Anchorage, Alaska 99503

Suggested citation:
Browne, B.L., Neal, C.A., and Bacon, C.R., 2022, The ~400 yr B.P. eruption of Half Cone, a post-caldera composite cone within Aniakchak caldera, Alaska Peninsula: Alaska Division of Geological & Geophysical Surveys Professional Report 126, 60 p. https://doi.org/10.14509/30839

Cover. Photograph from the southwest Aniakchak caldera rim looking northeast at the steep, ~300-m-high exposure through Half Cone. Light tan tephra and dark gray vent-filling lava flows (middle cliffs) from pre-400 yr BP Half Cone eruptions are overlain by reddish orange and black pyroclastic deposits from the ~400 yr B.P. eruption. The blocky surface of the Cobweb lava flow, mantled by 1931 tephra, lies to the right of Half Cone on the floor of Aniakchak caldera. Older Aniakchak edifice volcanic rocks are in the foreground and background. Photo: Neal, C. A., USGS-AVO.

Contents

Introduction 2
Geologic Setting 3
Geologic History 5
Methods 9
Stratigraphy of the ~400 yr B.P. Eruption 10
    Proximal Tephra Stratigraphy 12
    Tephra Stratigraphy Within Aniakchak Caldera 16
    Tephra Stratigraphy Outside Aniakchak Caldera 20
    Dispersal of Half Cone Tephra 21
    The Cobweb Lava Flow and Cobweb Tuff Cone 24
Whole-Rock Geochemistry 24
Petrography and Mineral and Glass Compositions 31
    Petrography and Plagioclase Compositions 31
    Glass Compositions 40
Discussion 42
    Volume Calculations for the Half Cone Eruption 42
    Titanomagnetite and Ilmenite Geothermometry 44
    Pre-Eruption Storage Conditions of the ~400 yr B.P. Half Cone Magmas 46
    Eruption Chronology 48
Summary 53
Acknowledgments 54
References 56

Figures

Figure 1. Earthstar Geographics image of the Alaska Peninsula showing Kodiak Island, the Aleutian trench, the North American Plate, the Pacific Plate, and historically active volcanoes including Aniakchak volcano 4
Figure 2. Simplified geologic map of Aniakchak caldera 6
Figure 3. Photos of Cobweb lava flow and Cobweb tuff cone 8
Figure 4. Photographs of typical pyroclasts from the Pink Pumice and Brown Pumice phases of the ~400 yr B.P. eruption 12
Figure 5. Scanning electron microscope images of Pink Pumice and Brown Pumice pyroclasts 13
Figure 6. Photographs of upper Half Cone walls 14
Figure 7. Annotated and measured stratigraphic columns with scale bars of accessible ~400 yr B.P. tephra at locations 2 and 4 along the Half Cone walls 15
Figure 8. Field photos showing characteristics of Pink Pumice and Brown Pumice deposits located within and outside Aniakchak caldera 17
Figure 9. Annotated and measured stratigraphic columns of ~400 yr B.P. tephra at locations 1 and 7 19
Figure 10. Annotated and measured stratigraphic columns of ~400 yr B.P. tephra at locations 18a, 15, 14, and 27 21
Figure 11. Isopach and isopleth contours of the Pink Pumice and Brown Pumice fall layers 22
Figure 12. Weight percent major element concentrations of Pink Pumice and Brown Pumice, Cobweb lava flow and Cobweb tuff cone, as well as pre-400 yr B.P. Half Cone lavas and tephra 25
Figure 13. Major element concentrations of samples plotted against SiO_2 wt% from ~400 yr B.P. and pre-400 yr B.P. Half Cone lavas and tephra 26
Figure 14. Trace element concentrations of tephra and lava samples plotted against Zr from ~400 yr B.P. and pre-400 yr B.P. Half Cone lavas and tephra 28

Figure 15. Major element concentrations measured by XRF of tephra and lava samples plotted as a function of relative stratigraphic order 29
Figure 16. Trace element concentrations of samples measured by XRF and ICP-MS plotted as a function of relative stratigraphic order 30
Figure 17. Photomicrographs of Pink Pumice pyroclasts 32
Figure 18. Photomicrographs of Brown Pumice pyroclasts 33
Figure 19. Representative back-scattered electron images of plagioclase types 35
Figure 20. Rim and core anorthite compositions of plagioclase crystals by electron microprobe analyses relative to ~400 yr B.P. stratigraphy 36
Figure 21. Core to rim composition transects of plagioclase with corresponding backscattered electron images of crystals from Pink Pumice pyroclasts 37
Figure 22. Core to rim transects of plagioclase via electron microprobe with corresponding back-scattered electron images of crystals from Brown Pumice and Cobweb lava flow 38
Figure 23. Photomicrographs of the Cobweb lava flow 39
Figure 24. Anhydrous major element compositions of matrix glasses in pyroclasts from the Pink Pumice and Brown Pumice from proximal locations 1 and 2 41
Figure 25. Approximate isopach contours of the combined Pink Pumice and Brown Pumice fall layers 43
Figure 26. Calculated pre-eruptive equilibrium temperatures versus log fO_2 45
Figure 27. The area within isopleth contours versus average of maximum lithic diameters from tephra samples for eruption column heights between 5 and 25 km 48

Tables

Table 1. Radiocarbon dates constraining post-caldera tephra fall deposits from Aniakchak volcano 11
Table 2. Volumes of tephra and magma produced during the ~400 yr B.P. Half Cone eruption phases 44

Appendices

The following appendices are available to download at: doi.org/10.14509/30839

Appendix A: Sample metadata with locations and descriptions of pyroclastic samples
Appendix B: Sample metadata with locations, descriptions, and thicknesses of pyroclastic samples
Appendix C: Locations, descriptions, and whole-rock geochemistry values from rock samples
Appendix D: Locations, descriptions, and electron microprobe analyses of plagioclase from rock samples
Appendix E: Locations, descriptions, and electron microprobe analyses of pyroxene from rock samples
Appendix F: Locations, descriptions, and electron microprobe analyses of magnetite and ilmenite from rock samples
Appendix G: Locations, descriptions, and electron microprobe analyses of matrix glass from pyroclastic samples

THE ~400 YR B.P. ERUPTION OF HALF CONE, A POST-CALDERA COMPOSITE CONE WITHIN ANIAKCHAK CALDERA, ALASKA PENINSULA

Brandon L. Browne[1,2], Christina Neal[3], and Charles R. Bacon[4]

ABSTRACT

Aniakchak volcano is a historically active caldera located on the central Alaska Peninsula. The largest eruption from Aniakchak volcano since the ~3,400 yr B.P. caldera-forming eruption occurred ~400 yr B.P. from Half Cone volcano, an intracaldera composite cone on the northwest floor of the Aniakchak caldera that was largely destroyed by the eruption. The ~400 yr B.P. eruption produced widely dispersed pumice fall deposits known as the Pink Pumice and Brown Pumice. Following small phreatomagmatic explosions, a buoyant Plinian eruption column combined with southwesterly winds dispersed ~1.3 km^3 of crystal-poor dacite (66.1–67.1% SiO_2) Pink Pumice to the northeast from Half Cone (~0.3 km^3 dense rock equivalent; DRE). Fluctuations in the diameters of pyroclasts and accidental lithics in the Pink Pumice indicate at least two cycles of waxing and waning mass flux at the Half Cone vent. This vent produced an eruption column that twice expanded and gained altitudes of ~15–20 km before weakening to lower altitudes. Brown Pumice scoria (58.2–66.9% SiO_2) as well as compositionally banded pyroclasts at the top of the Pink Pumice indicate that both dacite magma and an increasing amount of low-SiO_2 (58.2–60.5% SiO_2) andesite magma were erupted simultaneously during the transition to the Brown Pumice phase of the eruption. The reversely graded Brown Pumice fall deposit records an escalating Plinian column dominated by low-SiO_2 Brown Pumice scoria that reached altitudes of ~20–24 km and led to the emplacement of least ~3.5 km^3 of fall deposits up to at least 230 km to the northeast (~1 km^3 DRE). Over time, the Brown Pumice eruption column repeatedly experienced partial collapse that ultimately produced thick pyroclastic density current deposits, most of which were confined to within the caldera. Lithic-rich agglutinate and spatter exposed in 60-m-thick deposits atop the severed flanks of Half Cone and within ~2 km of Half Cone were emplaced at the end of the Brown Pumice phase. Agglutinate deposits range from 58.6 to 64.8% SiO_2, which generally falls in the compositional range between Brown Pumice and Pink Pumice compositional endmembers. Most of the Half Cone edifice was destroyed by the end of the Brown Pumice phase. The ~0.1 km^3 crystal-rich dacitic Cobweb lava flow (64.8–65.8% SiO_2) filled a basin left behind by the destruction of Half Cone as a series of radiating lobes. Subsequently, a small andesitic tuff cone (62.2–62.8% SiO_2) formed over the Cobweb lava flow vent. In all, we estimate that at least ~5.4 km^3 of tephra and ~0.1 km^3 of lava erupted during the ~400 yr B.P. eruption, yielding a total magmatic volume (DRE) of ~1.5 km^3. Titanomagnetite-ilmenite pairs in Pink Pumice and Brown Pumice samples record similar equilibrium temperature ranges (944–997 °C and 959–985 °C, respectively) but different fO_2 conditions—Pink Pumice pairs plot between NNO and

[1]Alaska Volcano Observatory, Alaska Division of Geological & Geophysical Surveys, 3354 College Road, Fairbanks, Alaska 99709
[2]Department of Geology, Humboldt State University, 1 Harpst Street, Arcata, CA 95521
[3]U.S. Geological Survey, Volcano Science Center, Alaska Volcano Observatory, 4210 University Drive, Anchorage, Alaska 99508
[4]U.S. Geological Survey, California Volcano Observatory, 345 Middlefield Road, Menlo Park, CA 94025-3561

NNO +0.5, Brown Pumice pairs plot below the NNO buffer. Titanomagnetite-ilmenite pairs in Brown Pumice agglutinate record a wider range of temperatures than either Pink Pumice or Brown Pumice samples (899–1018 °C) but also show two populations of fO_2—one that overlaps the Pink Pumice array at higher fO_2 and one that overlaps the Brown Pumice array at lower fO_2. Titanomagnetite-ilmenite pairs from the Cobweb lava flow have the largest fO_2 range (NNO -0.5 to NNO +0.5), although most pairs overlap Brown Pumice samples at lower fO_2 conditions near NNO -0.5. Pairs in Cobweb lava flow samples record temperatures from 837 to 1054 °C, which is the largest temperature range recorded in deposits emplaced during any phase of the ~400 yr B.P. eruption. Geothermometry results of titanomagnetite-ilmenite pairs in ≤3,400 yr B.P. samples erupted from Aniakchak volcano record a similar temperature range and the presence of two fO_2 arrays as the ~400 yr B.P. samples, which implies the existence of two magma regions of the mush column; each the product of slightly different evolution. In addition, results from *in situ* compositional analyses of plagioclase suggest that the ~400 yr B.P. eruption may have been initiated, at least in part, by intrusion of basaltic magma, which ascended from the lower crust into the shallow subvolcanic magma mush column prior to and during eruption. The bimodal distribution of whole-rock compositions and the two plagioclase populations in the low-SiO_2 Brown Pumice—one defined by An_{40}–An_{60} cores and one defined by An_{79}–An_{95} cores—is consistent with an abbreviated period of mixing between intruding basalt and resident dacite mush prior to eruption. Progressive mixing between mafic and felsic magmas during and after the eruption likely produced the subsequently erupted Cobweb lava flow, which has an intermediate composition with abundant mineral disequilibria. Aniakchak volcano continues to show episodic signs of unrest, suggesting that eruptions will occur in the future.

INTRODUCTION

Aniakchak volcano is a historically active caldera located near Port Heiden on the Alaska Peninsula. Several Holocene eruptions have occurred from Aniakchak volcano, including two large caldera-forming eruptions—one between ca. 9,500 and 7,000 years ago (Bacon and others, 2014) and the other 3,400 ^{14}C yr B.P. (Miller and Smith, 1987)—the latter of which resulted in the current ~10-km-diameter and 0.5–1.0-km-deep caldera (Smith, 1925). Since the 3,400-yr B.P. eruption, at least a dozen separate vents within the caldera have erupted—often explosively—producing both lava flows and widespread tephra deposits that blanketed southwestern Alaska and the upper Alaska Peninsula with ash (Hubbard, 1932b; Kienle and Swanson, 1983; Riehle and others, 1987, 2000; Begét and others, 1992; Neal and others, 2001; Browne and others, 2006; Nicholson and others, 2011; Bacon and others, 2014). Two notable post-caldera eruptions include the ~400 yr B.P. eruption from Half Cone, a crescent-shaped remnant of an intracaldera composite cone located along the northwest edge of the Aniakchak caldera floor, and the 1931 eruption from intracaldera vents situated inboard of the western caldera wall. The ~400 yr B.P. Half Cone eruption is the largest post-caldera eruption yet identified from Aniakchak volcano, while the 1931 eruption is the most recent eruption from Aniakchak volcano and one of the largest in Alaska during the last 100 years (Hubbard, 1932b; Neal and others, 2001; Nicholson and others, 2011). Our goals for this study are to (1) describe the dispersal and volume of the ~400 yr B.P. Half Cone eruption based on stratigraphic characteristics of

the resulting deposits, (2) evaluate the pre-eruption storage conditions of magmas expelled during the ~400 yr B.P. Half Cone eruption based on both whole-rock geochemical analyses of juvenile material and *in situ* geochemical analyses of mineral and glass regions of deposits, and (3) synthesize stratigraphic and geochemical observations into a chronology for the ~400 yr B.P. eruption.

GEOLOGIC SETTING

Aniakchak volcano is located ~670 km southwest of Anchorage on the Alaska Peninsula, a narrow platform that divides the Bering Sea from the Pacific Ocean in southwest Alaska (fig. 1). This region is the original homeland of the Alutiiq/Sugpiaq people, who have inhabited the coastal environments of southcentral Alaska and the Alaska Peninsula for over 7,000 years (Ringsmuth, 2007). The peninsula stretches for 600 km from near Kukaklek Lake in Katmai National Park and Preserve in the northeast where it is ~170 km wide to Bechevin Bay in the southwest where it is less than 10 km wide (fig. 1). Beyond Bechevin Bay, the Alaska Peninsula transitions to the Aleutian Islands, a 2,500-km-long volcanic island archipelago that extends west from mainland Alaska toward Kamchatka. The Pacific coast of the Alaska Peninsula is characterized by steep-sided and glaciated stratovolcanoes perched above rugged, glacially carved inlets that expose underlying Tertiary and Mesozoic sedimentary rocks (Detterman and others, 1996). In contrast, the Bering Sea coast of the Alaska Peninsula is a flat plain with broad beaches that have been blanketed repeatedly by glacial and pyroclastic deposits (Detterman and others, 1996; Neal and others, 2001; Dreher and others, 2005; Bacon and others, 2014). Settlements on the Alaska Peninsula occur as small communities located almost exclusively along the Bering Sea or Pacific coasts. Port Heiden, located 25 km west where the Meshik River enters the Bering Sea, and Chignik, located 60 km southwest within Chignik Bay on the Pacific coast, are the nearest inhabited areas to Aniakchak volcano.

Southwest of Aniakchak volcano are Black Peak volcano, a glacially eroded stratovolcano with a small Holocene caldera and lava dome complex, and Veniaminof volcano, a large, frequently active ice-filled caldera that last erupted in 2021. Northeast of Aniakchak volcano are Yantarni volcano, a stratovolcano known for its similar size and morphology to Mount St. Helens in Washington State, and Chiginagak volcano, a small glacially covered stratovolcano known for its acidified summit lake that periodically discharges as noxious mudflows that impact the adjacent watershed and annual salmon runs (Schaefer and others, 2008). Like other volcanic centers in the Aleutian Arc, magmas erupted from Aniakchak volcano result from ongoing subduction of the Pacific Plate beneath the North American Plate, which occurs at a rate of 65 mm/year (Syracuse and Abers, 2006) based on calculated convergence velocities from magnetic lineations (DeMets and others, 1994). Aniakchak volcano is situated atop continental crust approximately 100 km (Syracuse and Abers, 2006) above the upper surface of the subducting Pacific Plate and ~300 km to the northwest of the trench where the Pacific and North American plates come in contact and periodically slip past each other generating powerful earthquakes and tsunamis (e.g., Shennan and others, 2009).

A background discussion of Aniakchak volcano would not be complete without mentioning Father Bernard Hubbard (1888–1962), a geology professor and Jesuit priest from Santa Clara University in California. Along with his photos and films, his exciting writings of Aniakchak volcano's stark beauty as well as his vivid descriptions of what he saw as an uninhabited, treacherous, and moon-like landscape during visits in 1930, 1931, and 1932 led to its widespread popularity in American culture (Hubbard, 1931, 1932a; Douglas, 1932). Subsequent work contradicts Father Hubbard's description of the Aniakchak region as being devoid of human activity, as it has since been established that the first humans arrived on the Alaska Peninsula some 9,000 years ago and, by ~7,000 years ago, had established numerous communities on the peninsula and adjacent Kodiak Island (e.g., Henn, 1978; Dumond, 1987a, 1987b; Ringsmuth, 2007; VanderHoek and

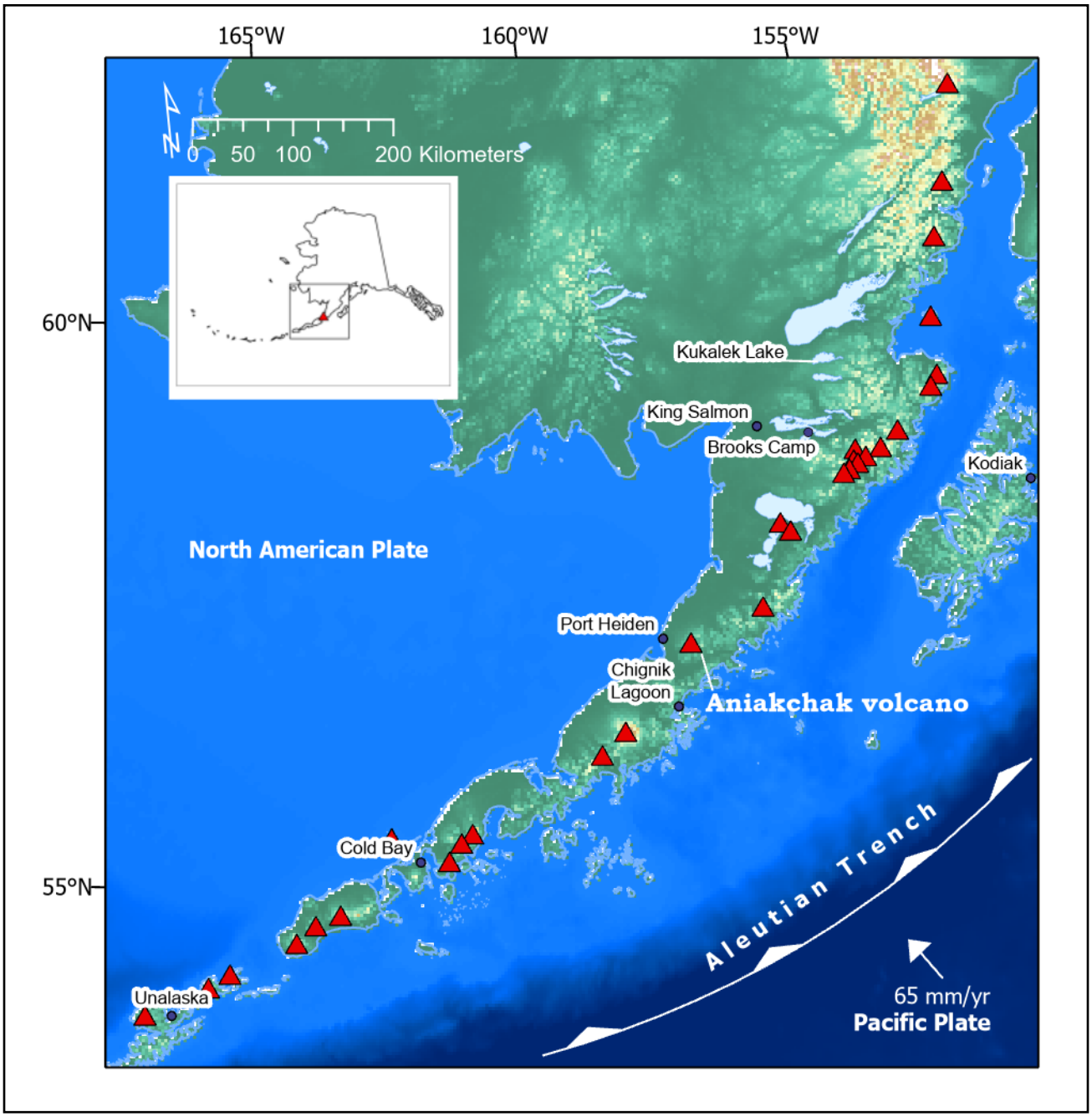

Figure 1. Map of the Alaska Peninsula showing Kodiak Island, the Aleutian trench, the North American Plate, the Pacific Plate, and historically active volcanoes (red triangles) including Aniakchak volcano. The white arrow indicates the direction and speed of the Pacific Plate (from DeMets and others, 1994; Syracuse and Abers, 2006). Communities and place names of lakes, oceans, and inlets described in the text are also included. Brooks Camp is located within the Brooks River Archeological District within Katmai National Park and Preserve described by Dumond (1987b) and Riehle and others (2000).

Myron, 2004; VanderHoek and Nelson, 2007). However, his adventurous "glacier priest" persona and public enthusiasm for Aniakchak volcano were influential in establishment of the ~2,500-km^2 Aniakchak National Monument and Preserve in 1980 (Ringsmuth, 2007). In addition, Hubbard's documentation of Aniakchak volcano's only historical eruption in 1931 provided a valuable timeline and description of eruption processes that were later used to advance our scientific understanding

of volcanic activity and hazards at Aniakchak volcano (Hubbard, 1932b; Neal and others, 2001; Nicholson and others, 2011; Bacon and others, 2014; this study).

GEOLOGIC HISTORY

The oldest known eruptions of Aniakchak volcano occurred approximately 850,000 years ago (Nye and others, 1997). Lava flows and pyroclastic deposits from these Pleistocene eruptions range from basaltic andesite to dacite and are now exposed in cross section within glaciated valleys and caldera walls that formed in the Holocene (Qv in fig. 2; George and others, 2004). The detailed Holocene evolution of the volcano based on studies by Bacon and others (1997), Nye and others (1995, 1997), Bacon (2000, 2002), Neal and others (2001), and Bacon and others (2014) are summarized below.

The Aniakchak I ignimbrite (Qa1 in fig. 2) records the oldest documented Holocene explosive eruption from Aniakchak volcano. This andesitic ignimbrite consists of pyroclastic density current and fall deposits that occur as nonwelded deposits in low-lying valleys and welded ignimbrite and fall deposits at higher elevation atop the volcano flanks. The Aniakchak I ignimbrite was emplaced between ca. 9,500 and ca. 7,000 yr B.P. (Bacon and others, 2014; VanderHoek, 2009; VanderHoek and Myron, 2004). Following the Aniakchak I eruption are deposits from ca. 7,000 yr B.P. Plinian eruptions that produced a package of volcanic rocks including rhyodacite lava, pumice fall, and ignimbrite known as the Black Nose Pumice. Several additional Holocene eruptions occurred after the Black Nose Pumice and before the Aniakchak II (ANI II) caldera-forming eruption.

The dominant feature of Aniakchak volcano is the ~10-km-diameter and 0.5–1.0-km-deep caldera (Smith, 1925) that formed during the catastrophic 3,430 ^{14}C yr B.P. Aniakchak II eruption (Miller and Smith, 1987). Approximately 14 km^3 DRE of rhyodacite (67–70 wt% SiO_2) and 13 km^3 DRE of andesite (57–60 wt% SiO_2) magma were erupted during the Aniakchak II eruption (Miller and Smith, 1987; Begét and others, 1992; Dreher and others, 2005). Resulting fall deposits have been identified in Greenland ice cores (Pearce and others, 2004), while ignimbrite extends up to 80 km from the caldera and fills adjacent valleys to a thickness of up to 75 m (Miller and Smith, 1977, 1987). The ignimbrite is compositionally stratified with layers characterized from base to top by rhyodacite, rhyodacite and andesite, and andesite pumice clasts, which form sharp contacts within exposed sections (Dreher and others, 2005). Interestingly, although banded pumices exist in the ignimbrite, no true hybrid compositions indicative of mixing between the andesite and rhyodacite endmembers have been found (Dreher and others, 2005; Bacon and others, 2014). Upon entry to the Bering Sea, this ignimbrite produced a tsunami recorded by discontinuous pumiceous sand layers within Holocene peat along the northern Bristol Bay coastline of Alaska up to 15 m above mean high tide (Waythomas and Neal, 1998). Larsen (2006) constrained the pre-eruptive magma storage conditions for the Aniakchak II rhyodacite and andesite magmas based on cold-seal hydrothermal phase equilibria experiments and petrologic data. These findings showed pre-eruptive storage conditions for the rhyodacite at ~885°C and 65–150 MPa (3–6 km depth) compared to ~1000°C and >110 MPa (>4 km depth) for the andesite.

A deep, early caldera lake formed in the collapse basin after the Aniakchak II eruption accompanied by the subaqueous effusion of four lava domes. This lake, with an estimated volume of 3.7 x 10^9 m^3 and a depth of at least 100 m at its highest stand, catastrophically drained ca. 1,860 yr B.P. through a steeply incised notch in the eastern caldera wall known as The Gates (fig. 2; McGimsey and others, 1994; Waythomas and others, 1996; VanderHoek and Myron, 2004). Building-sized boulders were carried several km east from Aniakchak volcano by the torrent of muddy flood waters, which eventually inundated the region with sediment-laden currents and buried a prehistoric village site located ~40 km east along Aniakchak Bay on the Pacific coast (VanderHoek and Myron,

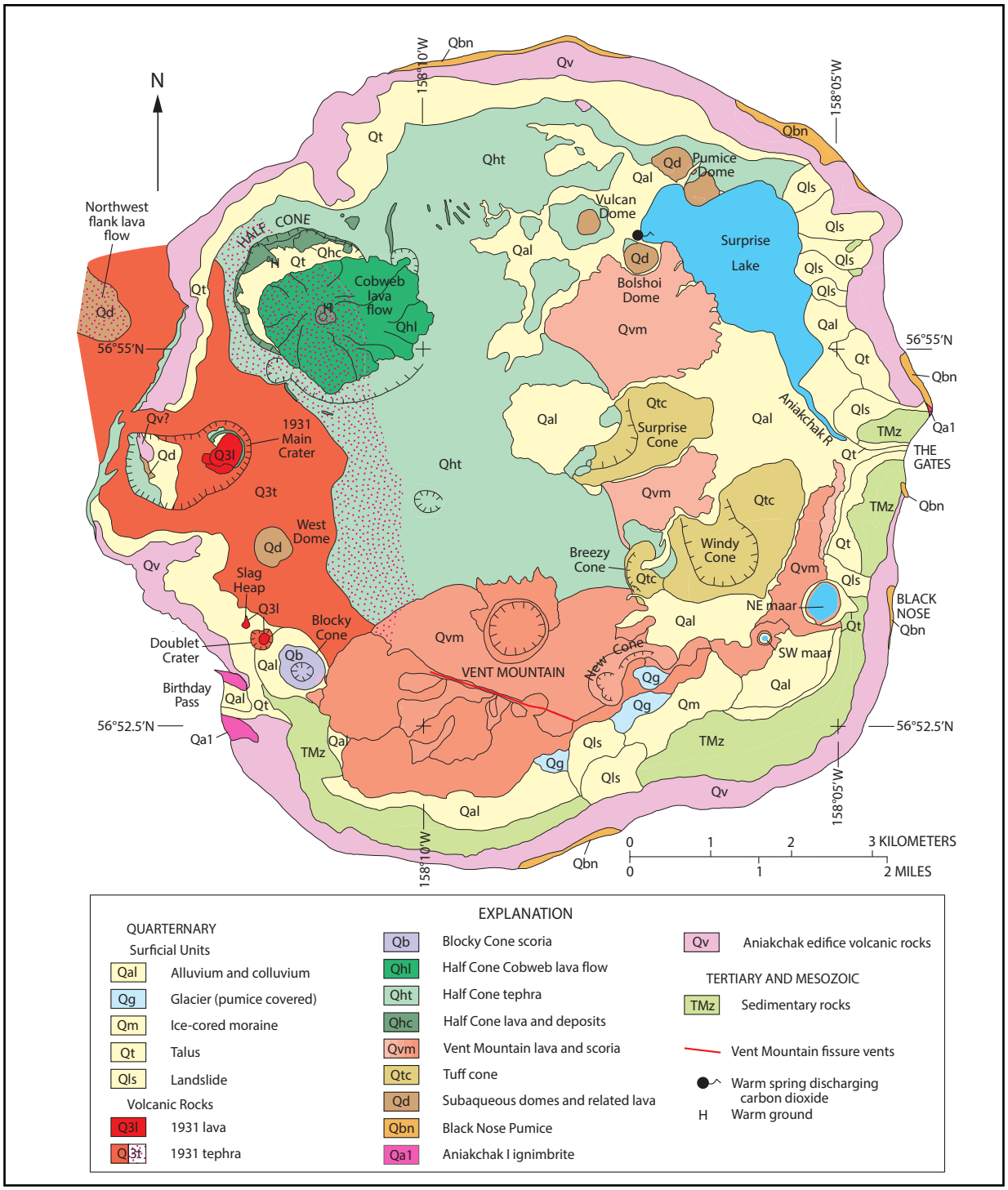

Figure 2. Simplified geologic map of Aniakchak caldera (modified after fig. 10 of Bacon and others, 2014, and fig. 5 of Neal and others, 2001; and unpublished geologic mapping by C.A. Neal, R.G. McGimsey, and T.P. Miller). Half Cone lies along the northwest floor of Aniakchak caldera. Pre-400 yr B.P. lavas and tephra deposits exposed in the severed flanks of Half Cone are mapped together with agglutinate and welded spatter deposits of the ~400 yr B.P. eruption (unit Qhc). These units are distinguished from thick nonwelded pyroclastic density current deposits from the ~400 yr B.P. eruption (unit Qht) and the Cobweb lava flow (unit Qhl). The Cobweb tuff cone lies near the middle of the Cobweb lava flow, where warm ground was observed by Neal and others (2001) (noted by H). Tephra from the 1931 eruption (unit Q3t) is mapped as a solid color where thick and by a stipple pattern where thinner or mantling lavas from Vent Mountain, the Cobweb lava flow, thick pyroclastic density current deposits from the ~400 yr B.P. eruption, and the northwest flank of Half Cone.

2004). At present, Surprise Lake (~3 km^2), located along the northern caldera wall, is what remains of the formerly much larger intracaldera lake. It continues to drain though The Gates into the Aniakchak River, a National Wild and Scenic River that flows east to the Pacific Ocean within the same drainage as the ca. 1,860 yr B.P. flood (McGimsey and others, 1994; Waythomas and others, 1996).

Volcanic activity following the violent lake-draining event includes the production of larger intracaldera composite vents like Vent Mountain and Half Cone (Qvm and Qhc in fig. 2, respectively) as well as the emplacement of smaller tuff cones and a small scoria cone (Neal and others, 2001). Vent Mountain is a scoria and spatter cone that stands about 500 m above the caldera floor, making it the most prominent topographic and volcanic feature within the caldera. Lavas erupted from Vent Mountain and an associated northeast-trending fissure on its southern flanks are silicic andesite to dacite, which account for ~1.5 km^3 DRE of erupted material (Bacon and others, 2014). Vent Mountain lavas extend up to 6 km north to Surprise Lake and 6 km northeast to The Gates. Vent Mountain lavas emplaced to the north and northwest are buried beneath the youngest pyroclastic deposits from Half Cone (Qht in fig. 2) and deposits from the 1931 eruption. A small debris-covered glacier was identified by Neal and others (2001) in the perennially shadowed, north-facing slopes between Vent Mountain and the southwest caldera wall.

Half Cone is an arcuate structure that represents the remains of a collapsed composite cone that formed against the western Aniakchak caldera wall. The steep walls of Half Cone expose thick, older but post-caldera pyroclastic deposits, eviscerated lava domes, and vitrophyric andesite to dacite lavas with spectacular columnar joints. Bacon and others (2014) reported radiocarbon ages of 840±30 ^{14}C yr B.P. (690–800 calibrated 2σ age range calendar yr B.P.) for the oldest pyroclastic deposit exposed within the Half Cone walls. The most recent pyroclastic deposits that cap the Half Cone walls were emplaced 380±50 ^{14}C yr B.P. (310–510 calibrated 2σ age range calendar yr B.P.; Bacon and others, 2014) during Half Cone's cataclysmic eruption. The focus of this study is this cataclysmic eruption from Half Cone, which we refer to as the "~400 yr B.P." eruption. The Cobweb lava flow (Qhl in fig. 2)—a ~50-m-thick crystal-rich blocky dacite lava that spread radially in nested lobes from a vent at the foot of Half Cone's steep crescentic walls—and a small tuff cone perched atop the vent region of the Cobweb lava flow were emplaced within a basin that formed following the ~400 yr B.P. collapse of Half Cone (fig. 3).

Eruptions from vents on the western floor of the Aniakchak II caldera during May and June of 1931 represent the most recent volcanic activity at Aniakchak volcano (Hubbard 1932a). Work by Neal and others (2001) and Nicholson and others (2011) indicated that ash from the 1931 eruption was dispersed as far as 600 km to the north over 6 weeks of activity, resulting in a total bulk volume of 0.9 km^3 and approximately 0.3 km^3 of dacite and andesite magma. The walls of the main 1931 eruption crater expose 40 m of pyroclastic deposits in which nine rhythmically bedded packages of alternating dacite pyroclastic fall and lithic-rich flow layers overlie agglutinate from the ~400 yr B.P. eruption (Neal and others, 2001; Nicholson and others, 2011). The top of the 1931 crater walls reveal another 40 m of alternating andesite spatter agglutinate and lithic-rich fall layers, suggesting a transition to Strombolian eruption style (Nicholson and others, 2011). Pyroclastic deposits from the 1931 eruption mantle the western flanks of Half Cone and the surface of the Cobweb lava flow. 1931 deposits also partially fill the Cobweb tuff cone crater. Two subsidiary vents about 2 km south of the 1931 main crater produced small dacite and rhyodacite lava flows (fig. 2).

Nearly a century after its last eruption, Aniakchak volcano continues to show episodic signs of a restless subvolcanic system including deep long-period (LP) earthquake activity (Power and others, 2004) and magmatic CO_2 and helium

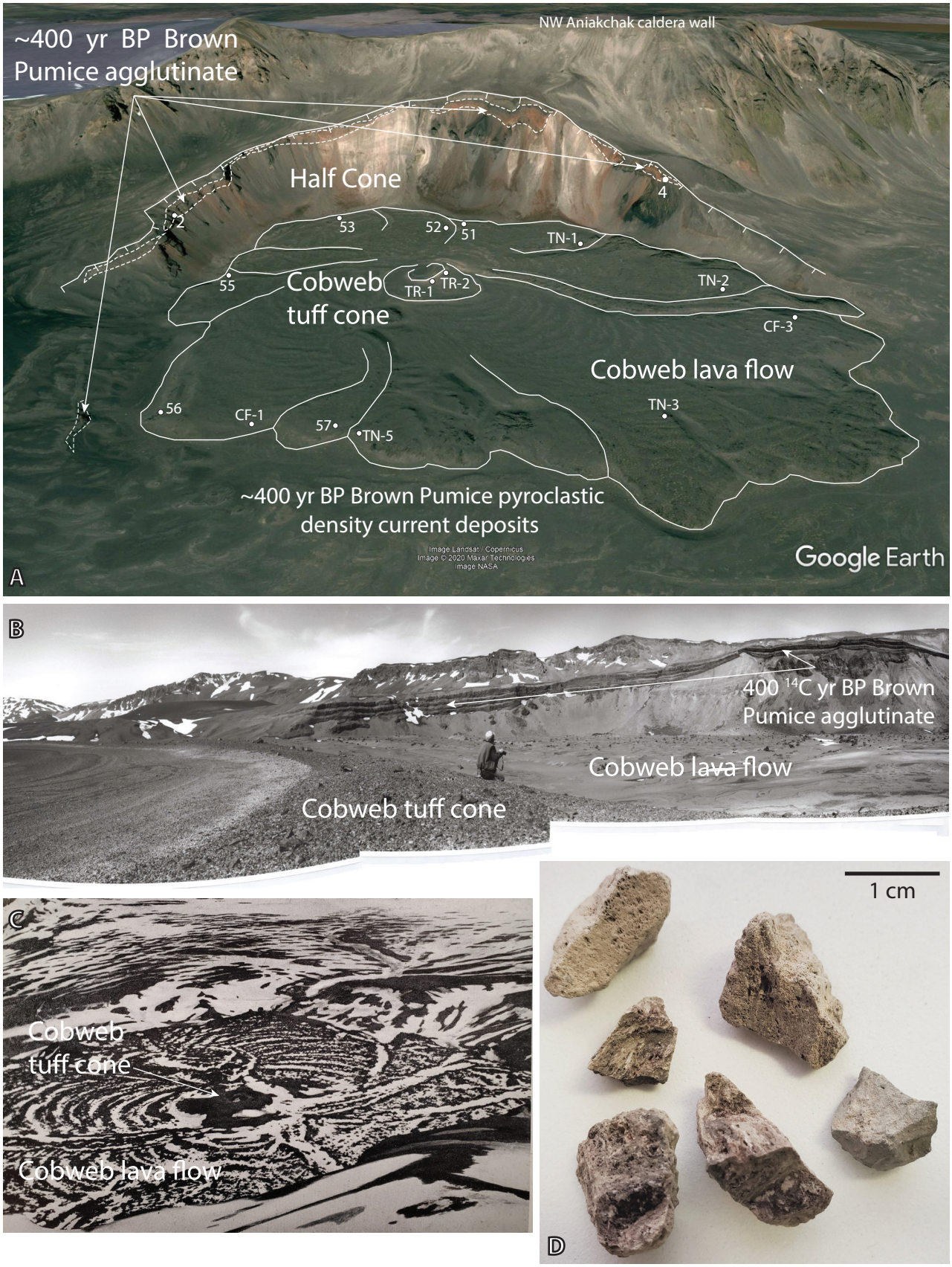

Figure 3. See full caption on next page.

bubbling through surface spring water (Evans and others, 2015) suggesting that explosive eruptions will occur in the future.

METHODS

The goal of this study is to use field and analytical observations of deposits from the ~400 yr B.P. Half Cone eruption to reconstruct the eruption chronology, estimate the volume and dispersal characteristics of tephra, and gain insight into pre-eruptive magma storage conditions. As such, we focus on the ~400 yr B.P. pyroclastic deposits, the Cobweb lava flow, and Cobweb tuff cone. Geological investigations were conducted in the field during the summers of 1992–1994, 1997, and 2002. Field sites were located within Aniakchak caldera and beyond the caldera rim, mostly to the north and northeast of the volcano. Pyroclastic samples considered in this study (app. A) are described in terms of the color of pyroclasts, percentage of accidental lithics, presence or absence of compositionally banded pyroclasts, thickness, relative changes in grain size, pyroclast vesicularity, sorting, bedforms, and the degree of induration and welding. At several locations, the dimensions of the three largest lithics from mappable tephra horizons were measured. Deposit thicknesses and lithic measurements are documented in appendix B. We were unable to acquire quantitative grain-size data (e.g., median grain size, sorting) for tephra deposits because many fragile pyroclasts, particularly pyroclasts larger than 10 cm, had cracked apart or broken upon impact, making them unsuitable for sieving and granulometric analyses. We interpret clast-supported and pumice-rich tephra units that conformably overlie the underlying topography and sediments as fall deposits. Ash-rich beds with pyroclasts and lithics set in a fine-ash matrix that erode underlying deposits are interpreted as pyroclastic density current deposits.

Major and trace element compositions were determined for a subset of pyroclasts and lava flow samples from the ~400 yr B.P. deposits collected in 1992 and 1993 by C. Neal and R. McGimsey, in 1997 by C. Bacon, and in 2002 by B. Browne and C. Neal (Browne and others, 2004; Browne, 2006; Bacon and others, 2014). Samples were analyzed by the Peter Hooper GeoAnalytical Lab at Washington State University (WSU) by wavelength-dispersive X-ray fluorescence (XRF) and inductively coupled plasma mass spectrometry (ICP-MS; app. C). WSU uses the methods described in Johnson and others (1999) and Knaack and others (WSU, written commun., 1994) for XRF and ICP-MS analyses respectively. Nye and others (2017, 2018) summarize the analytical protocols applied to these samples and give an overview of the analytical precision, accuracy, and significant digits applicable to this dataset. Comparison with prior analyses published by Bacon and others (2014) is possible because all AVO geochemical analyses were re-calibrated in 2007 to be time-consistent and internally consistent with data collected post-2007 (Nye and others, 2018). Stereoscopic examination helped to identify and describe banded pyroclasts, which had been excluded from sample submissions for whole-rock compositional analyses.

Polished thin sections were prepared of pyroclasts and lavas sampled in 2002 by B. Browne for

Figure 3, page 8 (previous). Images of Cobweb lava flow and Cobweb tuff cone. **A.** Oblique Google Earth image looking northwest toward Half Cone showing pre-400 yr B.P. lavas and tephra exposed in the exposed walls as well as the distinctively orange agglutinate and welded spatter deposits from the ~400 yr B.P. cataclysmic eruption. Also labeled are the Cobweb lava flow lobes, an outline of the Cobweb tuff cone, thick pyroclastic density current deposits emplaced during the Brown Pumice phase of the ~400 yr B.P. eruption, and the names and locations of samples collected by B. Browne and C. Neal in 2002 that are used in this study. **B.** Panorama photograph looking east toward Half Cone, the Cobweb lava flow, and the Cobweb tuff cone taken from the northern crater rim of the Cobweb tuff cone (photograph by C. Neal). **C.** Aerial photograph from Hubbard (1931) of the Cobweb lava flow and Cobweb tuff cone showing flow lobes, flow levees, and blocky surface prior to the 1931 eruption, which blanketed the lava and tuff cone with thick deposits of ash, pyroclasts, and lithics. **D.** Photograph showing typical pyroclasts from the Cobweb tuff cone, some of which are gray and others show stripes and swirls of gray and tan compositional banding.

petrographic examination. *In situ* major element analyses of matrix glass and plagioclase, pyroxene, and some Fe–Ti oxides were conducted via electron probe microanalysis at the Advanced Instrumentation Laboratory at the University of Alaska Fairbanks and the University of California Los Angeles (UCLA) Department of Earth, Planetary, and Space Sciences. Most *in situ* major element analyses of Fe–Ti oxide were performed in Menlo Park with a JEOL 8900 electron microprobe. Mineral analyses of plagioclase and pyroxene were obtained after standard calibration using a 15-kV accelerating voltage, a 10-nA beam current, and a focused 1-µm beam. Mineral analyses of Fe–Ti oxides were obtained after standard calibration using a 30-kV accelerating voltage, a 10-nA beam current, and a focused 1-µm beam. Smithsonian calibration standards used in plagioclase analyses include Tiburon albite (Si, Al, Na), ilmenite (Ti), olivine (Mg, Fe), anorthite (Ca), and orthoclase10 (K). Smithsonian calibration standards used in pyroxene analyses include hypersthene (Si, Mg, Fe), ilmenite (Ti), augite (Ca), hornblende-2 (Al), chromite (Cr), spessartine (Mn), Tiburon albite (Na), and orthoclase10 (K). Smithsonian calibration standards used in magnetite and ilmenite analyses include magnetite (Fe, Mg), ilmenite (Ti, Mn), quartz (Si), chromite5 (Al, Cr, Ni), and vanadium (V). Glass analyses were obtained after standard calibration using a 15-kV accelerating voltage, 10-nA beam current, and a defocused 5-µm diameter beam while monitoring for volatile loss during 10-second count times (e.g., Na and K migration). Natural glass Smithsonian calibration standards were used in glass analyses, including CCNM obsidian (Si, Al, Na, K), BasaltGlass-2 (Mg, Fe, Ca), BasaltGlass-3 (Ti, P, Mn), and Scapolite (Cl). Glass standards were also used as unknowns throughout the analyses to monitor analytical drift.

STRATIGRAPHY OF THE ~400 YR B.P. ERUPTION

The ~400 yr B.P. eruption chronology is recorded most completely in thick pyroclastic fall deposits with interbedded pyroclastic density current deposits exposed in the walls of Half Cone, on the caldera floor and caldera rim, and atop other topographic highs such as Vent Mountain and Surprise Cone. Those deposits recorded an extended period of voluminous, highly energetic explosive volcanic activity from Half Cone. This explosive phase was followed by the effusion of the Cobweb lava flow and finally production of a small tuff cone located in the center of the Cobweb lava flow. Both the Cobweb lava flow and Cobweb tuff cone are mantled by deposits from the 1931 eruption (Hubbard, 1932b; Neal and others, 2001; Nicholson and others, 2011). Below, we first describe new age constraints of the eruption followed by the stratigraphy and dispersal of the fall and flow deposits that account for the majority of magma erupted in this event. Finally, we describe the Cobweb lava flow and Cobweb tuff cone.

Radiocarbon dating (standard and American Mass Spectrometry [AMS]) of organic material to constrain the eruption age of the Pink Pumice and Brown Pumice has been carried out by multiple geologists using four different laboratories over a span of nearly two decades (1985–2002; table 1). The most recent radiocarbon analyses presented here are from wood collected within soil below the distinctive Pink Pumice fall deposit. One standard and one AMS date of these wood fragments returned median probability calibrated ages of 400 and 424 yr B.P., respectively. In the mid 1980s, three dates that were older by more than a century were obtained from both wood and soil below the Pink Pumice. Unfortunately, the data sheets for these older ages are missing and we are unable to evaluate and report complete metadata for the samples. While all other results are consistent with a ~400 yr B.P. age of the cataclysmic Half Cone eruption as proposed by Bacon and others (2014), we encourage subsequent studies to further refine the age of this eruption through dating of both proximal and distal tephra falls.

Proximal exposures of the explosive phase of the eruption reveal the following general stratigraphy: thick, low-density, light-colored Plinian pumice fall abruptly overlain by darker Plinian pumice fall interbedded with pyroclastic density current deposits.

Table 1. Radiocarbon dates constraining post-caldera tephra fall deposits from Aniakchak volcano. Units dated are preliminary based on field correlations and, where possible, bulk chemistry of juvenile clasts. Locations in decimal degrees, WGS84 datum. Dates calibrated using CALIB (Stuiver and Reimer, 1993) version 8.2; B.P. (before present) ages are reported with respect to 1950 C.E.

Field Sample ID	Latitude N	Longitude W	Collector	Stratigraphic context or unit dated	Analytical age (2σ) ^{14}C yr BP)	Calibrated age range (2σ) cal yr BP	Calibrated age range (2σ) cal AD)	Relative area under distribution	Median probability calibrated age	Radiocarbon Lab Sample ID	Radiocarbon Lab/type of analysis	Material Dated	δ^{13}C
NA02-6C	57.067	-158.09	Neal, C	Half Cone Pink Pumice	360 ± 80	280-539	1411–1670	0.98	400	GX-29531	G (STD)	wood	-26.7
NA94-24A	56.9348	-158.1104	Neal, C	Half Cone Pink Pumice	390 ± 60	289-545	1405–1661	1.00	424	B-76809	B (AMS)	wood	-28.8
85AMm28	nr	nr	Miller, TP	Half Cone Pink Pumice	500 ± 80	427-633	1297–1523	0.92	528	I-14, 222	T	wood	nr
85AMm14	57.0583	-158.0833	Miller, TP	Half Cone Pink Pumice	590 ± 90	475-689	1261–1475	1.00	592	2358	U	soil	nr
85AMm20	57.05	-158.125	Miller, TP	Half Cone Pink Pumice	590 ± 160	291-802	1148–1659	0.98	580	2358	U	soil	nr

B, Beta Analytic
U, U.S. Geological Survey Laboratory Reston, VA (M. Rubin) and Menlo Park (S. Robinson)
G, Geochron Laboratory
T, Teledyne
STD, Standard 14C processing
AMS, Accelerator mass spectrometry
nr, not reported

Pyroclasts in the lower pumice fall are typically white-beige to a deep reddish pink (fig. 4) depending on the degree of vesicularity and syn-eruptive oxidation, both of which correlate positively with pyroclast diameter. Pyroclasts in non-welded exposures of the upper pumice fall are typically brown, dark gray, or black unless oxidized to orange, crimson, or yellow. As such, previous studies have referred to the basal ~400 yr B.P. fall deposit as the "Pink Pumice" or the "Pink Pumice phase" due to abundant pink-colored and highly vesicular pyroclasts, and the upper fall deposit as the "Brown Pumice" or the "Brown Pumice phase" due to it being composed mostly of brown to dark gray scoriaceous pyroclasts (figs. 4, 5; Neal and others, 2001; Browne and others, 2004; Browne, 2006; Bacon and others, 2014). Banded pumice shows mixing between "Pink" and "Brown" magmas, particularly near the transition from the Pink Pumice to the Brown Pumice in the pyroclastic stratigraphy as well as in deposits produced at the end of the eruption from the Cobweb tuff cone. This indicates that at least two magma compositions were molten and in contact at the time of eruption. Tephra stratigraphy descriptions are divided into (1) proximal locations on the steep cliffs of Half Cone, (2) locations within the caldera, and (3) locations outside of the caldera.

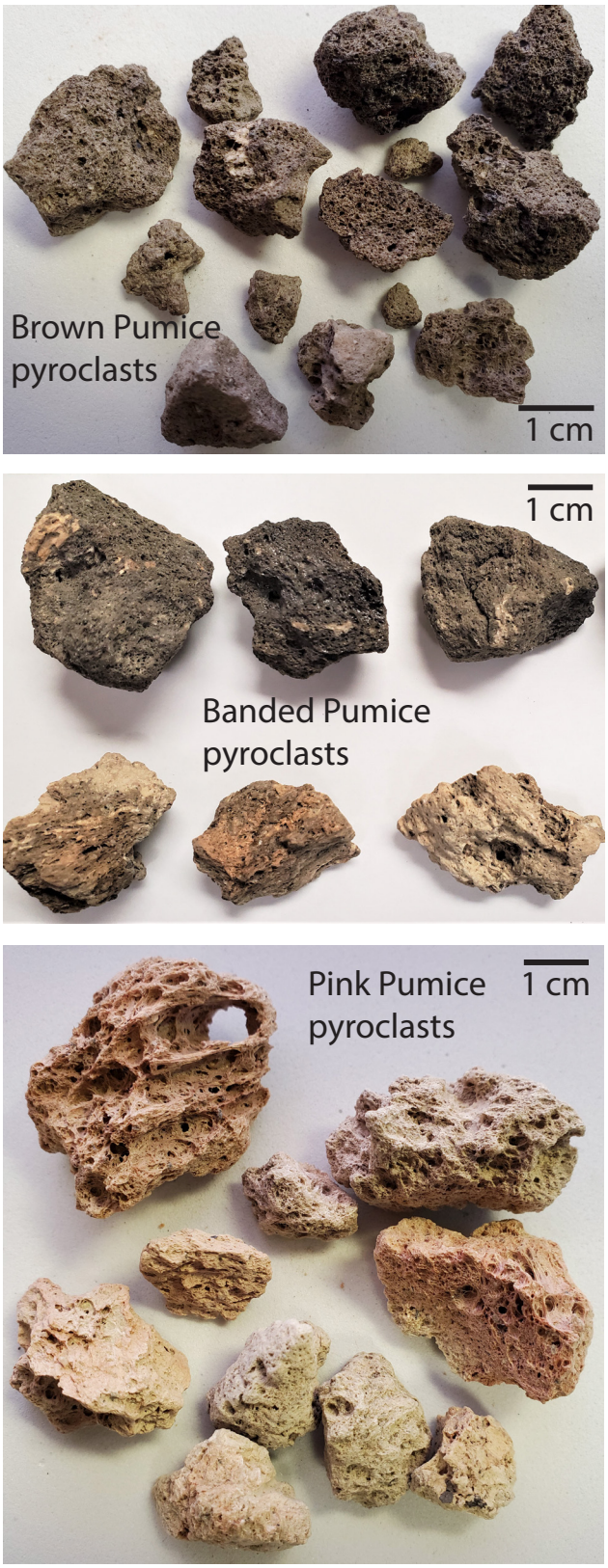

Figure 4. Photographs of typical pyroclasts from the Pink Pumice phase (bottom) and from the Brown Pumice phase (top) of the ~400 yr B.P. eruption. Pink Pumice pyroclasts are typically white-beige to pink depending on the degree of vesicularity and syn-eruptive oxidation. Pink Pumice pyroclasts also show a larger range of, and higher overall, vesicularity. Brown Pumice pyroclasts are typically brown, dark gray, or black unless oxidized or compositionally banded. Banded pyroclasts (middle) show mixing between "Pink" and "Brown" magmas.

Proximal Tephra Stratigraphy

Proximal stratigraphy of the ~400 yr B.P. deposit is best exposed along cliffs on the upper western wall of the eviscerated Half Cone edifice (fig. 6). Measured sections at locations 2 and 4 on the southwest and northeast cliffs of Half Cone

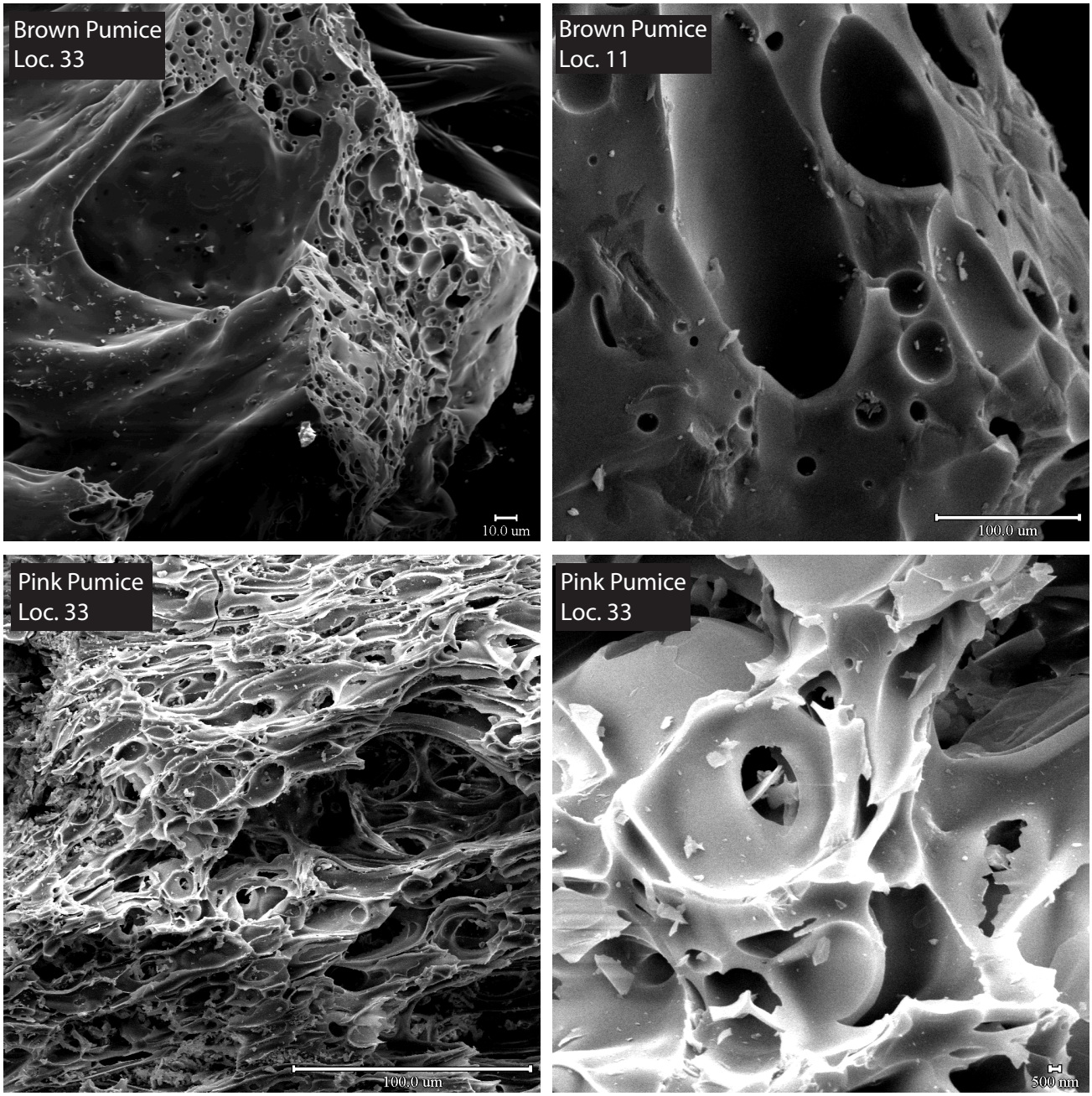

Figure 5. Scanning electron microscope images of Pink Pumice (bottom) and Brown Pumice (top) pyroclasts. Location numbers for samples are included for reference (fig. 7). Note the highly vesicular Pink Pumice pyroclasts with thin and delicate bubble walls. Brown Pumice pyroclasts possess a range of vesicularity.

reveal a Pink Pumice thickness of 270 and 350 cm, respectively (fig. 7). At these locations, the Pink Pumice is a nonwelded, coarse-grained, clast-supported fall deposit that overlies a dark soil and thin, fine-grained, green-gray ash bed. The base of the Pink Pumice contains white to tan ash fragments, 1–3-mm pumice, and black, glassy, accidental lithics up to 1 mm in diameter that account for 50 percent of the deposit volume. Above the fine-grained base, the Pink Pumice reversely grades to a prominent coarser horizon marked by oxidized Pink Pumice pyroclasts and sparse (<5 percent) black, gray, and white accidental lithics. White "felsite" lithics (77 wt% SiO_2) composed mostly

of quartz and feldspar are particularly conspicuous in the Pink Pumice (Bacon and others, 2014). Pyroclasts in this coarse horizon range up to 35 cm in diameter and contain widespread impact fractures, which cause larger pyroclasts to crumble apart when removed from outcrops. Accidental lithics in coarse horizons range up to 12 cm in diameter. Two coarse horizons with notably larger pyroclasts are observed at location 4: one in the lower and another in the upper third of the Pink Pumice (fig. 7). The upper 30–50 cm of proximal Pink Pumice fall deposits is graded normally. Brown-colored and banded pyroclasts marked by stripes and swirls of pink-colored and brown-colored pumice account for 5–10 percent of the deposit within 30 cm of the Pink–Brown Pumice transition. In some proximal locations, the upper Pink Pumice fall deposit contains dense ballistic blocks that range up to 150 cm in diameter (figs. 6, 7).

The lower 55 cm and 20 cm of the Brown Pumice at locations 2 and 4, respectively, is a nonwelded, coarse-grained, clast-supported scoria fall deposit (fig. 7). The base of the Brown Pumice contains ~50 percent accidental lithics and abundant dark brown and brown-yellow scoria. Above the base, the concentration of accidental lithics falls to 15–30 percent but is still significantly higher overall than in the Pink Pumice. Pyroclast diameters increase from 3–5 cm at the base to 18–24 cm at the top, the coarsest of which are deeply oxidized to brick red. The top of the lower Brown Pumice fall in the Half Cone cliffs undulates with scour structures

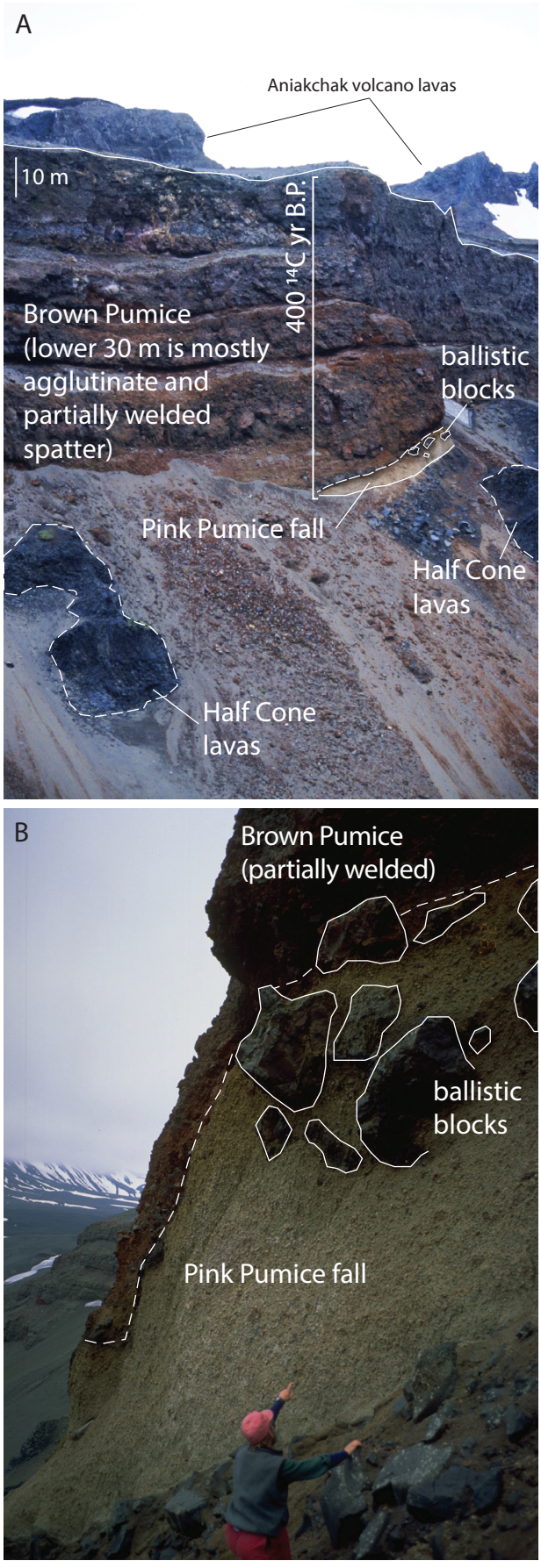

Figure 6. Photographs of upper Half Cone walls. **A.** Low-altitude, oblique aerial photograph showing light tan Pink Pumice fall deposits overlying pre-400 yr B.P. Half Cone lavas and tephra. The uppermost Pink Pumice deposits contain large and dense lithic blocks near the transition to overlying deposits emplaced during the Brown Pumice phase. The bulk of Brown Pumice deposits in the Half Cone cliffs are composed of a lower ~30–35 m of oxidized agglutinate and welded spatter with thinner beds of nonwelded and lithic-rich fall deposits overlain by ~25–30 m of coarse lithics with lesser amounts of agglutinate and brown scoria. **B.** Photograph of the clast-supported Pink Pumice fall deposit with large dense lithics overlain by scoria fall and partially welded spatter and agglutinate of the lower Brown Pumice at location 2. Geologist is 1.7 m tall.

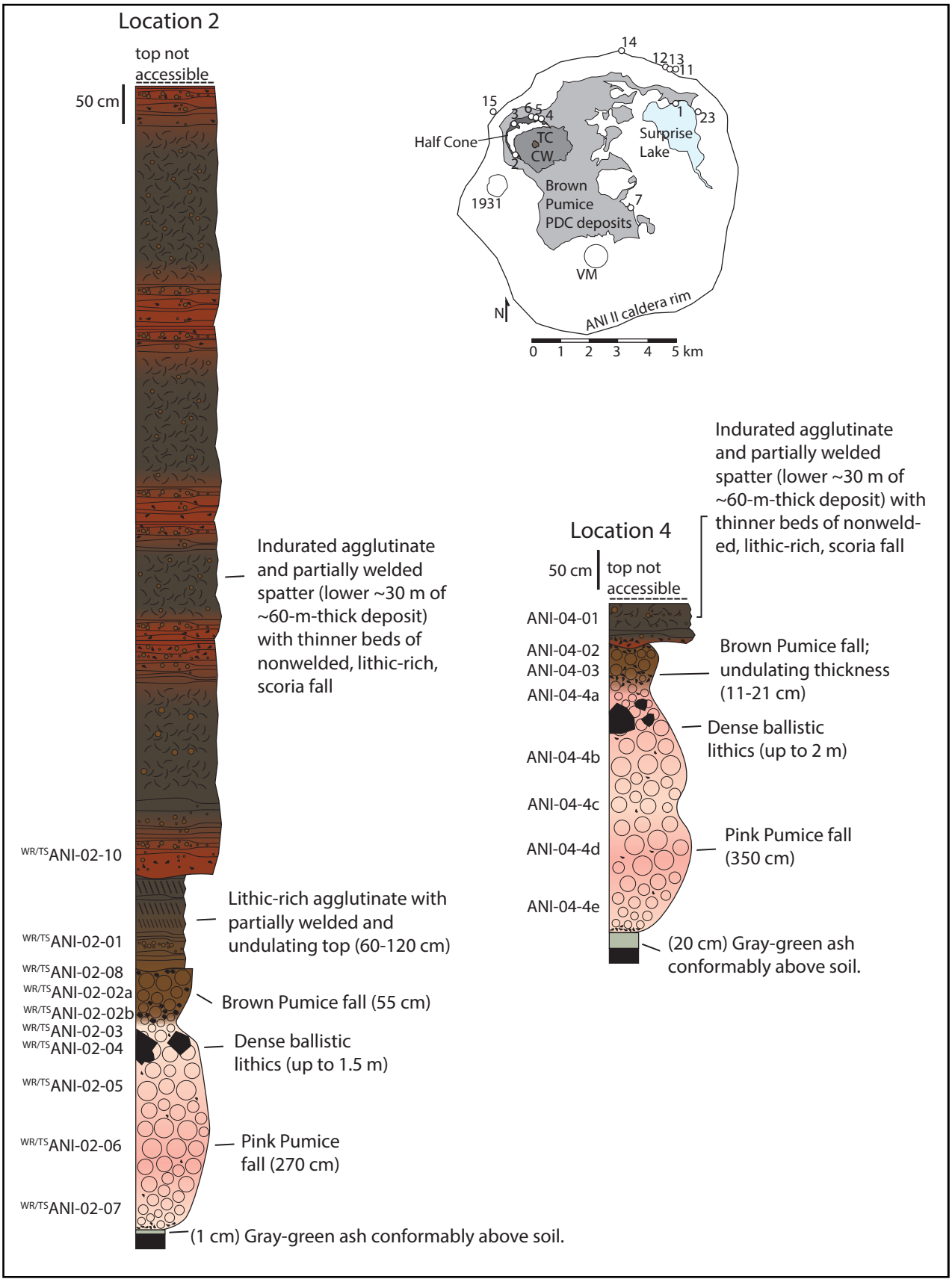

Figure 7. See full caption on next page.

filled by a dark, indurated, lithic-rich pyroclastic deposit with cm-scale laminations. This upper region of the lower Brown Pumice fall ranges in thickness from 60 to 120 cm and becomes progressively darker and more glass rich with pronounced flow banding in the upper half.

An additional ~60 m of the Brown Pumice deposit is exposed above the clast-supported scoria fall deposit in the cliffs of Half Cone (fig. 6). The lower half of these deposits is composed of <1–3-m-thick nonwelded, lithic-rich pyroclastic fall deposits with pink, tan, and brown pyroclasts sandwiched by thicker (5–10 m) ledge-forming ramparts of agglutinate and welded spatter. The base and top of agglutinate and spatter ramparts are deeply oxidized from orange to red while their interiors are black and vitrophyric with fluidal-shaped Brown Pumice pyroclasts (fig. 7). The thickness of the partially welded agglutinate deposits is relatively constant along the 4 km Half Cone rim but the deposit decreases in thickness away from Half Cone and has not been found more than ~2 km from the rim. Brown Pumice agglutinate is exposed within the lower northeast walls of the 1931 crater as well as the northern flanks of Vent Mountain and West Dome (fig. 2; Neal and others, 2001; Nicholson and others, 2011; Bacon and others, 2014). These deposits are shown in figures 13D and E of Bacon and others (2014). Brown Pumice agglutinate also occurs atop ridges of ash-rich, cross-bedded pyroclastic density current deposits emplaced during the Brown Pumice phase in the central caldera (fig. 8H; Neal and others, 2001).

The upper half of Brown Pumice deposits exposed in the Half Cone rim occur atop sheer cliffs and are difficult to access. Our descriptions are limited to ground-based observations aided by binoculars and photos acquired via helicopter. Unlike the lower half of the cliff-forming deposits, which is largely agglutinate and partially welded spatter, the uppermost ~30 m primarily consists of two ~15-m-thick packages of dense, angular, coarse lithics that range up to 3 m in diameter. Thin lenses of red scoria and oxidized fluidal agglutinate also occur within coarse lithic deposits. An approximately 2-m-thick bed of gray, nonwelded, fine-grained lithics and gray and brown scoria separate the two thicker packages of coarse lithics (fig. 6). We encourage future studies of these deposits, as they may reveal how the pre-400 yr B.P. Half Cone edifice was destroyed during the ~400 yr B.P. cataclysmic eruption.

Tephra Stratigraphy Within Aniakchak Caldera

Well preserved, accessible exposures of the ~400 yr B.P. tephra stratigraphy within Aniakchak caldera are found near Pumice Dome in the northeast region of the caldera and atop topographic highs, such as the northern flank of Vent Mountain and northwestern flank of Surprise Cone (figs. 8, 9).

Similar to outcrops on the Half Cone cliffs, the Pink Pumice within the caldera is a nonwelded, coarse-grained, clast-supported fall deposit composed of highly vesicular pyroclasts and sparse black, gray, and white "felsite" accidental lithics. In most locations where the base is exposed, the Pink Pumice overlies a thin, green-gray ash bed that in turn overlies >2 m of dark, fine-grained pyroclastic deposits from Surprise and Windy Cones (fig. 8B, C; Neal and others, 2001). The Pink Pumice at location 1 near Pumice Dome is 36 cm thick (fig. 9). It displays reverse grading from an ash and

Figure 7, page 15 (previous). Annotated and measured stratigraphic columns with scale bars of accessible ~400 yr B.P. tephra descriptions are limited at locations 2 and 4 along the Half Cone walls. Stratigraphic columns are drawn with a schematic weathered profile instead of a grain-size scale because fractured and broken pyroclasts in the Pink Pumice and Brown Pumice prevented granulometric measurements. The uppermost Brown Pumice deposits were not measured due to their precipitous location atop sheer cliffs. Sample numbers are included adjacent to stratigraphic columns where tephra was collected. Sample numbers indicate those with corresponding whole-rock geochemical data (WR) and petrographic thin section (TS). Inset map shows locations 2 and 4 with respect to the Aniakchak caldera rim, Half Cone, Cobweb lava flow (CW), Cobweb tuff cone (TC), thick and unconsolidated pyroclastic density currents emplaced during Brown Pumice phase, Surprise Lake, and vents of the 1931 eruption and Vent Mountain (VM).

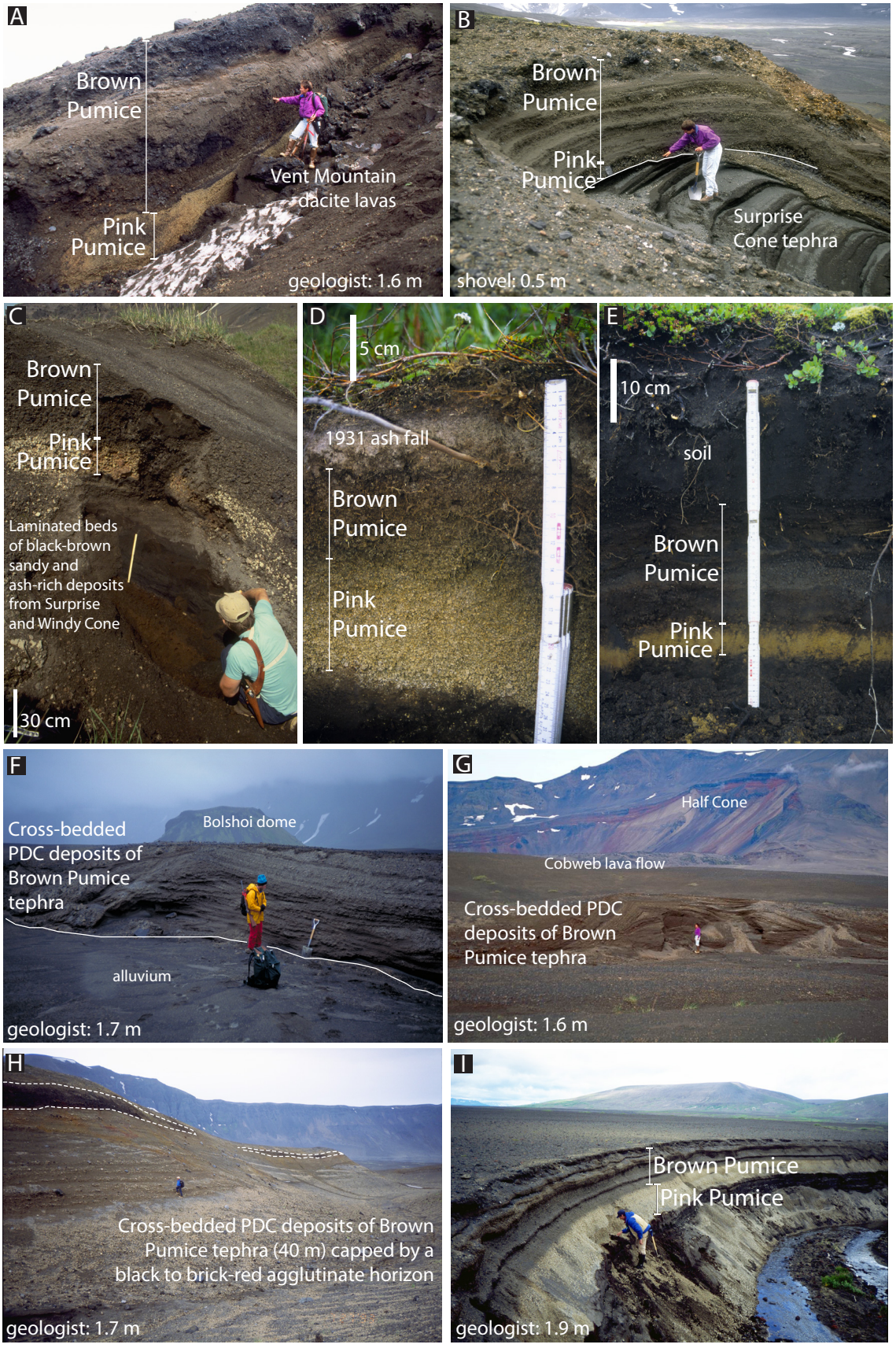

Figure 8. See full caption on next page.

lithic-rich base to a coarser-grained horizon with up to 15-cm-diameter pyroclasts. The coarsest and most vesicular pyroclasts in the middle of the Pink Pumice also contain the most widespread impact fractures and display the deepest gray-pink color due to oxidation. The upper Pink Pumice fall deposit contains ~10 percent brown-colored and banded pyroclasts and grades normally to the 5–10 cm transition from pink-dominated to brown-dominated pyroclasts at location 1.

Overlying the Pink Pumice at location 1 is a ~230 cm interbedded fall and density-current deposit emplaced during the Brown Pumice phase of the eruption (fig. 9). The Brown Pumice fall grades reversely from a lithic-rich base with sparse pink-colored and banded pyroclasts to a coarse-grained and lithic-rich middle containing fist-sized brown scoria with red oxidized cores. A 1-m-thick poorly sorted, ash-rich, matrix-supported pyroclastic density current deposit is interbedded with the Brown Pumice fall deposits at location 1. This ash-rich unit displays mm- to cm-scale laminations defined by differences in grain sizes and abundance of accidental lithics as well as up to 2 m long, discontinuous, lenses composed of rounded pink- and brown-colored pyroclasts. Brown pyroclasts are coated with ash immediately above and below this thin ash bed. Another 75 cm of Brown Pumice scoria fall overlain by scoriaceous soil occurs at the top of the section at location 1.

Location 7 (fig. 9) is situated atop the rim of Surprise Cone, ~3.5 km south of location 1 and 4 km southeast of Half Cone. Here, the 16-cm-thick Pink Pumice overlies Surprise Cone pyroclastic deposits along an angular unconformity (fig. 8B). The ~1,000 yr B.P. Surprise Cone deposits (Bacon and others, 2014) are dark gray, poorly sorted, and matrix supported with bedding defined by changes in grain size and the ratio between accidental lithics and subrounded vesicle-poor pyroclasts (fig. 9). The Pink Pumice at this location grades reversely from an ash- and-lithic-rich base with 1 cm pyroclasts and 30 percent accidental lithics to pinkish-beige pyroclasts up to 4 cm in diameter that are coated in fine ash. The upper 4 cm grades normally to a finer lithic-rich horizon at the Pink Pumice–Brown Pumice transition. Pink-colored banded pyroclasts account for 20 percent of the lower 8 cm of the Brown Pumice fall, which grades reversely from 1–2 cm scoria at the base to 16-cm-diameter scoria and breadcrusted bombs at the top. The upper 76 cm of the Brown Pumice deposit consists of ash-rich, matrix-supported, poorly sorted pyroclastic density current deposits with mm- to cm-scale laminations, rounded pyroclasts, and ballistic sags. These ash-rich pyroclastic deposits occur as packages of darker, ash- and lithic-rich deposits with sparse pumice alternating with lighter colored, coarser grained, pumice-rich deposits. The ~400 yr B.P. deposit is capped by the

Figure 8, page 17 (previous). Field photos showing characteristics of Pink Pumice and Brown Pumice deposits located within and outside Aniakchak caldera. **A.** Tan and clast-supported Pink Pumice fall overlain by scoria fall and interbedded pyroclastic density current deposits of the Brown Pumice phase on the northern Vent Mountain flanks, ~3.5 km south from vent. **B.** Tan clast-supported Pink Pumice fall deposit (indicated by geologist's hand) and overlying scoria fall with interbedded ash-rich pyroclastic density current deposits 4.2 km southeast from vent at Location 7 (fig. 9) emplaced during the Brown Pumice phase. The ~400 yr B.P. deposits overlie dipping phreatomagmatic deposits of Surprise Cone. **C.** Clast-supported Pink Pumice fall with oxidized pyroclasts underlie Brown Pumice scoria fall 5.1 km northeast of vent at Location 1 (fig. 9). Phreatomagmatic deposits from Surprise and Windy Cone under lie the ~400 yr B.P. deposits at this location. **D.** Clast-supported Pink Pumice and Brown Pumice fall deposits above dark brown soil with 1931 ash fall below modern soil 35 km northeast of vent at location 37. **E.** Fine lapilli in clast-supported Pink Pumice and Brown Pumice fall deposits above dark soil 10 km southeast of vent at location 27. **F.** Looking north toward Bolshoi Dome at cross-bedded pyroclastic density current deposits emplaced during the Brown Pumice phase of the eruption on the central caldera floor ~2.5 km southeast from vent. **G.** View to the west toward Half Cone showing cross-bedded pyroclastic density current deposits emplaced during the Brown Pumice phase of the eruption on the caldera floor ~2 km east from vent (fig. 13 from Neal and others, 2001). **H.** View toward the north of ~40-m-thick pyroclastic density current deposits emplaced during the Brown Pumice phase of the eruption capped by dark brown to black agglutinate that is locally oxidized to red. Note oxidation of underlying pyroclastic deposits, which is consistent with the accumulation of hot and still-molten agglutinate. **I.** Clast-supported Pink Pumice and Brown Pumice fall deposits located 9.2 km northwest of vent at location 22.

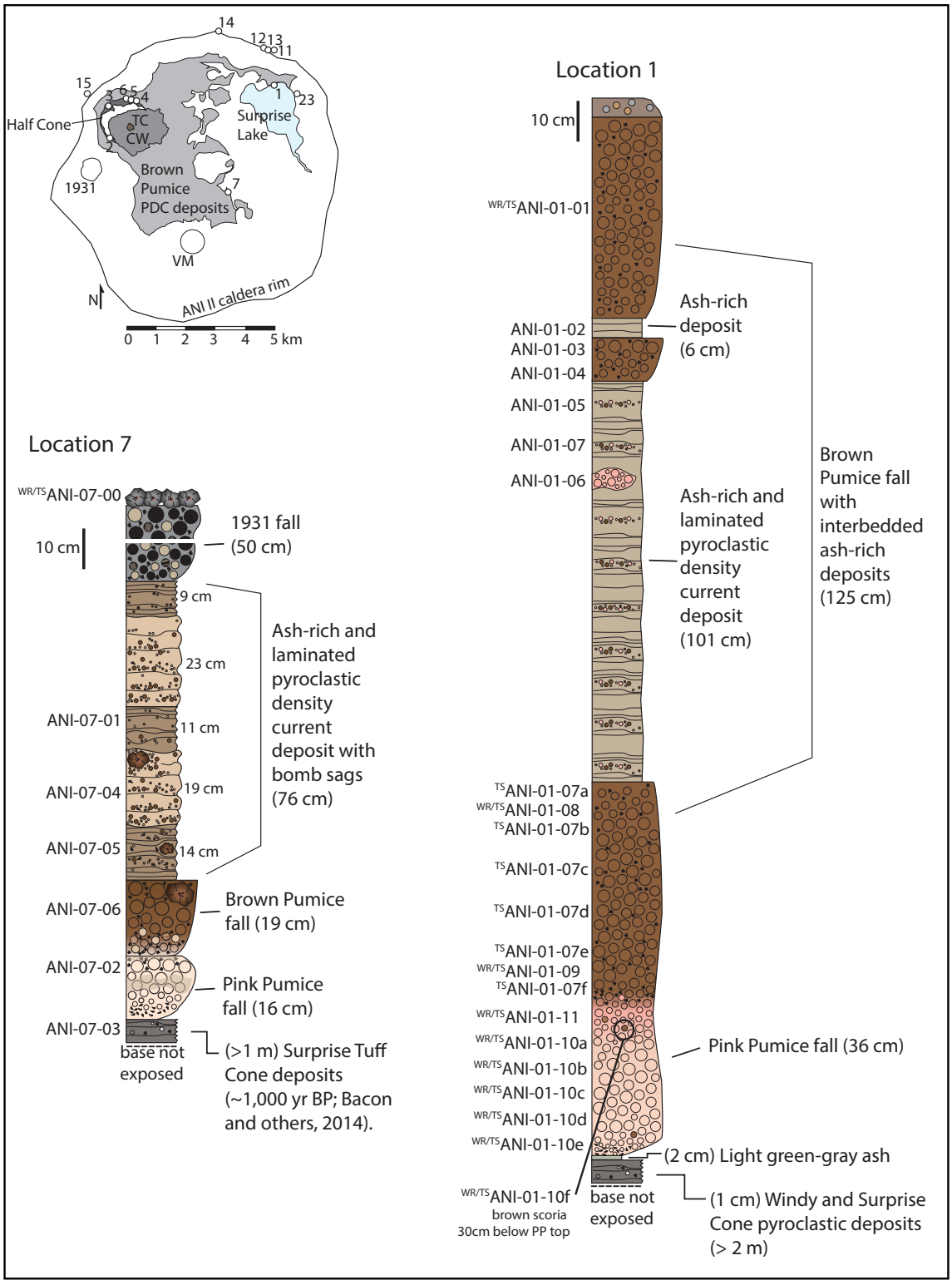

Figure 9. Annotated and measured stratigraphic columns of ~400 yr B.P. tephra at locations 1 and 7, located within the caldera near Pumice Dome and Surprise Cone, respectively. Stratigraphic columns are drawn with a schematic weathered profile instead of a grain-size scale due to abundant fractured and broken pyroclasts in the Pink Pumice and Brown Pumice. Sample numbers indicate those with corresponding whole-rock geochemical data (WR) and petrographic thin section (TS). Inset map shows locations 1 and 7 with respect to the Aniakchak caldera rim, Half Cone, Cobweb lava flow (CW), Cobweb tuff cone (TC), thick and unconsolidated pyroclastic density currents emplaced during Brown Pumice phase, Surprise Lake, and vents of the 1931 eruption and Vent Mountain (VM).

1931 lithic-rich fall deposit marked by black, tan, and banded pumice lapilli overlain by breadcrusted ballistics (Neal and others, 2001).

Exposures of the ~400 yr B.P. tephra in topographic lows within Aniakchak caldera, like the region between Surprise Cone and the Cobweb lava flow (Qht in fig. 2), consist of poorly sorted, matrix-supported, ash-rich pyroclastic density current deposits emplaced during the Brown Pumice phase of the eruption. While exposed thickness of the ash-rich deposits ranges from 1 m to at least 40 m, the total thickness is unknown because underlying fall deposits are not exposed; however, measurements in gullies located in the central caldera indicate a minimum thickness of 40 m (Neal and others, 2001). These deposits are internally stratified with planar and low- to high-angle cross-beds that are traceable for several meters. Lenses of coarse-grained and angular to sub-rounded pyroclasts ranging in color from light pinkish gray to dark brown are common. In-field visual estimates indicate an accidental lithic concentration of approximately 20 percent. Within 2 km of Half Cone, the ash-rich deposits are sometimes capped by an indurated and partially welded spatter agglutinate deposit that correlates to those atop the Half Cone cliffs. Underlying ash-rich deposits were heated and oxidized to an orange-red color when the hot and molten agglutinate and welded spatter layer was deposited.

Tephra Stratigraphy Outside Aniakchak Caldera

The stratigraphy of the ~400 yr B.P. deposit outside the Aniakchak caldera within 10 km of Half Cone is best represented northwest of Half Cone at locations 15 and 18a, and northeast and east of Half Cone at locations 14 and 27, respectively (fig. 10). Two especially conspicuous characteristics of the eruption sequence outside the caldera rim are (1) the scarcity of ash-rich pyroclastic density current deposits in the upper Brown Pumice phase, and (2) two prominent coarse-grained horizons in the Pink Pumice fall marked by pyroclasts that are significantly larger, more vesicular, more oxidized, and more widely impact fractured compared to pyroclasts from layers above and below them (fig. 10). For example, at location 15 situated 2 km west of Half Cone atop the caldera rim, the base of the Pink Pumice grades reversely from an ash- and lithic-rich zone to the first of two coarse-grained horizons marked by large, dark pink pyroclasts that split into pieces when handled. This lower coarse horizon contains pyroclasts and accidental lithics that range up to 13 cm and 3 cm, respectively, while the upper coarse horizon contains pyroclasts and lithics that range up to 43 cm and 16 cm, respectively. The two coarse pumice horizons are separated by 19 cm of clast-supported fall deposit with <1 cm accidental lithics and 2–3 cm pale gray to light pink pyroclasts; both of which show normal grading at the base and reverse grading at the top. Aside from the graded base and top, this portion of the Pink Pumice is otherwise relatively uniform in terms of grain size, color, vesicularity, proportion of accidental lithics, and low degree of oxidation. The upper 12 cm of the Pink Pumice at location 15 grades normally toward the Pink Pumice–Brown Pumice transition (fig. 10).

Exposures of Brown Pumice within 10 km of the Half Cone rim that are located outside of the caldera consist of a nonwelded, clast-supported fall deposit composed of coarse scoria and breadcrust bombs. Accidental lithics account for up to 50 percent of the Brown Pumice base but decrease to 5–15 percent in the middle to upper Brown Pumice fall. At some locations atop the caldera rim, the Brown Pumice contains ash-rich pyroclastic density current deposits interbedded with fall deposits (fig. 10), but these ash-rich layers thin quickly away from the caldera rim. Northwest of Half Cone at location 15, the Brown Pumice fall is 151 cm thick with a reversely graded lithic-rich base. Brown Pumice pyroclasts and breadcrust bombs measure up to 20 cm in the lower 50 cm of the deposit but steadily decrease in size to ~1 cm in the upper 70 cm. An 18 cm thick deposit composed of gray lithic-rich ash is interbedded with the Brown Pumice fall at location 15. Above

the ash bed is a ~10 cm thick horizon of Brown Pumice scoria and breadcrust bombs.

Dispersal of Half Cone Tephra

Isopach maps (fig. 11 A, B) and isopleth maps (fig. 11 C, D) of the Pink Pumice fall deposit and Brown Pumice fall deposit are based on in-field measurements at 28 locations within 80 km of Half Cone. Dashed lines delineate approximate isopach (i.e., tephra thickness) and isopleth (i.e., maximum accidental lithic diameter) contours. The thickness of the Pink Pumice fall deposit is reasonably well constrained within 80 km of Half Cone as a distinct pinkish-beige tephra sandwiched between dark brown soil below and Brown Pumice fall above. In contrast, the full thickness of Brown Pumice fall deposits is less well constrained because these deposits were buried by thick ash-rich deposits of the 1931 eruption in the central caldera or were partially eroded through aeolian and pedogenetic processes beyond the caldera rim. Erosive (i.e., scouring) and undulatory contacts between interbedded pyroclastic fall and flow deposits within proximal Brown Pumice also record removal of

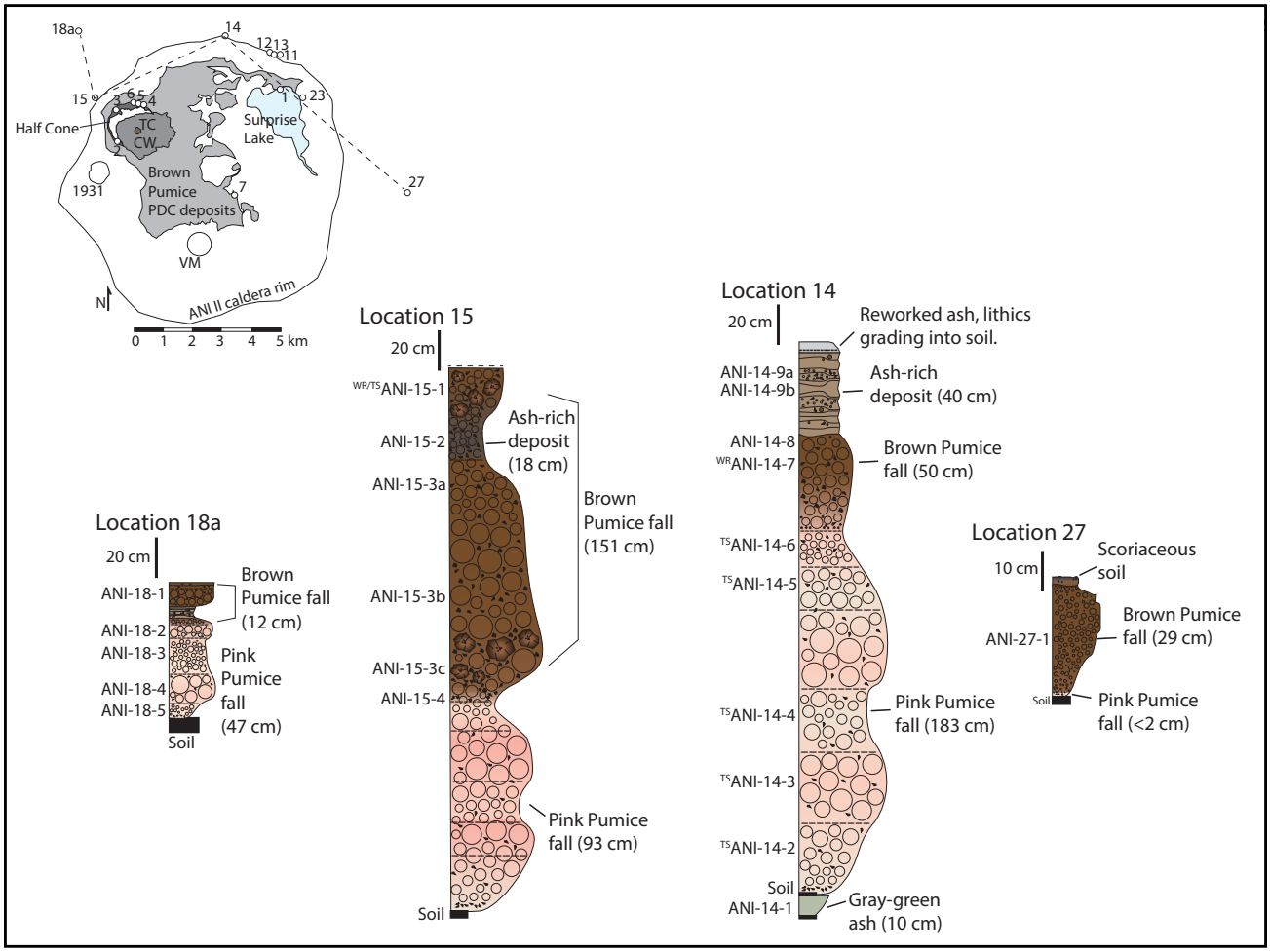

Figure 10. Annotated and measured stratigraphic columns of ~400 yr B.P. tephra at locations 18a, 15, 14, and 27, located outside the caldera at distances of ~2-10 km from vent. Stratigraphic columns are drawn with a schematic weathered profile instead of a grain-size scale due to abundant fractured and broken pyroclasts in the Pink Pumice and Brown Pumice. Fluctuations in pyroclast diameters are more conspicuous at these locations and distances from vent, particularly for Pink Pumice fall deposits. Sample numbers are included adjacent to stratigraphic columns where tephra was collected. Sample numbers indicate those with corresponding whole-rock geochemical data (WR) and petrographic thin section (TS). Inset map shows locations 18a, 15, 14, and 27 with respect to the Aniakchak caldera rim, Half Cone, Cobweb lava flow (CW), Cobweb tuff cone (TC), thick and unconsolidated pyroclastic density currents emplaced during Brown Pumice phase, Surprise Lake, and vents of the 1931 eruption and Vent Mountain (VM).

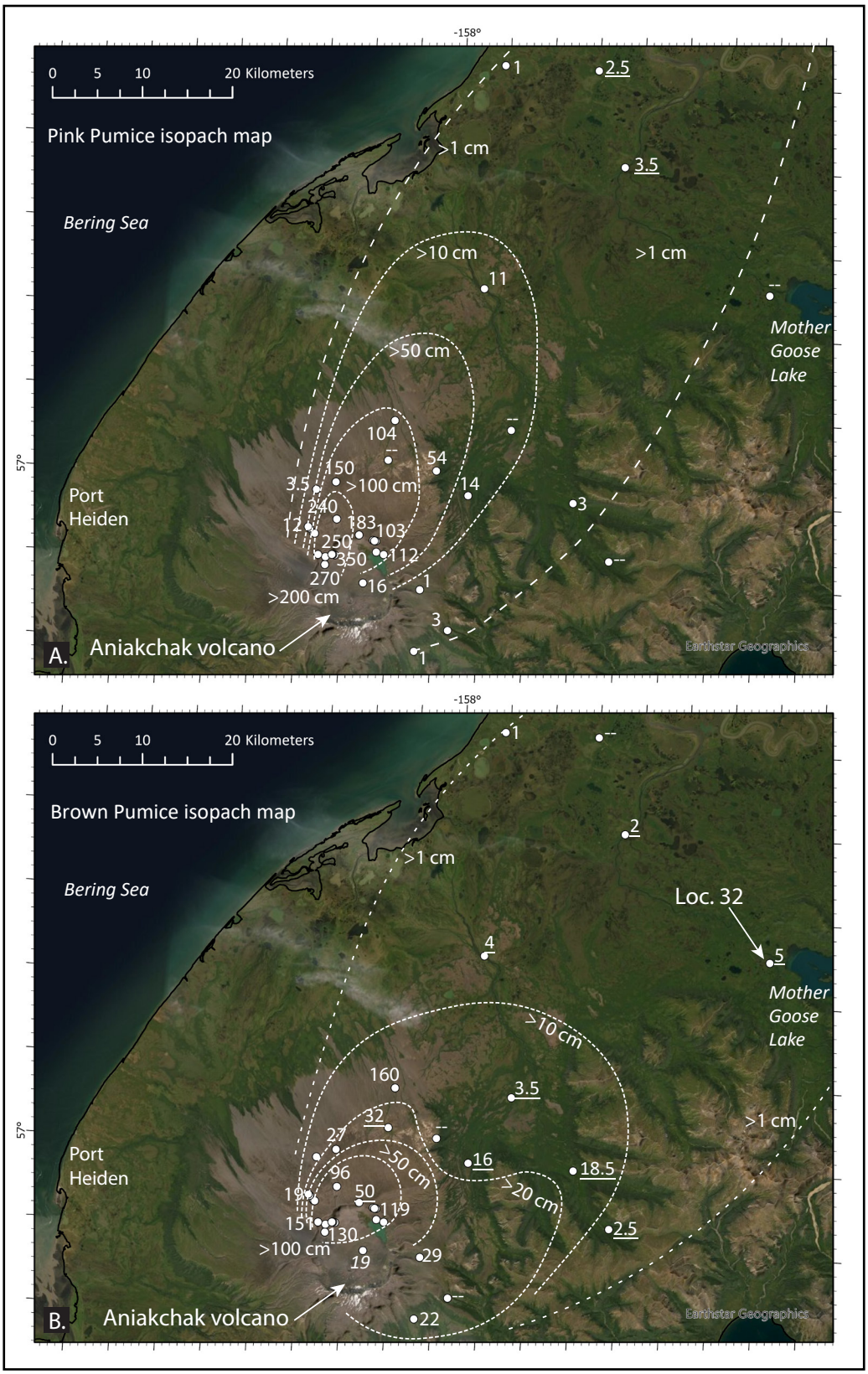

Figure 11. Isopach and isopleth contours of the Pink Pumice and Brown Pumice fall layers. **A.** Isopach contours (in cm) for the Pink Pumice fall layer. **B.** Isopach contours (in cm) for the Brown Pumice fall layer. Numbers adjacent to sample locations (circles) specify measured thickness. Numbers in italics indicate fall deposit thicknesses that are likely incomplete due to erosion of the top. Dashes (--) indicate that the fall deposit was not observed.

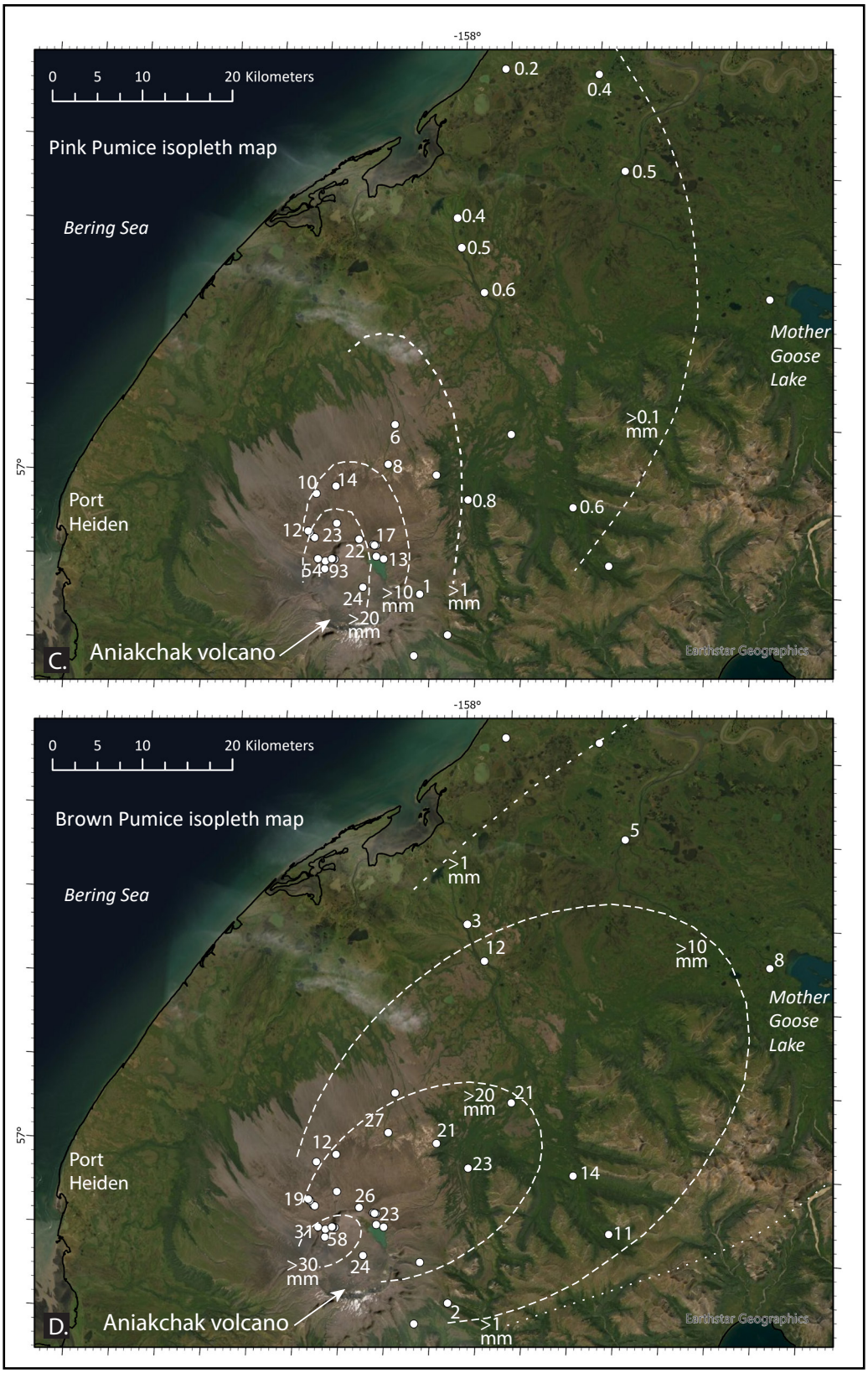

Figure 11, continued. Isopach and isopleth contours of the Pink Pumice and Brown Pumice fall layers. **C.** Isopleth lithic contours (in mm) for the Pink Pumice fall layer. **D.** Isopleth lithic contours (in mm) for the Brown Pumice fall layer. At location 32 near Mother Goose Lake, ~80 km northeast of Half Cone, the Brown Pumice tephra occurs as one stratigraphic layer with shards of Pink Pumice tephra mixed in. Lithic isopleths are based on averaging the five largest lithic fragments at each site in each deposit. Isopleth locations without an adjacent number indicate that maximum lithics were not measured. Closely spaced dashed isopach and isopleth contours indicate higher certainty than contours with dashed lines spaced farther apart.

material. Preservation of Pink Pumice and Brown Pumice deposits beyond 100 km from Half Cone is limited due to very strong winds on the Alaska Peninsula and the widespread presence of wetlands in peninsula lowlands.

The Pink Pumice fall deposit forms a narrow elliptical lobe oriented approximately N30E that extends at least 70 km away from Half Cone (fig. 11A). However, shards of Pink Pumice tephra are found mixed within Brown Pumice tephra layers located far beyond 70 km. The thickest deposit was located on the steep cliffs of the Half Cone edifice and measured 350 cm. The Pink Pumice 100 cm and 10 cm isopachs extend ~20 km and ~40 km away from the volcano, respectively. The deposit measures 35 km across its axis. The thickest unconsolidated Brown Pumice fall deposit (fig. 11B) is located on the steep cliffs of the Half Cone edifice as ~150 cm of clast-supported, nonwelded scoria fall overlain by ~30 m of agglutinate and welded spatter. The deposit forms a much broader elliptical lobe that is approximately twice as wide as the Pink Pumice fall deposit and is oriented approximately N40E away from Half Cone. At location 32 near Mother Goose Lake, ~80 km northeast of Half Cone, the Pink Pumice and Brown Pumice tephras are mixed within one stratigraphic layer that is ~5.5 cm thick (fig. 11B). Although no prominent Pink Pumice horizon was observed beneath the Brown Pumice tephra at location 32, glass analyses of tephra shards from this location indicate that Pink Pumice as well as Brown Pumice clasts occur at this site. Previous work by Riehle and others (2000) suggested that the ~400 yr B.P. Half Cone tephra may occur as a 5–10 cm thick fall deposit of mixed Pink Pumice and Brown Pumice known as "Ash C" in Brooks Camp (fig. 1) located ~230 km northeast of Half Cone on the Alaska Peninsula.

The Cobweb Lava Flow and Cobweb Tuff Cone

The Cobweb lava flow is an approximately circular, blocky lava flow that was emplaced after the deposition of the Pink Pumice and Brown Pumice and collapse of Half Cone but before the formation of the Cobweb tuff cone (fig. 3). Photographs taken by Hubbard in 1930 (prior to the 1931 eruption) reveal a lava flow characterized by (1) steep autobrecciated flow fronts up to 50 m tall; (2) a jagged, blocky surface with spires, pressure ridges, and well-developed levees; and (3) a tuff cone slightly off-center of the lava flow (fig. 3C; Hubbard, 1931). Both the Cobweb lava flow and Cobweb tuff cone were covered by thick 1931 tephra fall deposits (Hubbard, 1931, 1932a; Neal and others, 2001; Nicholson and others, 2011), and although still plainly visible, surface structures currently are less obvious than in Hubbard's photographs. Aerial photographs clearly show that the 2 km east-west by 1.6 km north-south lava flow spread radially into at least six flow lobes from a vent located slightly west of the lava flow center. That vent region is now concealed beneath the 190 m wide and 40 m tall Cobweb tuff cone. The tuff cone itself is a lithic-dominated, unconsolidated pile of blocky, angular, poorly vesicular ash- and lapilli-sized pyroclasts that range in color from light beige to dark gray. Pyroclasts with compositional banding are more abundant in Cobweb tuff cone deposits (fig. 3D) than in the Pink Pumice and Brown Pumice fall; however, pyroclasts without compositional banding are more common overall in Cobweb tuff cone deposits.

WHOLE-ROCK GEOCHEMISTRY

Major- and trace-element concentrations of 76 pyroclast and lava samples from Half Cone that were sampled in 1992 and 1993 by C. Neal and R. McGimsey, in 1997 by C.R. Bacon, and in 2002 by B. Browne and C. Neal are described here (app. C). These major- and trace-element concentrations are also included in appendix B of Bacon and others (2014), who presented them within the scope of all postglacial deposits erupted from Aniakchak volcano. We discuss major- and trace-element compositions of material erupted ~400 yr B.P. in the context of the eruption stratigraphy.

Pink-colored pyroclasts plot as dacite based on the scheme of Le Bas and others (1986), ranging

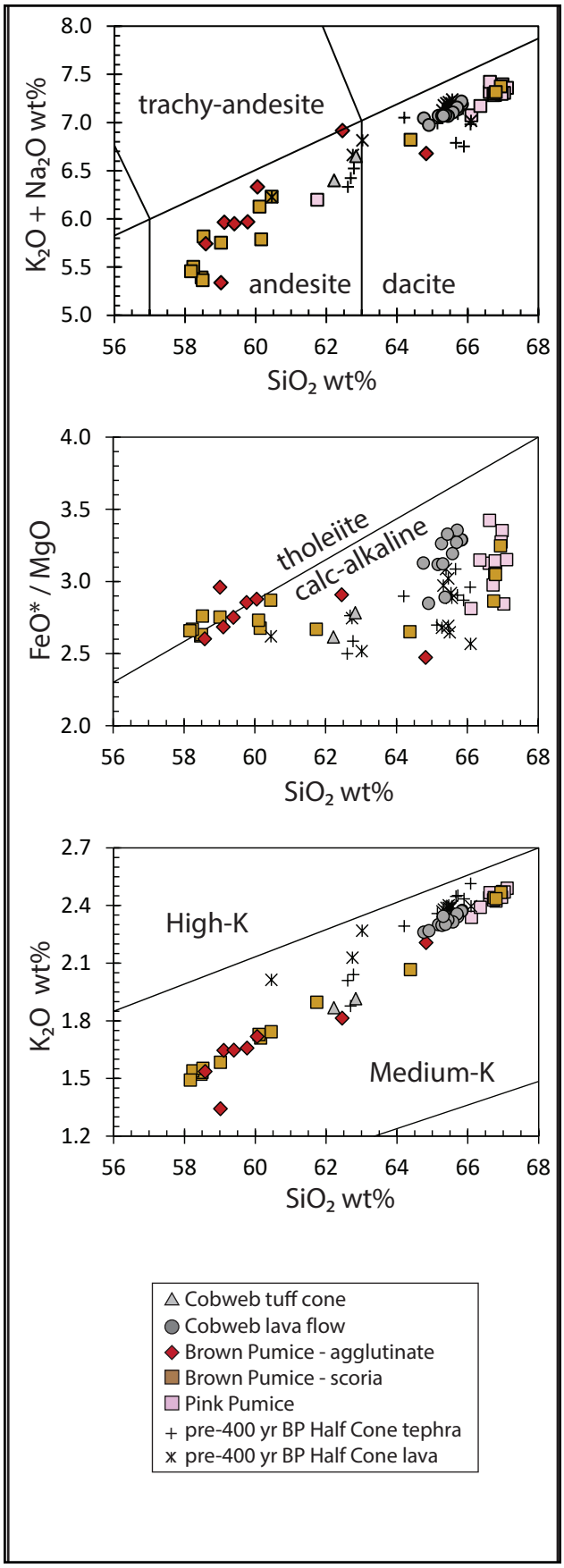

narrowly from 66.1 to 67.1% SiO_2 (fig. 12; table 1). Brown-colored andesite to dacite pyroclasts range from 58.2 to 66.9% SiO_2, but many whole-rock geochemical plots show a bimodal distribution of Brown Pumice scoria compositions, each of which comprises a narrow range. Most brown-colored pyroclasts cluster at the lower end of the SiO_2% range (58.2 to 60.5% SiO_2)—referred to here as "low-SiO_2" Brown Pumice. The higher silica population of brown-colored pyroclasts—referred to here as "high-SiO_2" Brown Pumice—ranges from 61.7 to 66.9% SiO_2. Interestingly, low-SiO_2 and high-SiO_2 Brown Pumice scoria are indistinguishable in hand sample. Agglutinate deposited during the end of the Brown Pumice phase of the eruption range from 58.6 to 64.8% SiO_2, which partially fills in the compositional range between the Brown Pumice compositional endmembers. Cobweb lava flow samples (64.8–65.8% SiO_2) and pyroclasts from the Cobweb tuff cone (62.2–62.8% SiO_2) have a narrower compositional range and plot either intermediately to the Pink Pumice and Brown Pumice compositional endmembers or similarly to Pink Pumice and high-SiO_2 Brown Pumice samples. Samples have FeO*/MgO ranging from 2.5 to 3.4 (FeO* = FeO_T) and medium-K trends based on Le Maitre (1989; figs. 12, 13). The majority of samples from the ~400 yr B.P. eruption (and Half Cone in general) are calc-alkaline except for the more mafic population of Brown Pumice pyroclasts, which plot in the tholeiitic field on the SiO_2 versus FeO*/MgO diagram (fig. 12).

Most major elements plot linearly with SiO_2: where TiO_2, FeO_T, MgO, MnO, and CaO are

Figure 12. Weight percent major element concentrations of Pink Pumice (pink squares), Brown Pumice (brown squares), Cobweb lava flow (gray circles), Cobweb tuff cone (gray triangles), as well as pre-400 yr B.P. Half Cone lavas (✖) and tephra (+) plotted against concentration SiO_2 wt%. FeO* indicates all Fe calculated as FeO. Rock names from Le Bas and others (1986) and high-, medium-, and low-K fields based on Le Maitre (1989). Tholeiite–calc-alkaline partition from Miyashiro (1974). Symbol size is larger than the 1σ uncertainty for all samples.

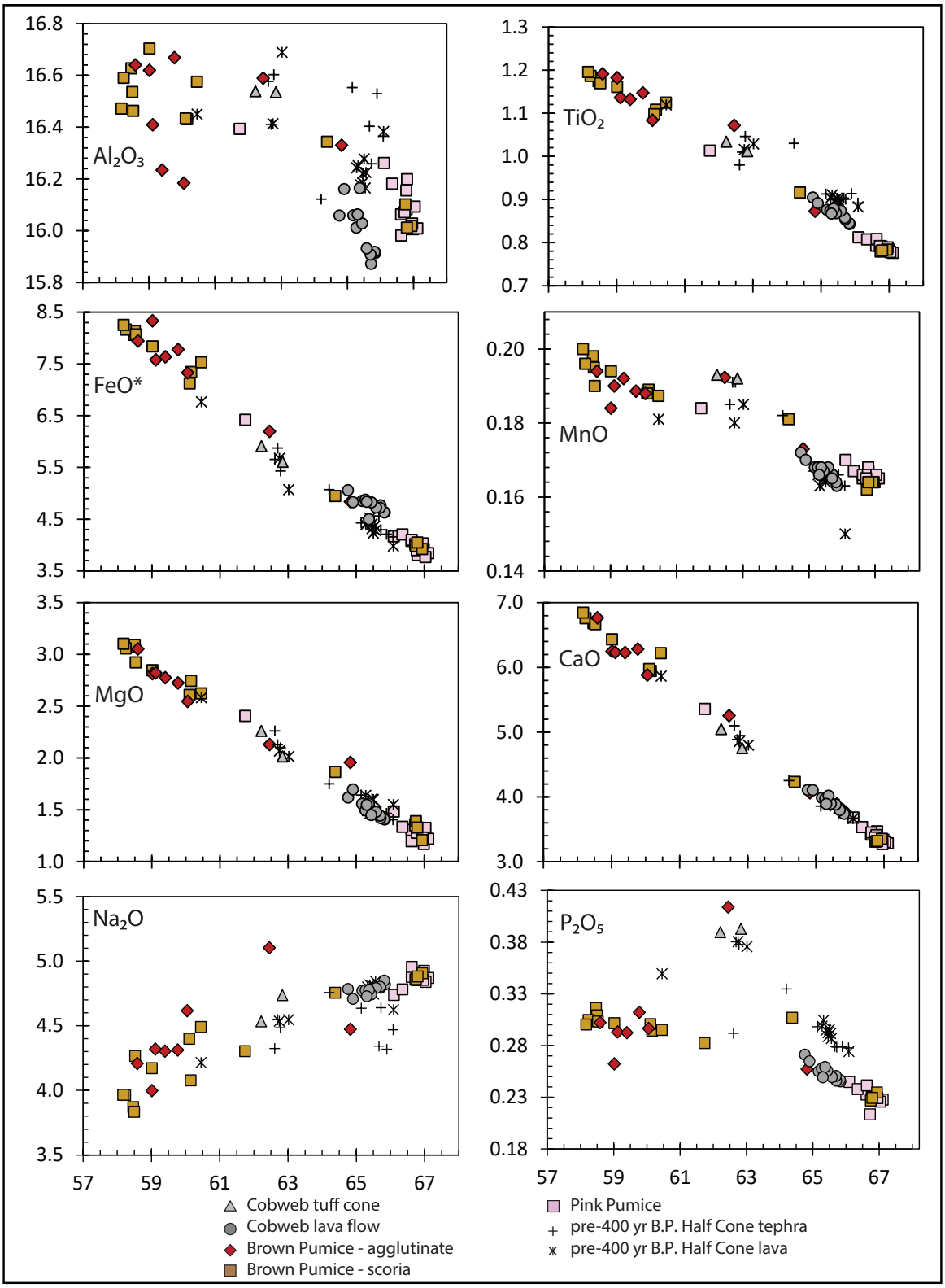

Figure 13. Major element concentrations of samples (in wt%) plotted against SiO_2 wt% from ~400 yr B.P. and pre-400 yr B.P. Half Cone lavas and tephra. The symbols used are the same as those in figure 12. Symbol size is larger than the 1σ uncertainty for all samples. Note the scatter in Na_2O and Al_2O_3 and diverging trends in P_2O_5. Also note how Cobweb lava flow samples plot along distinct trends for Al_2O_3, FeO*, and MnO. Pre-400 yr B.P. samples also plot along distinct trends of TiO_2, and P_2O_5.

negatively correlated to SiO_2, K_2O, and Na_2O are positively correlated (fig. 13). Plots of some major elements, however, are more complicated. For example, concentrations of Al_2O_3 and MnO in Cobweb lava flow samples form trends parallel to, but offset from, Pink Pumice and Brown Pumice trends. In addition, concentrations of Al_2O_3, MnO, and P_2O_5 in Cobweb tuff cone samples more closely resemble pre-400 yr B.P. tephra and lava from Half Cone than Pink Pumice and Brown Pumice samples. Concentrations of Al_2O_3 and P_2O_5 are generally negatively correlated to SiO_2, although these elements are more scattered than other major elements (fig. 13). Plots of P_2O_5 against SiO_2 (and K_2O and V, not shown in fig. 13) reveal two offset trends for samples with >62% SiO_2.

Concentrations of most trace elements generally form linear trends with Zr (fig. 14); however, trends in Sc, Ni (≤6 ppm), and Cr (≤13 pm) are more scattered. Low-SiO_2 Brown Pumice pyroclasts have the lowest Zr and are consistently higher in Cr, Sc, V, and Sr compared to other ~400-yr B.P. deposits (fig. 14). Low-SiO_2 Brown Pumice pyroclasts also have consistently lower Ba, Rb, Y, and Nb concentrations and the lowest La/Yb ratios. V, Sr, and Ta negatively correlate with Zr, whereas Ba, Rb, Y, and Nb positively correlate with Zr. Ni/Sc are <1 and generally negatively correlate with Sc, whereas La/Yb are low (<6) and positively correlate with La. Concentrations of incompatible elements like Ta and Zr correlate negatively with MgO%.

Similar to some major elements, some plots of trace elements (e.g. Sr, Ba, V) reveal trends for Brown Pumice that are parallel to—and offset from—Cobweb lava flow samples (fig. 14). For example, K_2O/P_2O_5, which is a proposed indicator of crustal assimilation (e.g., Pearce and others, 1975; Farmer and others, 2002; Putirka and others, 2012; Browne and others, 2017), positively corelate with Zr and plot as displaced trends, where Pink Pumice and Brown Pumice samples, Cobweb lava flow samples, and Cobweb tuff cone samples plot as distinct but roughly parallel groups. As observed for some major elements, Cobweb tuff cone samples plot with pre-400 yr B.P. tephra and lava from Half Cone rather than with samples of the Pink Pumice and Brown Pumice or Cobweb lava flow.

To see a clearer picture of how different compositions of magma were emplaced over time during the eruption, concentrations of major and trace elements in the ~400 yr B.P. deposit were also plotted as a function of relative stratigraphic order (figs. 15, 16). Most of these samples were collected from the tephra sections at locations 1 and 2 (figs. 7 and 9; app. 1) and are combined with samples from the subsequently emplaced Cobweb lava flow and Cobweb tuff cone. The concentrations of most major elements in Pink Pumice pyroclasts are relatively constant except for Al_2O_3, which appears to increase with stratigraphic height. Two compositionally distinct populations of Brown Pumice scoria—a low-SiO_2 and a high-SiO_2 Brown Pumice—were erupted simultaneously during the early Brown Pumice phase although the more silicic population decreased in abundance until only the more mafic population was deposited later in this phase. Compositions of agglutinate and spatter emplaced at the end of the Brown Pumice phase plot as a continuum between the low-SiO2 and high-SiO_2 Brown Pumice endmembers. Cobweb lava flow samples and pyroclasts from the Cobweb tuff cone generally plot between the Pink Pumice and Brown Pumice endmembers in all major and trace elements with the exception of Al_2O_3 in some lavas, which plot lower than other ~400 yr B.P. deposits (figs. 15, 16).

Plots of the concentration of major and trace elements in ~400 yr B.P. samples as a function of relative stratigraphic order suggest that pyroclast color may be a misleading indicator of magma composition. For example, pink-colored pyroclasts sampled from the contact between the Pink Pumice and Brown Pumice phases are intermediate between the Pink Pumice/high-SiO_2 Brown Pumice endmembers and the low-SiO_2 Brown Pumice endmember. Another example is high-SiO_2 Brown Pumice scoria that was erupted at the start of the Brown Pumice phase, which is virtually

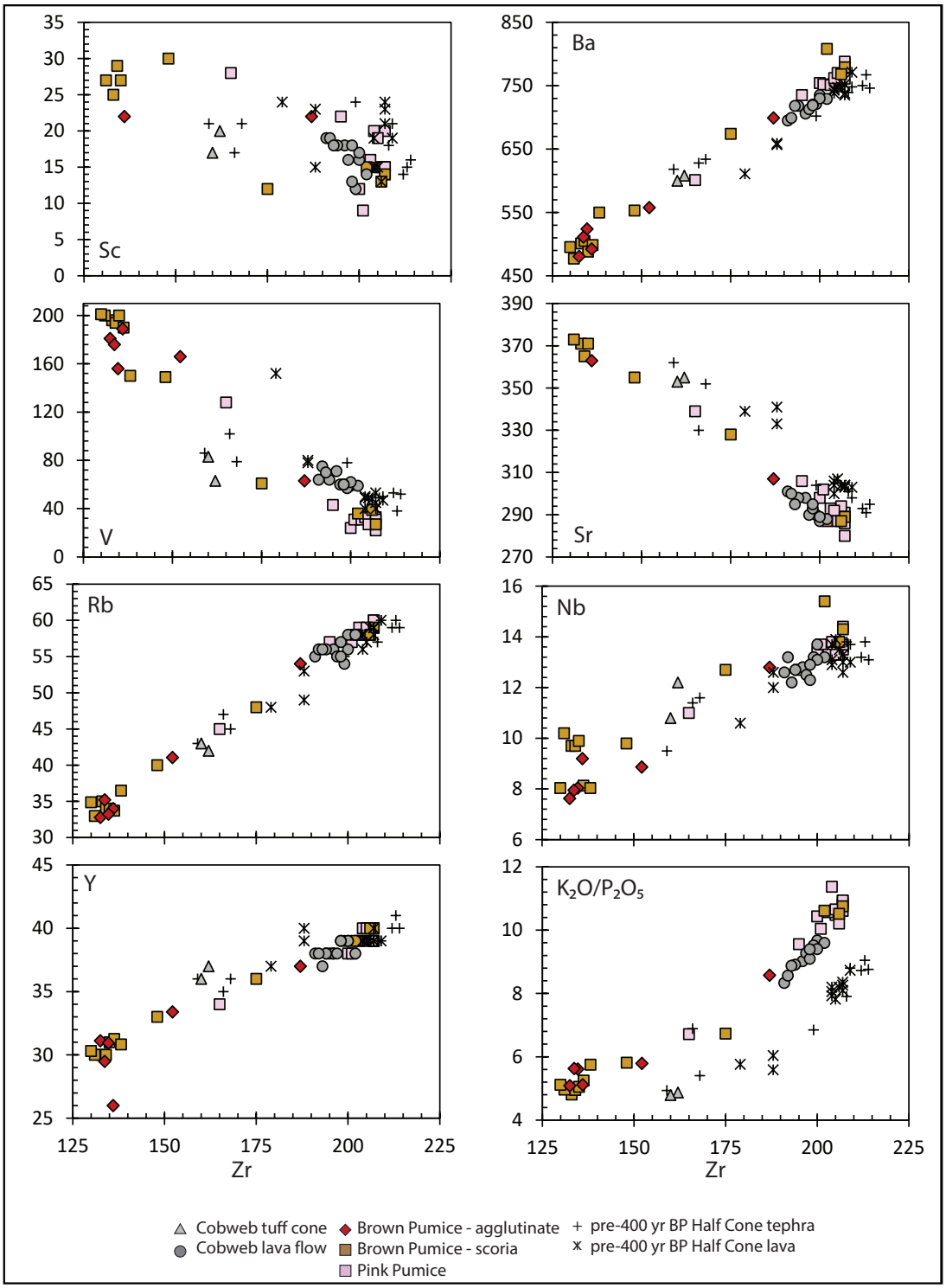

Figure 14. Trace element concentrations of tephra and lava samples (in ppm) plotted against Zr (ppm) from ~400 yr B.P. and pre-400 yr B.P. Half Cone lavas and tephra. The same symbols are used as in figure 12. Many Half Cone samples show deposit-specific trends in trace element concentrations including Ba, Sr, and V, where trends formed by Pink Pumice, Brown Pumice, Cobweb lava flow, and pre-400 yr B.P. samples plot along arrays that are subparallel to but offset from each other. For example, K_2O/P_2O_5, a proposed indicator of crustal contamination (e.g., Pearce and others, 1975; Farmer and others, 2002; Putirka and others, 2012; Browne and others, 2017), also shows deposit-specific trends and indicates that Pink Pumice samples correspond with the highest extent of crustal contamination, where some samples from the Brown Pumice, Cobweb tuff cone, and pre-400 yr B.P. tephra are the least contaminated by crust.

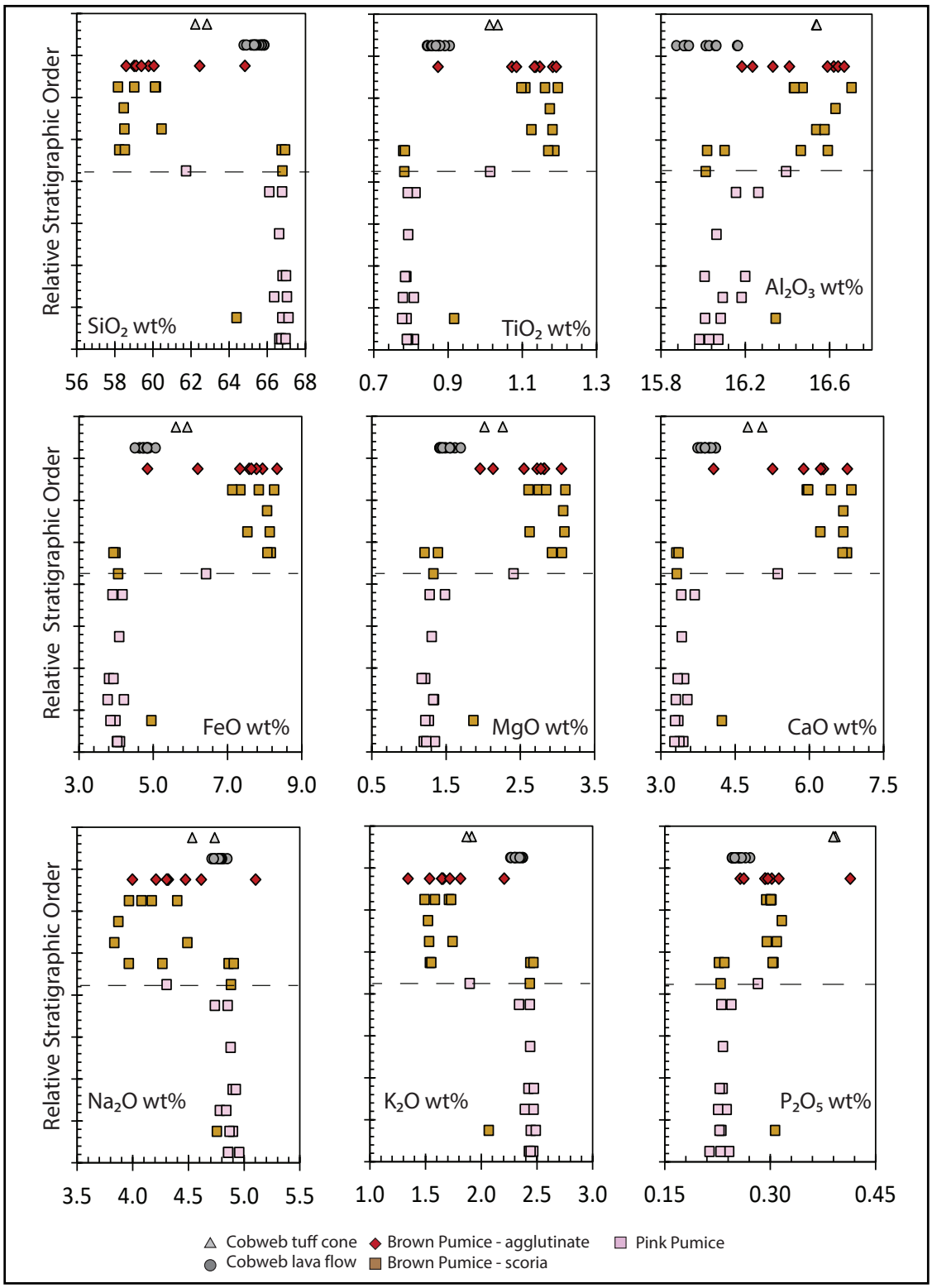

Figure 15. Major element concentrations measured by XRF of tephra and lava samples (in wt%) plotted as a function of relative stratigraphic order. Symbols are the same as in figure 12. Symbol size is larger than the 1σ uncertainty for all samples. The dashed line corresponds to the depositional contact of the Pink Pumice and Brown Pumice as observed in the field. Pyroclasts that displayed compositional banding were not selected for whole-rock analyses. Note the gradual increase with stratigraphic height of Al_2O_3 for many pyroclast samples. Some brown-colored pyroclasts from the Pink Pumice (and pink-colored pyroclasts from the Brown Pumice) are compositionally intermediate between Pink and Brown Pumice endmembers.

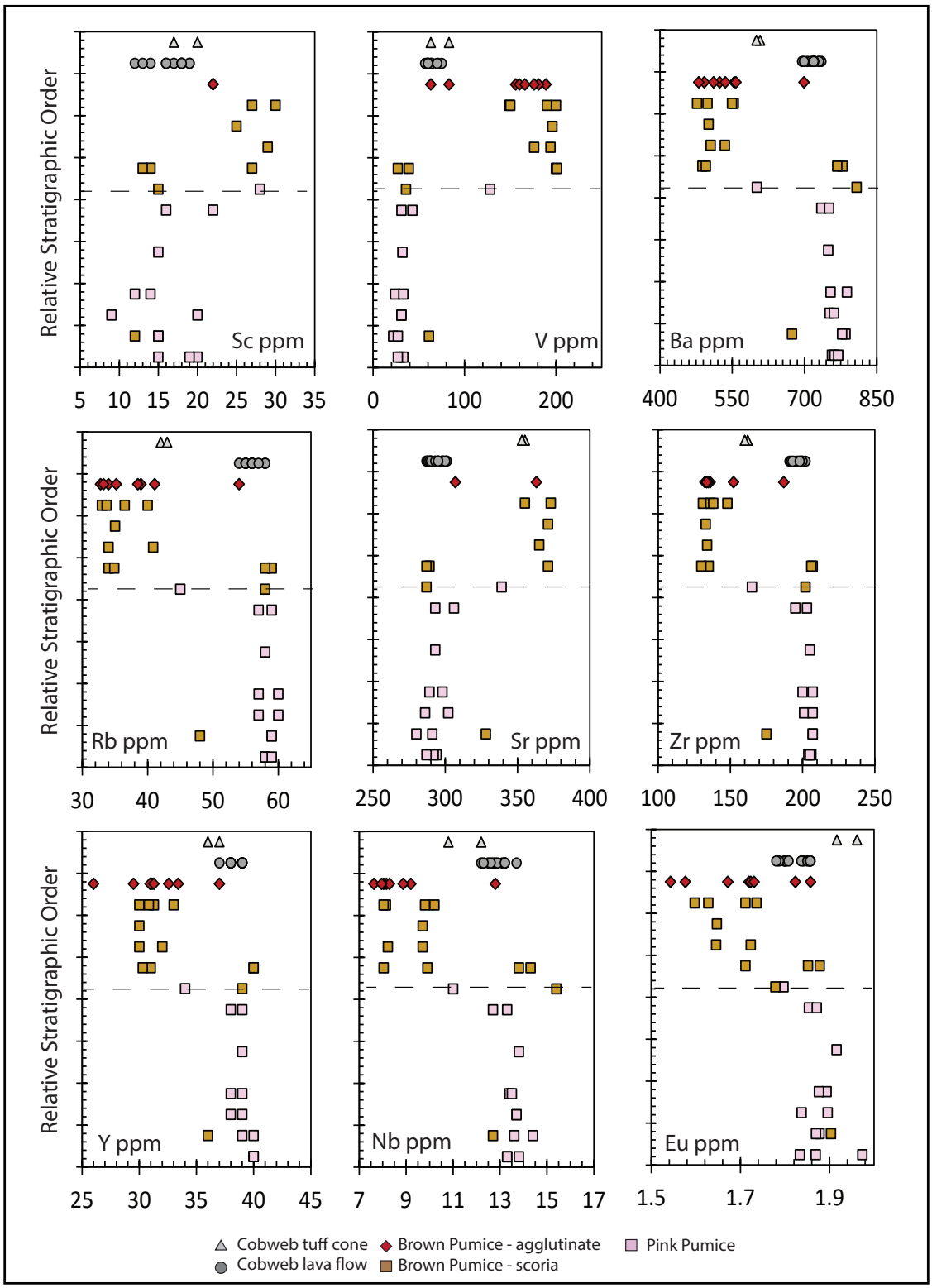

Figure 16. Trace element concentrations (in ppm) of samples measured by XRF (Sc, V, Ba, Rb, Sr, Zr, Y, and Nb) and ICP-MS (Eu) plotted as a function of relative stratigraphic order. Symbols are the same as those in figure 12. The dashed line corresponds to the depositional contact of the Pink Pumice and Brown Pumice as observed in the field. Pyroclasts that displayed compositional banding were not selected for whole-rock analyses. As in figure 15, some brown-colored pyroclasts from the Pink Pumice (and pink-colored pyroclasts from the Brown Pumice) are compositionally intermediate between Pink and Brown Pumice end members.

identical in composition to pink-colored pyroclasts erupted during the Pink Pumice phase. Finally, brown-colored pyroclasts sampled from the lower Pink Pumice are intermediate between low-SiO_2 Brown Pumice scoria and Pink Pumice/high-SiO_2 Brown Pumice pyroclasts. This lack of correlation between color and composition of pyroclasts—that do not show evidence of compositional banding in hand sample or thin section—appears to be the strongest evidence that hybrid magmas erupted during the Pink Pumice and Brown Pumice phases of the eruption.

PETROGRAPHY AND MINERAL AND GLASS COMPOSITIONS

Petrography and Plagioclase Compositions

In this section, we describe the petrographic characteristics of pyroclasts and lava erupted during the ~400 yr B.P. eruption, all of which contain plagioclase as the dominant mineral phase with lesser amounts of orthopyroxene (OPX), clinopyroxene (CPX), magnetite, and ilmenite (figs. 17, 18). Analyses of plagioclase are presented in appendix D. We also describe compositional characteristics of plagioclase based on back-scattered electron imaging and core-to-rim analyses via electron microprobe (fig. 19). Compositions of touching magnetite and ilmenite crystals as well as geothermometry calculations are presented in appendix F and are considered in the Discussion section.

Pink Pumice pyroclasts are highly vesicular with a colorless, microlite-poor matrix glass and a uniformly low concentration of phenocrysts (~1–2 percent; fig. 17). Vesicles range from spherical to elongate, with the most extensively stretched vesicles resembling string-like fibers. High-SiO_2 Brown Pumice scoria resembles Pink Pumice samples in terms of low crystallinity (~1–5 percent) and a microlite-poor matrix glass but the matrix glass is darker (fig. 18). Low-SiO_2 Brown Pumice scoria is also highly vesicular and contains a low concentration of phenocrysts (~1–5 percent) but is distinguished by its dark brown matrix glass and higher concentration of microlites. Compositional banding in some Pink Pumice and Brown Pumice pyroclasts is marked by ~mm-thick zones defined by darker and lighter matrix glass, and by crystallinity differences (fig. 17G). OPX and CPX in both Pink Pumice and Brown Pumice often contain opaque mineral inclusions and display simple twinning and euhedral forms with tabular to equant habits depending on their orientation in thin section. Pink Pumice and Brown Pumice pyroclasts also contain angular shards of accidental lithics that average 1–2 mm in diameter.

Plagioclase diameters range from 0.2 to 1 mm and 0.2 to 2 mm in Pink Pumice and Brown Pumice, respectively. Pink Pumice and Brown Pumice contain plagioclase as individual crystals surrounded by vesicular and glassy groundmass as well as in glomerocrysts. In Pink Pumice and high-SiO_2 Brown Pumice pyroclasts, about a third of individual plagioclase crystals are clear, unzoned, and tabular with albite and Carlsbad twinning; another third show oscillatory zoning; and the remaining third occur as broken shards that may have formed due to fragmentation (e.g., Best and Christiansen, 1997). The majority of oscillatory-zoned plagioclase in the Pink Pumice fall deposits record compositions ranging from ~An_{40} to ~An_{55} and do not show systematic differences between core and rim compositions (figs. 19, 20). However, some oscillatory zoned plagioclase, contain normally zoned interiors wrapped in disconformity-like dissolution zones and reversely zoned exteriors with elevated FeO% (fig. 21B). The proportion of these reversely zoned plagioclase steadily increases through the tephra stratigraphy—only one in 10 plagioclase selected for analysis in the basal Pink Pumice are reversely zoned compared to nearly half of plagioclase in the Brown Pumice fall (fig. 20).

One prominent difference between the plagioclase populations in low-SiO_2 Brown Pumice compared to Pink Pumice and high-SiO_2 Brown Pumice is the regular occurrence of coarsely sieved plagioclase in low-SiO_2 Brown Pumice pyroclasts

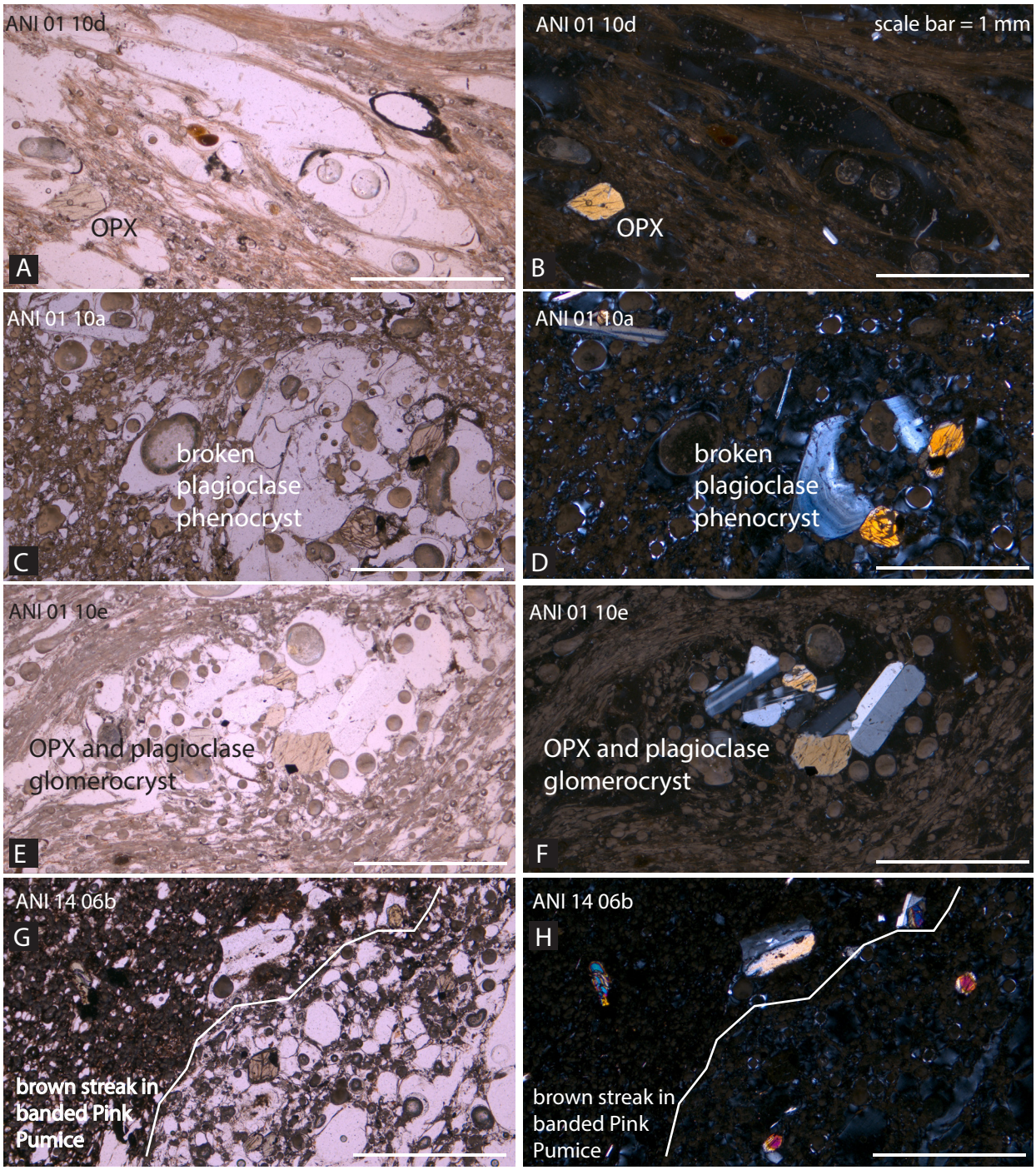

Figure 17. Photomicrographs of Pink Pumice pyroclasts. Scale bar for all images is 1 mm. **A, B**. Plane-polarized (A) and cross-polarized (B) view of sparse CPX crystal set in highly stretched vesicles of Pink Pumice pyroclast from sample ANI-01-10d (location 1). C, D. Plane-polarized (C) and cross-polarized (D) view of tabular (upper left) and oscillatory-zoned (lower right) plagioclase crystals with CPX set in highly vesicular pyroclast from sample ANI-01-10a (location 1). Note that the oscillatory-zoned plagioclase has been split apart, possibly due to vesiculation of melt entrapped by the plagioclase at higher pressures (e.g., Best and Christiansen, 1997). **E, F**. Plane-polarized (E) and cross-polarized (F) view of hypidiomorphic granular glomerocryst with plagioclase, OPX, CPX, and FeTi oxides set in highly vesicular pyroclast from sample ANI-01-10e (location 1). **G.** Plane-polarized view of banded pumice from sample ANI-14-06b (location 14), where a darker and less vesicular groundmass of a brown streak is on left side of photomicrograph adjacent to a lighter and more vesicular groundmass of the Pink Pumice pyroclast.

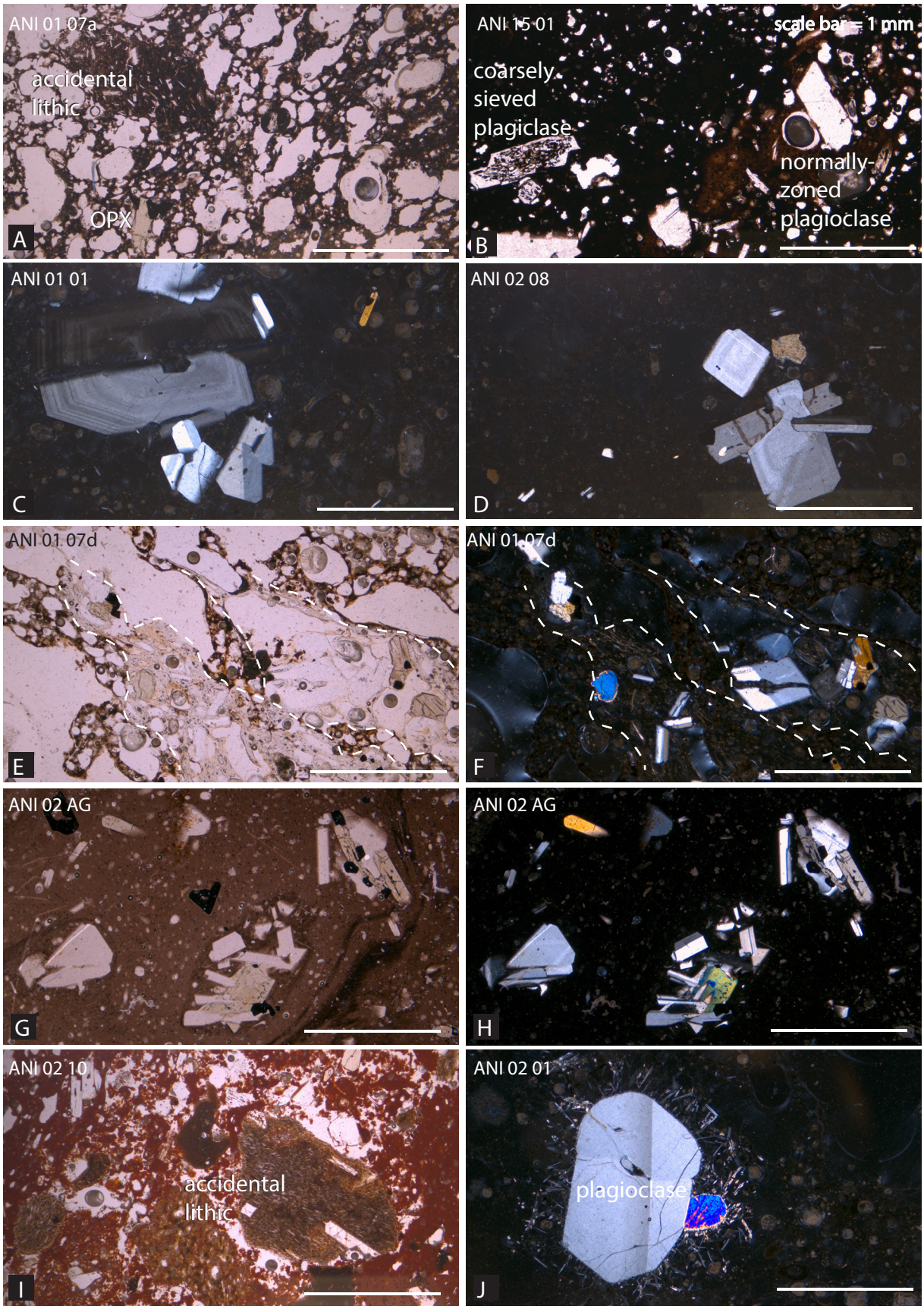

Figure 18. See caption on following page.

and Brown Pumice agglutinate (figs. 19–22). These coarsely sieved plagioclase are identified by a sponge-like texture in the crystal interiors characterized by abundant brown melt inclusions with diameters ranging between 10 and 50 μm. Core-to-rim transects of coarsely sieved plagioclase resemble steep sided plateaus with relatively uniform concentrations of significantly higher anorthite (An_{79}–An_{92}) and FeO% (0.7–0.9 wt%) in the crystal interiors enclosed by <10-μm-thick rims characterized by far lower concentrations of anorthite and FeO%. The interiors of coarsely sieved plagioclase contain significantly higher anorthite and FeO% concentrations compared to other types of plagioclase, whereas their rim compositions approach—but do not uniformly match—the rim compositions of other plagioclase crystals observed in Half Cone samples (An_{55}–An_{65}; figs. 20, 22).

Glomerocrysts in Pink Pumice and Brown Pumice are common and show idiomorphic granular texture with a mineralogy consisting of plagioclase adjoined to OPX, CPX, apatite, magnetite, and/or ilmenite (figs. 17, 18). In these glomerocrysts, euhedral plagioclase forms sharp contacts with adjacent pyroxenes and FeTi oxides. Some Brown Pumice scoria contain glomerocrysts with hypidiomorphic granular texture, where subhedral plagioclase forms curved and penetrating boundaries to adjacent intergrown pyroxenes. Plagioclase in glomerocrysts from Pink Pumice and Brown Pumice as well as the Cobweb lava flow also record crystallization from a more mafic melt (fig. 20) compared to individual plagioclase. That is, core regions of plagioclase in glomerocrysts typically range from An_{50} to An_{78}, which is higher than many individual crystals but lower than the coarsely sieved plagioclase present in Brown Pumice deposits. Rims of glomerocrystic plagioclase approach those observed in other individual plagioclase crystals (fig. 20).

Indurated and partially welded agglutinate and spatter deposits emplaced on and near Half Cone flanks near the end of the Brown Pumice phase were also examined in thin section. Scoria and agglutinate lenses contain 5–10 percent crystals and small accidental lithics with yellow and orange margins set in a poorly vesicular groundmass stained crimson due to heating and oxidation processes (fig. 18). Scoria typically possesses a devitrified groundmass compared to welded agglutinate samples, which usually possess a vitrophyric groundmass. Some plagioclase and CPX crystals have rounded margins and are enclosed by reaction rims (fig. 18J). Many crystals occur as angular broken shards. Black, matrix-supported, vitrophyric deposits contain ~5 percent accidental lithics and 10–25 percent crystals suspended in a eutaxitic groundmass with micron-scale flow bands that curve between and around crystals. About half of the crystallinity is accounted for by glomerocrysts. Individual plagioclase typically

Figure 18, page 33 (previous). Photomicrographs of Brown Pumice pyroclasts. Scale bar for all images is 1 mm. **A.** Plane-polarized view of Brown Pumice scoria with rounded vesicles, accidental lava lithic, and OPX crystal from sample ANI-01-07a (location 1). **B.** Plane-polarized view of low-SiO_2 Brown Pumice scoria with rounded vesicles, dark brown matrix glass, coarsely sieved plagioclase (lower left), and normally -zoned plagioclase (upper right) from breadcrust bomb sample ANI-15-01 (location 15). **C.** Cross-polarized view of oscillatory zoned plagioclase in hypidiomorphic glomerocryst with CPX set in vesicular scoria from sample ANI-01-01 (location 1). **D.** Cross-polarized view of oscillatory zoned plagioclase in allotriomorphic granular glomerocryst with OPX, CPX, and opaque FeTi oxides set in vesicular scoria from sample ANI-02-08 (location 2). **E, F.** Plane-polarized (E) and cross-polarized (F) view of Brown Pumice scoria with dashed lines marking smears of crystal-rich (plagioclase, CPX, OPX, and FeTi oxides) zones set in a groundmass that is less vesicular and lighter colored compared to the Brown Pumice scoria groundmass from sample ANI-01-07d (location 1). **G, H.** Plane-polarized (G) and cross-polarized (H) view of sample from partially welded deposit emplaced during the Brown Pumice phase on the Half Cone cliffs (sample ANI-02-AG, location 2). Partially welded samples display eutaxitic and vitrophyric textures with hypidiomorphic and allotriomorphic granular glomerocrysts of plagioclase, CPX, OPX, and FeTi oxides. **I.** Plane-polarized view of sample of thoroughly oxidized spatter with abundant accidental lithics emplaced during the Brown Pumice phase of the eruption (sample ANI-02-10, location 2). **J.** Cross-polarized view of Brown Pumice agglutinate (sample ANI-02-01, location 2) with a glomerocryst composed of rounded plagioclase with prominent Carlsbad twin and CPX enclosed by a reaction rim of radiating and acicular plagioclase, FeTi oxides, and CPX.

	Texture and composition	Eruption phase(s)
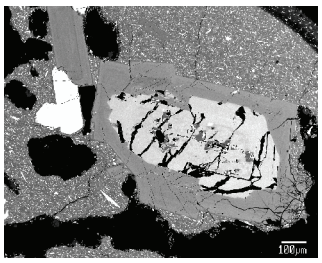	Plagioclase with An_{80} to An_{92} core regions that are rounded and fractured with inclusions of CPX, FeTi oxide, and apatite. Cores are enclosed by a thick euhedral 50-160-um rim with abruptly lower An (An_{52}-An_{60}).	☐Cobweb tuff cone ■Cobweb lava flow ☐Brown Pumice agglutinate ☐Low-SiO_2 Brown Pumice fall ☐High-SiO_2 Brown Pumice fall ☐Pink Pumice fall
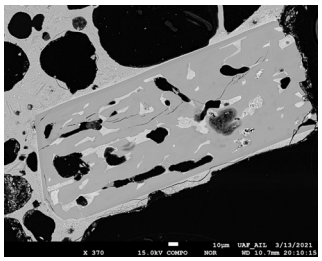	Coarsely sieved plagioclase with An_{76} to An_{91} cores marked by irregular melt inclusions and dissolution textures enclosed by ~10-um-wide rims with abruptly lower An content (An_{55} to An_{65})	☐Cobweb tuff cone ☐Cobweb lava flow ■Brown Pumice agglutinate ■Low-SiO_2 Brown Pumice fall ☐High-SiO_2 Brown Pumice fall ☐Pink Pumice fall
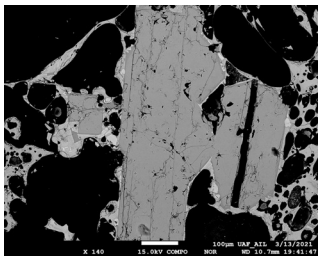	Plagioclase with unzoned An_{88}-An_{92} core regions enclosed by ~10-um rims with abruptly lower An content ranging from An_{55} to An_{67}	☐Cobweb tuff cone ☐Cobweb lava flow ■Brown Pumice agglutinate ■Low-SiO_2 Brown Pumice fall ☐High-SiO_2 Brown Pumice fall ☐Pink Pumice fall
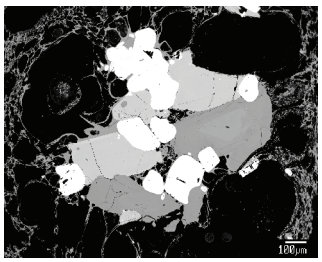	Normally- and oscillatory-zoned plagioclase in glomerocrysts with pyroxene, magnetite, ilmenite, and apatite with core regions ranging from An_{48} to An_{87} and rims ranging from An_{32} to An_{65}.	■Cobweb tuff cone ■Cobweb lava flow ■Brown Pumice agglutinate ■Low-SiO_2 Brown Pumice fall ■High-SiO_2 Brown Pumice fall ■Pink Pumice fall
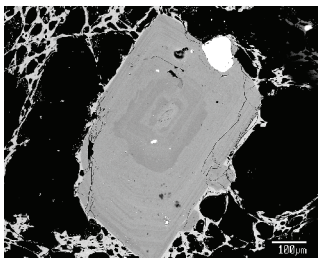	Plagioclase with repeating normal- and oscillatory-zoning patterns bound by dissolution surfaces. An_{50}-An_{55} regions normally zone to An_{40}-An_{45} regions over 100-150 um distances from core to rim.	☐Cobweb tuff cone ■Cobweb lava flow ■Brown Pumice agglutinate ■Low-SiO_2 Brown Pumice fall ■High-SiO_2 Brown Pumice fall ■Pink Pumice fall
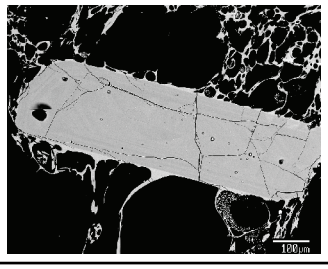	Generally normally zoned plagioclase, although reversely zoned varities occur and are common in Cobweb tuff cone deposits, with oscillating An contents ranging from An_{37}-An_{60}.	■Cobweb tuff cone ■Cobweb lava flow ■Brown Pumice agglutinate ■Low-SiO_2 Brown Pumice fall ■High-SiO_2 Brown Pumice fall ■Pink Pumice fall

Figure 19. Representative back-scattered electron images of plagioclase types based on texture and composition correlated with occurrence in different eruptive phases of the ~400 yr B.P. eruption. Filled boxes indicate the presence of specific plagioclase types in deposits emplaced during specific eruptive phases. Open boxes indicate that specific plagioclase types were not observed in deposits emplaced during those eruptive phases.

occur as either coarsely sieved or oscillatory zoned crystals. Cores of intact crystals record a slightly broader compositional range ($An_{40–60}$; figs. 19, 20) compared to earlier deposits. Similar to low-SiO_2 Brown Pumice samples, the An contents of cores of coarsely sieved plagioclase in agglutinate deposits are notably higher, ranging from An_{80} to An_{95}.

Cobweb lava flow samples are poorly vesicular and coarsely glomeroporphyritic (fig. 23). They resemble earlier erupted deposits in their mineral assemblage, occurrence of both individual and glomerocrystic crystals, and abundant oscillatory-zoned plagioclase with reversely zoned exteriors. Cobweb lava flow samples differ most significantly in thin section from Pink Pumice and Brown Pumice tephra in their lower vesicularity, higher crystallinity (5–25 percent), and abundance of disequilibria textures including widespread oscillatory-zoned, coarsely sieved, dusty-sieved plagioclase, embayed pyroxene, and crystals wrapped in reaction rims. Cobweb lava flow samples also contain plagioclase with very high-An ($An_{83–92}$) and high-FeO (0.7–0.8 wt%) cores (figs. 19, 20, 22), similar to the high-An coarsely sieved plagioclase in low-SiO_2 Brown Pumice pyroclasts. Also similar to coarsely sieved plagioclase in low-SiO_2 Brown Pumice, very high-An plagioclase crystals in Cobweb lava flow samples are enclosed by lower An and FeO wt% rims. However, the thickness of rims that enclose

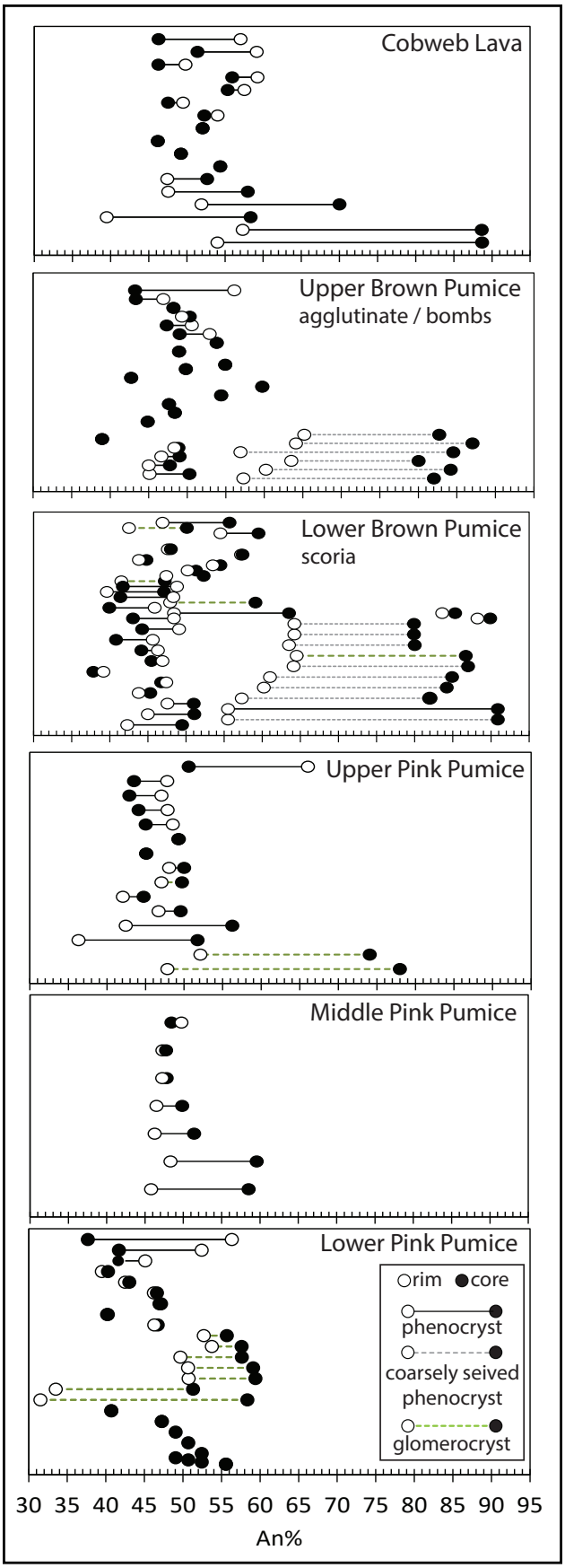

Figure 20. Rim and core anorthite compositions (An% = 100 x [Ca mol% / Ca mol% + Na mol% + K mol%]) of plagioclase crystals by electron microprobe analyses relative to ~400 yr B.P. stratigraphy. Filled circles denote compositions of crystal cores and open circles denote compositions of crystal rims. Horizontal lines connect rim and core compositions from the same crystal: black solid lines indicate analyses of individual phenocrysts, black dotted lines indicate analyses of coarsely sieved plagioclase, and green dashed lines indicate analyses of crystals within a glomerocryst. The vertical order of plagioclase analyses within each stratigraphic package is arbitrary. High-An coarsely sieved and glomerocrystic plagioclase in Brown Pumice scoria and agglutinate were plotted adjacent to other plagioclase to better utilize space. Most analyses of plagioclase in agglutinate samples are of fragments, indicated by single dots.

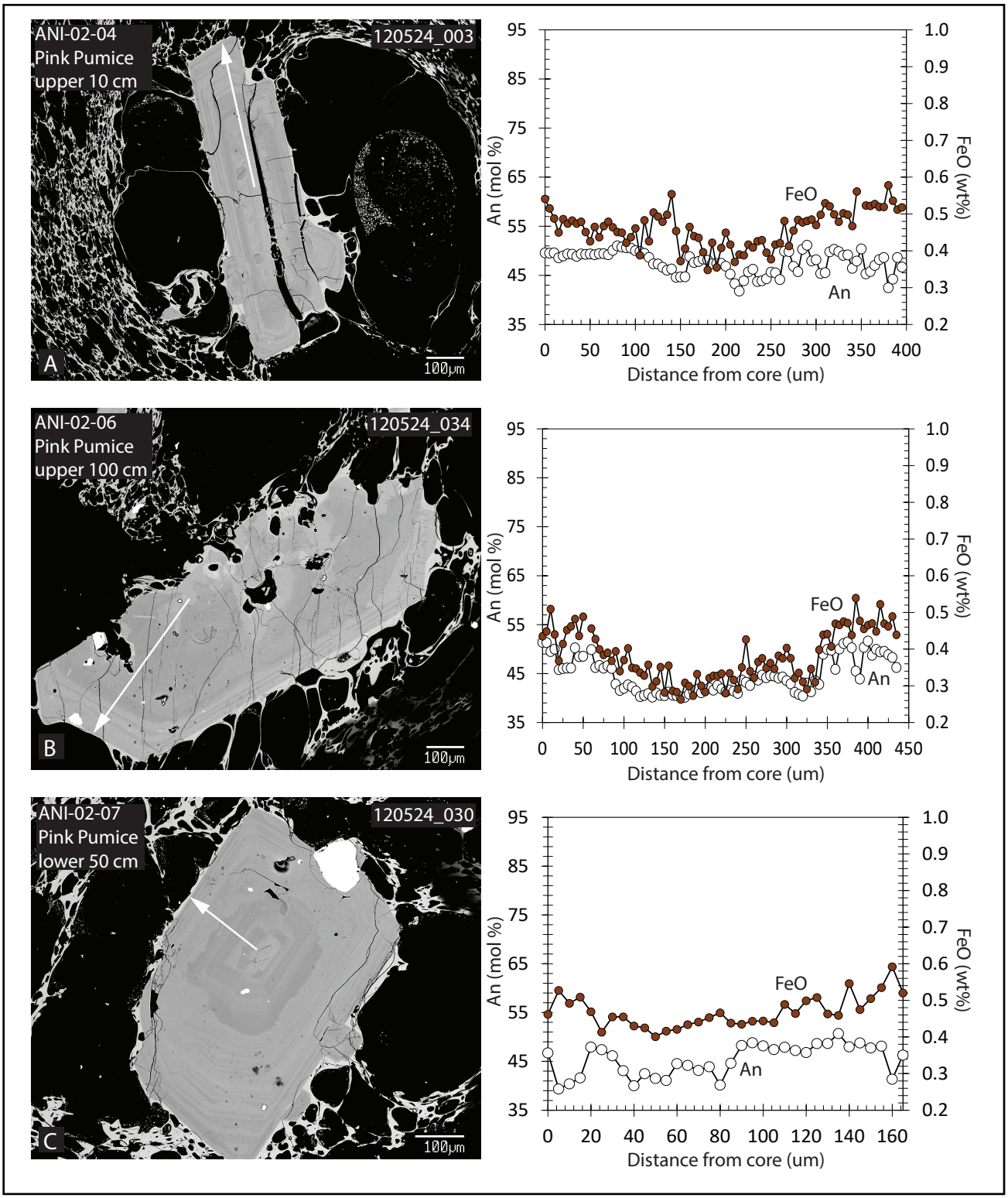

Figure 21. Core to rim composition transects (shown by arrow) of plagioclase with corresponding backscattered electron images of crystals from Pink Pumice pyroclasts—analyses by electron microprobe. Open circles correspond to An% vertical axis and filled circles correspond to FeO (wt%) vertical axis. Many plagioclase in Pink Pumice pyroclasts are characterized by oscillatory zoning (A and C). Other plagioclase are characterized by a normally zoned interior enclosed by a dissolution band enclosed by a reversely zoned exterior (B). Reversely zoned exteriors are marked by abrupt increases in both An% (An% = 100 x [Ca mol% / Ca mol% + Na mol% + K mol%]) and FeO wt%.

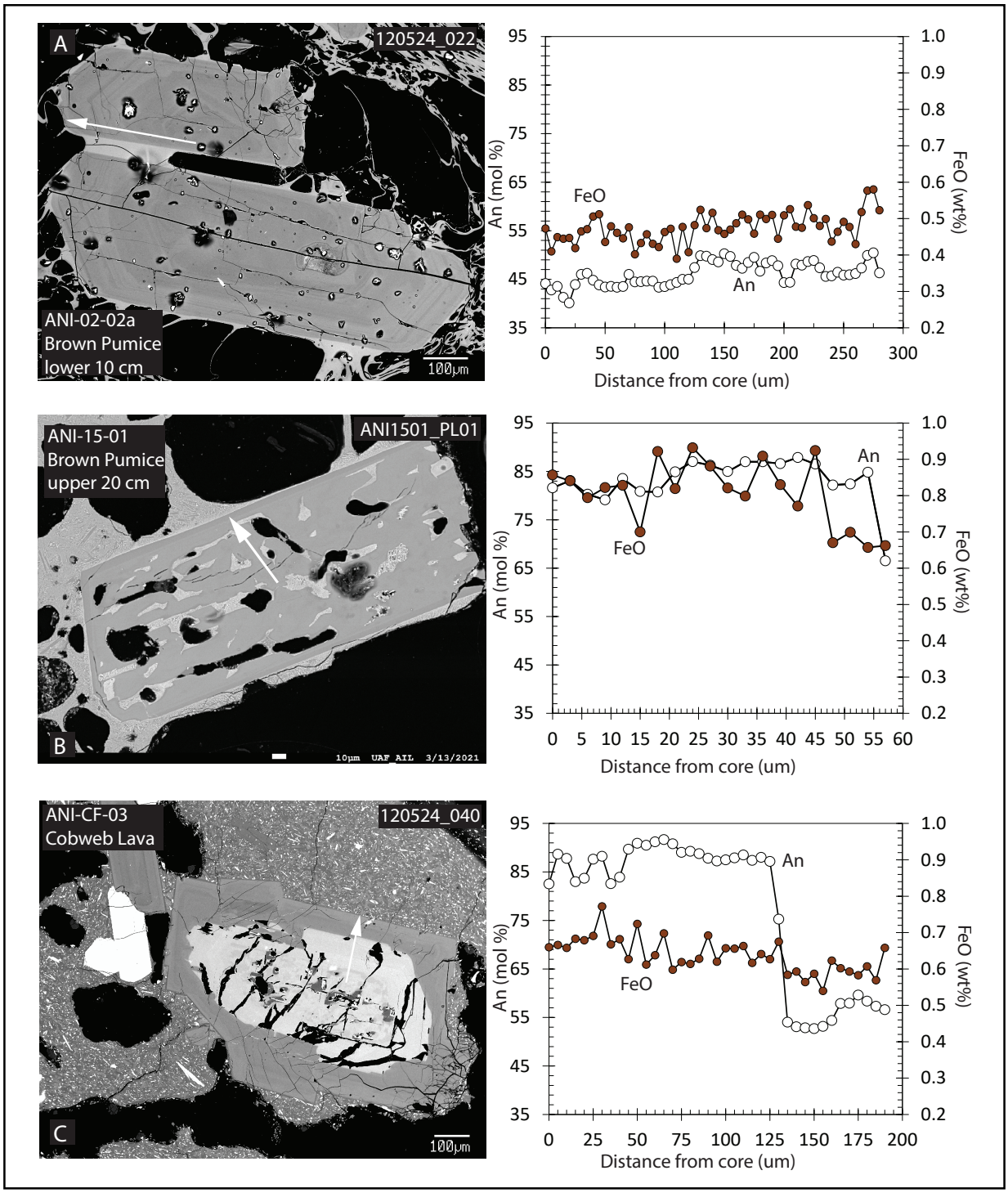

Figure 22. Core to rim transects (shown by arrow) of plagioclase via electron microprobe with corresponding backscattered electron images of crystals from Brown Pumice and Cobweb lava flow samples. Open circles correspond to An% vertical axis and filled circles correspond to FeO (wt%) vertical axis. **A.** Plagioclase in lower Brown Pumice fall (sample ANI-02-02a, location 2) showing oscillatory zoning in terms of fluctuating An% (An% = 100 x [Ca mol% / Ca mol% + Na mol% + K mol%]) and FeO wt% with distance toward the crystal rim. **B.** Coarsely sieved plagioclase in low-SiO_2 Brown Pumice is characterized by very high and relatively constant An% and FeO% interior surrounded by a thin rim with significantly lower An% and FeO% compositions, which is consistent with crystal nucleation and growth from a water-rich basalt at high pressures followed by ascent and crystallization from a more felsic and lower temperature melt (e.g., Nelson and Montana, 1992). **C.** Plagioclase crystal in the Cobweb lava flow (sample ANI-CF-03) with a rounded and fractured core region characterized by very high An% and FeO wt% enclosed by a euhedral rim with abruptly lower An%, which is consistent with crystal nucleation and growth from a basalt followed by crystallization from a more felsic and lower temperature melt.

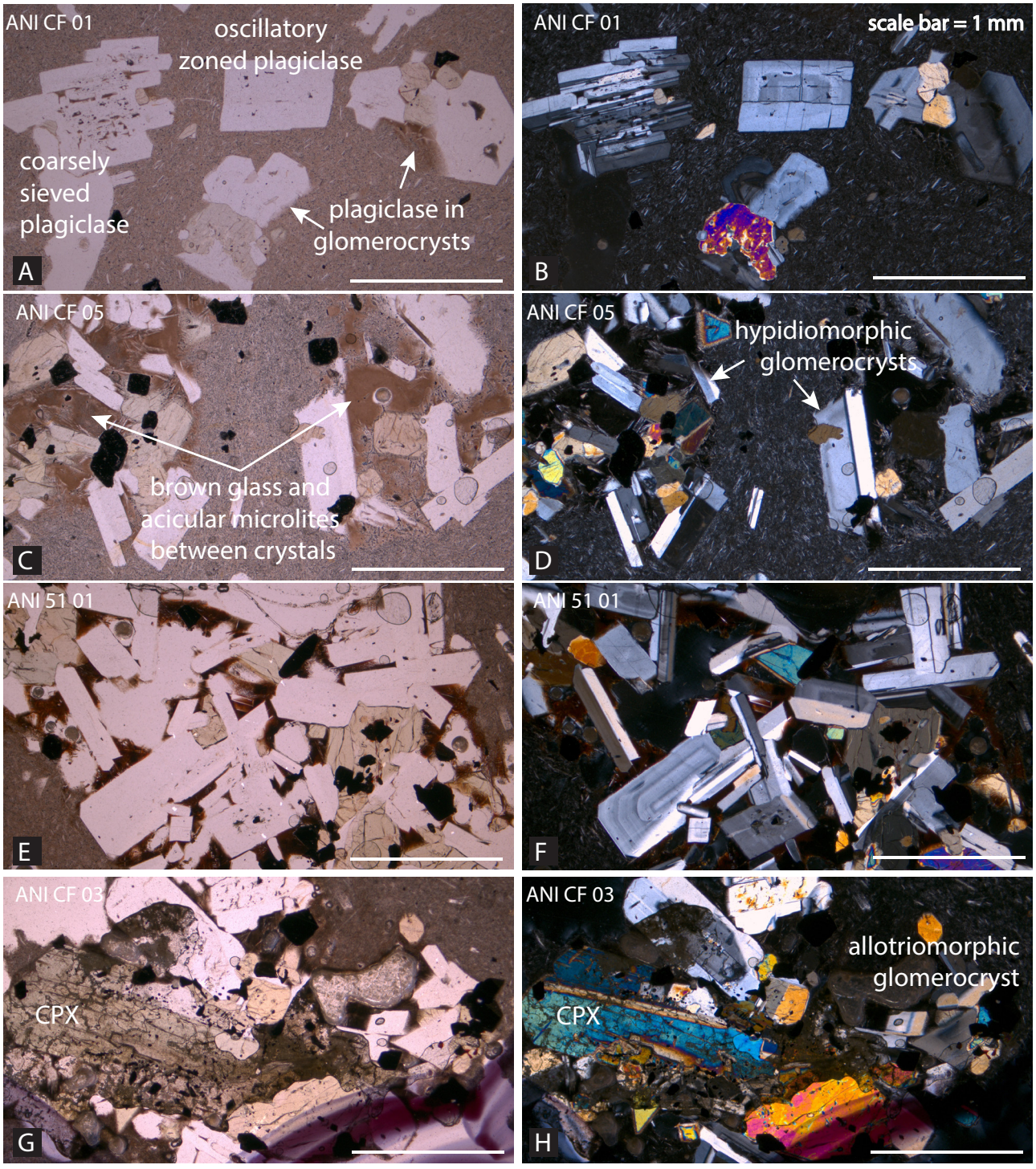

Figure 23. Photomicrographs of the Cobweb lava flow. Scale bar for all images is 1 mm. **A, B.** Sample ANI-CF-01. Plane-polarized (A) and cross-polarized (B) view showing different types and textures of plagioclase, including coarsely sieved plagioclase, oscillatory-zoned plagioclase, and plagioclase with CPX and OPX in hypidiomorphic granular glomerocrysts set in a trachytic groundmass. **C, D.** Sample ANI-CF-05. Plane-polarized (C) and cross-polarized (D) view of hypidiomorphic glomerocrysts consisting of plagioclase, CPX, OPX, apatite, and FeTi oxides. Glomerocrysts are suspended in a trachytic groundmass, but brown glass exists in the space between or adjacent to crystals in the glomerocrysts and needle-like microlites extend from crystal faces into the glass. **E, F.** Sample ANI-51-01. Plane-polarized (E) and cross-polarized (F) view of idiomorphic to hypidiomorphic granular glomerocrysts consisting of plagioclase, CPX, OPX, apatite, and FeTi oxides with brown glass and acicular microlites between crystals. **G, H.** Sample ANI-CF-03. Plane-polarized (G) and cross-polarized (H) view of allotriomorphic granular glomerocrysts where plagioclase and pyroxenes display embayed and curved faces along penetrating boundaries.

high-An plagioclase cores in the Cobweb lava flow are notably thicker than those enclosing high-An plagioclase cores in the low-SiO_2 Brown Pumice. The variety of glomerocryst textures, where some show idiomorphic granular texture and others show hypidiomorphic to allotriomorphic granular textures with intergrown plagioclase and pyroxene, is also unique to Cobweb lava flow samples compared to earlier emplaced tephra. The heterogeneous nature of the groundmass in Cobweb lava flow samples is also different—whereas individual crystals are suspended in a finely crystalline (and sometimes flow banded) trachytic groundmass, the groundmass surrounding glomerocrysts is usually brown glass (fig. 23). Many idiomorphic granular glomerocrysts also show intersertal texture with brown glass occupying interstices between plagioclase and pyroxene crystals. Compositional differences also occur between individual crystals and those in glomerocrysts. For example, core compositions of OPX crystals suspended in finely crystalline groundmass are compositionally distinct in terms of their lower Mg# (molar Mg/[Mg+Fe]) and greater variability of Al_2O_3 compared to OPX in glomerocrysts (app. E).

Glass Compositions

Major element compositions of matrix glass in Pink Pumice and Brown Pumice pyroclasts from locations 1, 2, 15, and 32 (figs. 7, 9, 11B, 25) are shown in appendix G and figure 24. For comparison, we include major element compositions of matrix glass in pre-400 yr B.P. pumice fragments from within a pyroclastic deposit exposed in the steep cliffs of the Half Cone edifice that underlies a thin soil layer and the Pink Pumice. Most low-SiO_2 Brown Pumice matrix glass compositions normalized to anhydrous values plot as basaltic-andesite and andesite, although some compositions plot within the dacite field. Pink Pumice and high-SiO_2 Brown Pumice matrix glass compositions normalized to anhydrous values plot across as dacite and trachydacite. No difference is observed between matrix glass compositions from the base to the top of the Pink Pumice. Matrix glass analyses in most Brown Pumice pyroclasts range from 56.9 to 69.9 percent SiO_2, although like the whole-rock compositions, most Brown Pumice matrix glass compositions plot in a bimodal distribution with relatively few intermediates. Interestingly, the most mafic Brown Pumice matrix glass compositions are slightly less evolved than the most mafic Brown Pumice whole-rock compositions in terms of wt% SiO_2, which might reflect accumulation of plagioclase and plagioclase-rich glomerocrysts. Microlite-rich matrix glass in agglutinate emplaced during the later Brown Pumice phase of the eruption range from 68.3 to 69.5 percent SiO_2. Pre-400 yr B.P. Half Cone tephra plots linearly with Pink Pumice and Brown Pumice matrix glass except for TiO_2. Bacon and others (2014) also observed higher TiO_2 concentrations in pre-400 yr B.P. Half Cone tephra compared to ~400 yr B.P. tephra. Pink Pumice matrix glasses also show a similarly narrow compositional range (68.3–69.8 percent SiO_2) compared to matrix glass of older Half Cone tephra (65.9–66.4 percent SiO_2).

Riehle and others (2000) used radiocarbon dating coupled with *in situ* glass analysis by electron microprobe of a tephra referred to both as Ash C (Nowak, 1968; Dumond, 1979) and Deposit C (Riehle and others, 2000) from the Brooks River Archeological District near Brooks Camp in Katmai National Park to suggest that the tephra originated from Aniakchak volcano. Riehle and others (2000) described Ash C at multiple locations within the Brooks River Archeological District, where it ranged from 5 to 10 cm thick and appeared as a fine ash layer with a pale yellow-gray base, a greenish gray center, and a grayish brown top overlain by a thin soil. Radiocarbon ages for Ash C indicated an age of ~400 yr B.P. (Riehle and others, 2000). Glass compositions of Ash C from Riehle and others (2000) are shown with glass compositions of known ~400 yr B.P. Half Cone tephra in figure 24. Also shown in figure 24 are glass compositions of Ash C samples that were collected by B. Browne and D. Dumond in 2004 and included in this study. Because the age and compositions of

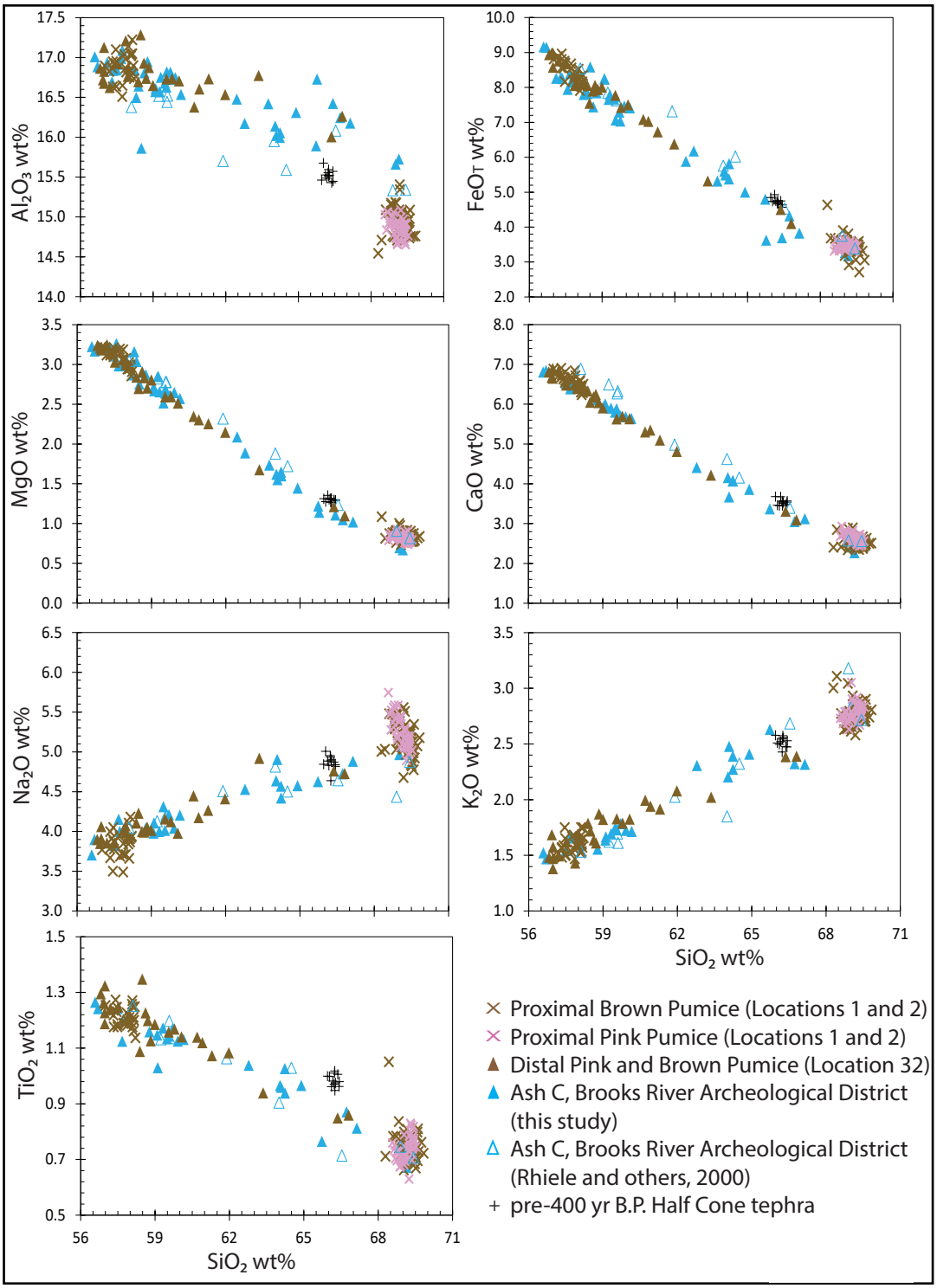

Figure 24. Anhydrous major element compositions of matrix glasses in pyroclasts from the Pink Pumice (pink X symbols) and Brown Pumice (brown X symbols) from proximal locations 1 and 2. Pink and Brown Pumice tephra from distal location 32 are also included (brown triangles). For reference, major element composition of matrix glasses in pyroclasts from pre-400 yr B.P. tephra from location 6 are included (black + symbol). Glass analyses are also included from ~400 yr B.P. Ash C samples from the Brooks River Archeological District ~230 km northeast of Half Cone published in Riehle and others (2000; open blue triangles) and collected by B. Browne and D. Dumond in 2004 (filled blue triangles). Ash C glass analyses support the hypothesis of Riehle and others (2000) that the Ash C tephra likely originated from Aniakchak volcano. We suggest that the Ash C tephra was deposited from the ~400 yr B.P. Half Cone eruption.

glass from known ~400 yr B.P. Half Cone tephra (this study) are equivalent to those of Ash C, we concur with Riehle and others (2000) that Ash C in Brooks Camp likely originated from the ~400 yr B.P. Half Cone cataclysmic eruption.

DISCUSSION

In this section, we utilize the tephra stratigraphy and geochemistry along with mineral and glass compositions to evaluate some important characteristics of the ~400 yr B.P. Half Cone eruption including (1) the volume of the ~400 yr B.P. eruption; (2) the magma storage temperatures based on titanomagnetite–ilmenite geothermometry calculations; (3) storage conditions of magmas erupted during the Pink Pumice and Brown Pumice phases—as well as the Cobweb lava flow—based on whole-rock geochemistry, magnetite-ilmenite thermobarometry, and mineral compositions and textures; and (4) a chronology of the ~400 yr B.P. eruption in light of the differences in whole-rock composition, mineral textures, grain size, accidental lithic concentration, sorting, and the nature (e.g., pumice versus lava) of resulting deposits.

Volume Calculations for the Half Cone Eruption

We use isopachs (fig. 11A, B) for the Pink Pumice and Brown Pumice fall deposits to estimate the volume of material erupted using the method of Nathenson and Fierstein (2015). This method graphically models the exponential decay in fall deposit thickness as a function of isopach area (Pyle, 1989; Fierstein and Nathenson, 1992; Nathenson and Fierstein, 2015). Results based on our measurements indicate a minimum bulk tephra volume of ~1.3 km^3 for the Pink Pumice fall (table 2). The volume of the Brown Pumice fall deposit is likely significantly greater than the Pink Pumice fall deposit but is more difficult to estimate due to concealment of the Brown Pumice deposits beneath thick ash-rich deposits in the central caldera and partial removal of Brown Pumice deposits by aeolian and pedogenetic processes in medial and distal locations. The similar age and equivalent glass compositions of Ash C in the Brooks River Archeological District (Riehle and others, 2000) to confirmed ~400 yr B.P. Half Cone tephra (this study) suggest a minimum volume of ~3.5 km^3 for the Brown Pumice fall and a dispersal that reached at least as far away as ~230 km northeast of Half Cone (fig. 25).

Isopleth mapping of the largest accidental lithic fragments (fig. 11C, D) in the Pink Pumice and Brown Pumice record differences in the dispersal of tephra between the two eruption phases. Lithic fragments deposited during the Pink Pumice phase were dispersed primarily to the north and northeast of Half Cone, whereas lithic fragments deposited during the Brown Pumice phase were dispersed to the northeast. Brown Pumice deposits also contain significantly larger lithic fragments compared to Pink Pumice deposits, indicating that Brown Pumice fall were deposited from a higher ash cloud than the cloud from which Pink Pumice fall deposits accumulated. The minimum magmatic volume (DRE) of the Pink Pumice fall is ~0.3 km^3 compared to ~1 km^3 for the Brown Pumice fall based on average lithic concentrations of 5 and 10 percent for the Pink Pumice and Brown Pumice, respectively, and average vesicularities of 75 and 65 percent for the Pink Pumice and Brown Pumice, respectively. Given the thickness of ~400 yr B.P. Half Cone tephra in Brooks Camp, it is likely that this deposit extends beyond the Alaska Peninsula. Indeed, recent field studies suggest that ~400 yr B.P. Half Cone tephra may occur throughout the Cook Inlet region as a stratigraphic layer that includes glass shards from both the Pink Pumice and Brown Pumice phases (K. Wallace, USGS, oral commun., 2021). We encourage future studies to further evaluate the extent of air fall tephra in southwest Alaska related to the ~400 yr B.P. Half Cone eruption.

The volume of tephra emplaced as thick and unconsolidated ash-rich pyroclastic density current (PDC) deposits within the caldera is difficult to calculate because of the unknown topography of the underlying surface at the time of emplacement,

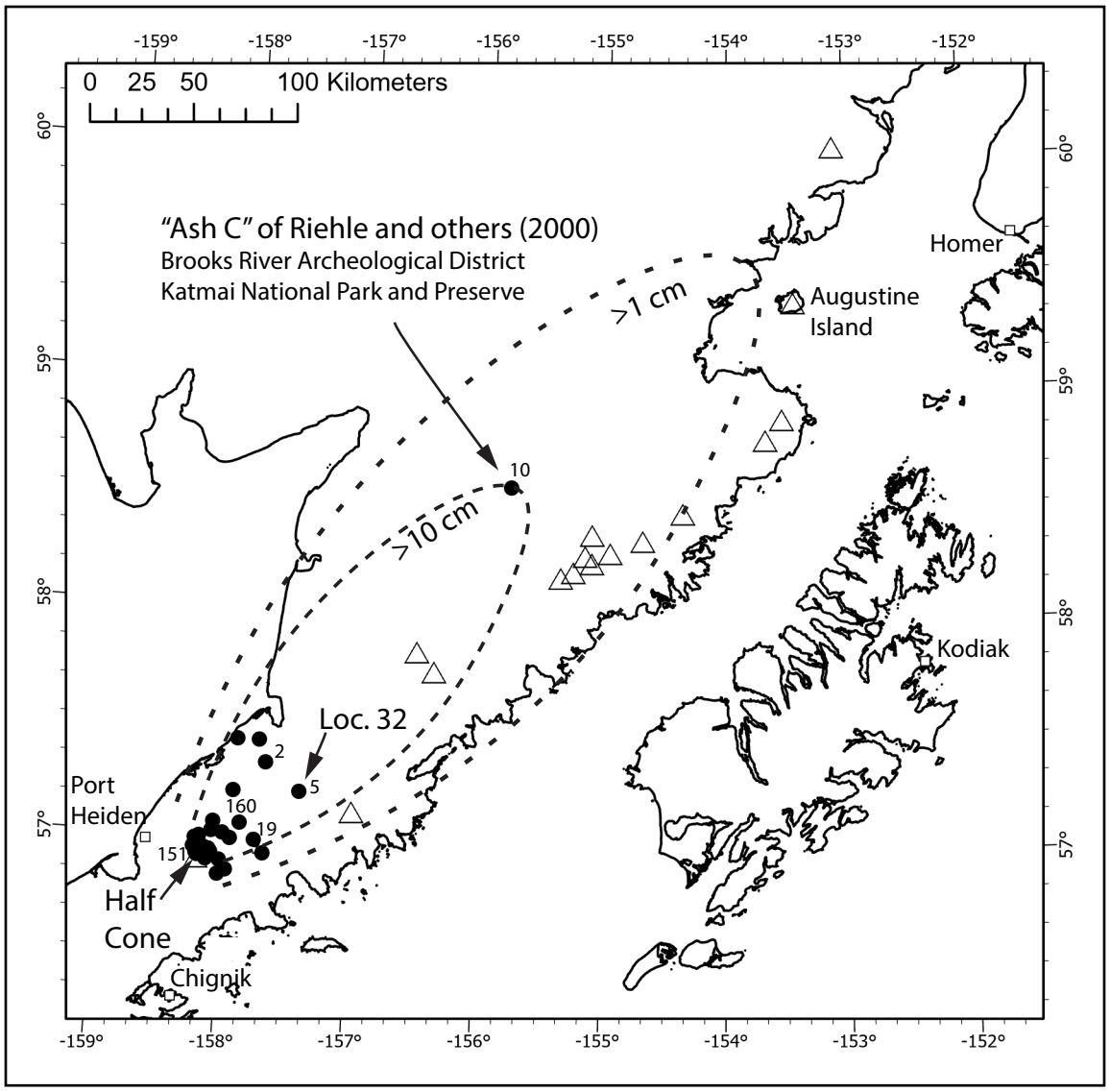

Figure 25. Approximate isopach contours (in cm) of the combined Pink Pumice and Brown Pumice fall layers drawn to include Ash C of Riehle and others (2000) in the Brooks River Archeological District within Katmai National Park and Preserve, located 230 km northeast of Half Cone. Numbers adjacent to sample locations (circles) specify measured thickness. Open triangles indicate Aleutian volcanoes. Open boxes indicate locations of communities, including Port Heiden, Chignik, Kodiak, and Homer. The 10 cm contour is of higher confidence than the 1 cm contour.

and because the base of these deposits is not exposed. Geologic mapping of the unconsolidated ash-rich deposits within Aniakchak caldera by Neal and others (2001; map unit Qht on fig. 2) indicates a surface area of approximately 20 km^2. In some locations, (e.g., along the north flank of Vent Mountain in the southern caldera, and atop Surprise Cone and lava flows from Vent Mountain near Surprise Lake) the unconsolidated ash-rich deposits are <1 m thick. In contrast, ash-rich PDC deposits within a 5 km^2 area in the central caldera are at least 40 m thick where exposed in gullies between the Cobweb lava flow and Surprise Cone. The 5 km^2 surface area, and an estimated minimum thickness in the center of the area of ~40 m that decreases to <1 m around the perimeter of ~400 yr B.P. PDC deposits based on geologic mapping (Neal and others, 2001), yield a minimum approximate tephra volume of ~0.5 km^3 if modeled after a trapezoidal prism. The magmatic volume (DRE)

Table 2. Volumes of tephra and magma produced during the ~400 yr B.P. Half Cone eruption phases.

Eruption Phase	Types of Deposits	Minimum Tephra Volume (km^3)	Minimum Magma Volume, Dense Rock Equivalent (km^3)
Pink Pumice fall	clast supported coarse pumice fall proximally, fine ash distally	~1.3	~0.3
Brown Pumice fall	clast supported coarse scoria fall proximally, fine ash distally	~3.5	~1
Brown Pumice PDC	caldera-filling unconsolidated and matrix supported lithic- and ash-rich pyroclastic density current deposits	~0.5	~0.1
Brown Pumice agglutinate	thick, indurated, and variably oxidized and welded agglutinate deposits	~0.05	~0.003
Cobweb lava flow	crystal-rich blocky lava flow	~0.1	~0.1

of these PDC deposits is ~0.1 km^3 based on an average lithic concentration of 50 percent and average vesicularity of 65 percent for the pyroclasts.

The volume of tephra emplaced as thick, indurated, and variably oxidized and welded agglutinate deposits within the Half Cone cliffs is also difficult to calculate because of the unknown topography of the underlying surface at the time of emplacement and subsequent burial of this layer by material erupted in 1931. We approximate a volume of 0.05 km^3 for these deposits based on a high concentration of accidental lithics and average thickness of 60 m along the 4 km of southeast-facing cliff face in the western walls of the Half Cone edifice. The estimated magmatic volume (DRE) of agglutinate deposits is 0.003 km^3 based on an average lithic concentration of 50 percent and average vesicularity of 10 percent.

We estimate that a volume of at least ~5.4 km^3 of bulk tephra (~1.4 km^3 DRE) and approximately 0.1 km^3 of lava erupted as the ~50-m-thick and ~2 km x ~1.6 km Cobweb lava flow, yielding a total magmatic volume (DRE) of ~1.5 km^3. These estimates update those from Neal and others (2001), who proposed a total tephra volume of between 0.75 and 1.0 km^3 (0.2–0.3 km^3 DRE). The volume of tephra produced during the ~400 yr B.P. Half Cone eruption is at least five times greater than the volume of tephra erupted in 1931 (Nicholson and others, 2011). The volume of this Half Cone eruption is second only to that of the 1912 Novarupta eruption–the 20th century's most voluminous volcanic eruption (13.5 km^3 DRE; Hildreth and Fierstein, 2012)—among Alaska Peninsula eruptions over the past ~3,400 years whose volume estimates are well constrained.

Titanomagnetite and Ilmenite Geothermometry

While titanomagnetite and ilmenite are present in all ~400 yr B.P. and pre-400 yr B.P. Half Cone deposits, ilmenite is less common than titanomagnetite in Pink Pumice samples and is rare in Brown Pumice samples. Core regions of 86 touching titanomagnetite and ilmenite phenocryst pairs in ≤3,400 yr B.P. deposits from Aniakchak volcano—including 28 pairs from the ~400 yr B.P. Half Cone eruption—were analyzed for major element concentrations via electron microprobe and used to estimate pre-eruption equilibrium temperatures. Titanomagnetite and ilmenite range from 20 to 100 μm in diameter and vary in crystal shape from euhedral to subhedral for titanomagnetite and subhedral to anhedral for ilmenite. Pyrite is often found in association with titanomagnetite in Brown Pumice samples, either as an inclusion or adjacent to titanomagnetite crystals.

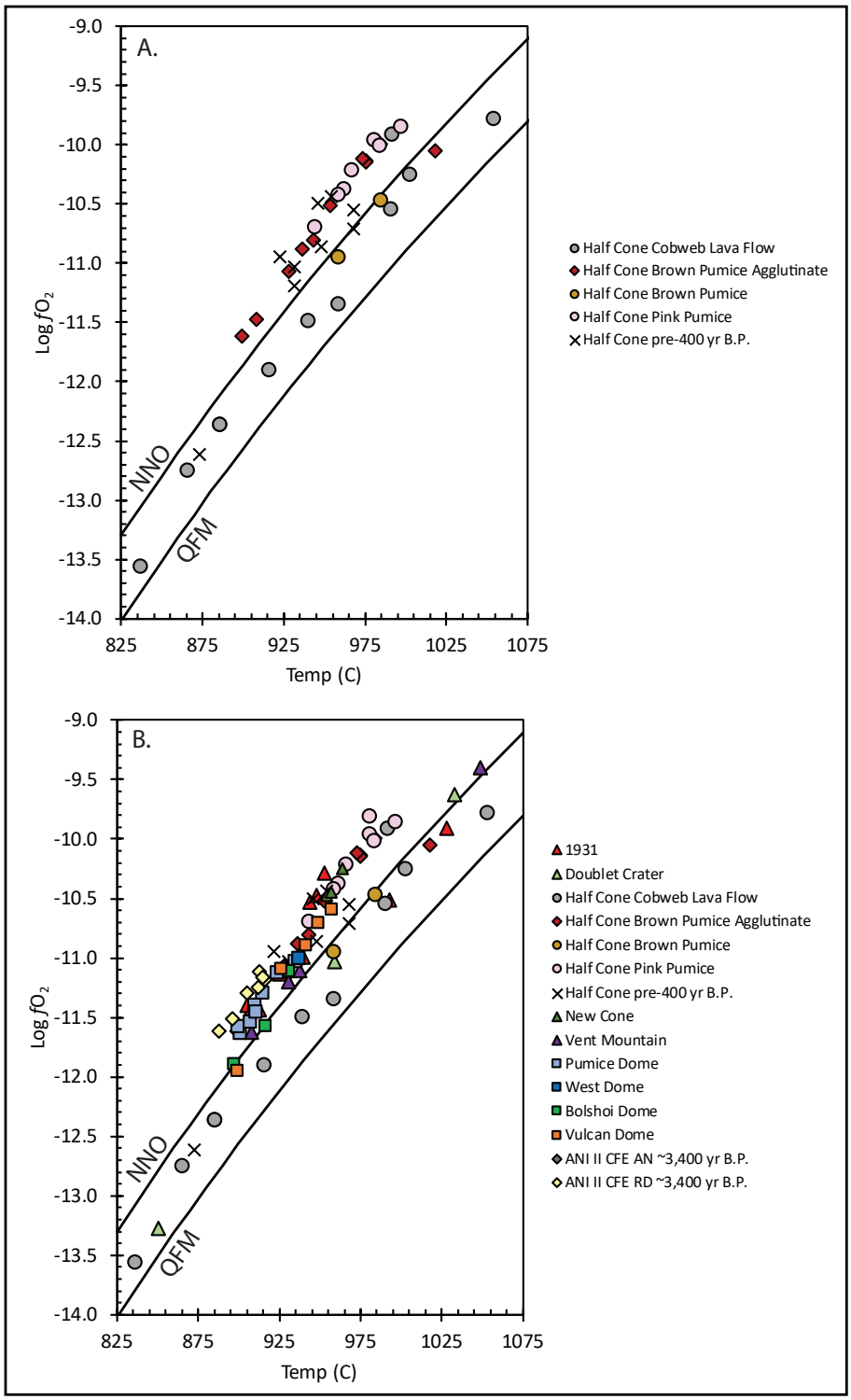

Figure 26. Calculated pre-eruptive equilibrium temperatures versus log fO_2 using the algorithm of Ghiorso and Evans (2008) via the OFM Research website for touching titanomagnetite–ilmenite pairs collected by electron microprobe. All titanomagnetite–ilmenite pairs passed the Mg/Mn partitioning test for equilibrium (Bacon and Hirschmann, 1988). Because the Ghiorso and Evans (2008) thermobarometer is based on a larger experimental dataset acquired over a greater range of fO_2 conditions, we prefer calculated temperatures and oxygen fugacities using their method to those calculated using ILMAT (app. F); see Coombs and others (2009) for additional comparison of calculation methods. Nickel-nickel-oxide (NNO) and quartz-fayalite-magnetite (QFM) buffer curves are shown. **A.** Temperatures and log fO_2 for ~400 yr B.P. deposits. **B.** Temperatures and log fO_2 for Aniakchak II (ANI II) caldera-forming eruption deposits and post-caldera products of Aniakchak volcano.

Many titanomagnetite and ilmenite in indurated and partially welded agglutinate deposits emplaced during the Brown Pumice phase as well as some in the Cobweb lava flow are oxidized and contain exsolution lamellae. These crystals were excluded from geothermometry calculations.

We calculated temperatures and corresponding fO_2 conditions for touching titanomagnetite-ilmenite pairs in Mg–Mn equilibrium (Bacon and Hirschmann, 1988) using two techniques. One technique utilizes the Ghiorso and Evans (2008) geothermobarometer. The other geothermobarometer is modeled in the ILMAT spreadsheet (Lepage, 2003) using the calculations of Anderson and Lindsley (1985) and Stormer (1983). Results from Ghiorso and Evans (2008) and ILMAT generally agree in terms of a range of fO_2, although ILMAT calculates slightly lower temperatures and fO_2 overall (app. F). Temperatures and corresponding fO_2 conditions of touching titanomagnetite-ilmenite pairs based on the Ghiorso and Evans (2008) geothermobarometer are shown in figure 26. Some scatter of these results is expected due to analytical effects and model uncertainty in terms of temperature and fO_2, which are likely ~50°C and ~0.3 Log_{10} units, respectively.

Pre-eruptive magmatic temperatures recorded by titanomagnetite-ilmenite pairs in Pink Pumice samples range from 944 to 997°C and form a linear array ~0.5 log units above the NNO buffer (fig. 26A). Titanomagnetite-ilmenite pairs in scoria from the Brown Pumice fall record similar temperatures (959–985 °C) but lower fO_2 conditions, which are slightly below the NNO buffer. Titanomagnetite-ilmenite pairs in Brown Pumice agglutinate record a wider range of pre-eruptive temperatures than either Pink Pumice or Brown Pumice samples (899–1018 °C). Most pairs plot in a fO_2 population that overlaps the Pink Pumice array. One pair from an agglutinate sample plots with the Brown Pumice array at lower fO_2. Fe–Ti oxide pairs from the Cobweb lava flow have the largest fO_2 range (NNO -0.5 to NNO +0.5), although most pairs overlap Brown Pumice samples at lower fO_2 conditions near NNO -0.5. Pairs in Cobweb lava flow samples record temperatures ranging from 837 to 1054°C, which is the largest temperature range and includes both the lowest and the highest temperatures recorded in deposits emplaced during any phase of the ~400 yr B.P. eruption. However, the Fe–Ti oxide pairs from Cobweb lava flow samples that yield the lowest temperatures are also those with the most euhedral forms, suggesting that they might be most representative of crystal-melt equilibrium (Bacon and others, 1997). It is possible that the temperature range recorded by Fe–Ti oxide pairs in Cobweb lava flow samples indicates disequilibrium, which is commonly observed in lava-hosted Fe–Ti oxides (e.g., Venezky and Rutherford, 1999; First and others, 2021).

Pre-400 yr B.P. Half Cone tephra and lavas contain titanomagnetite-ilmenite pairs that record temperatures between 873 and 968°C; which overlaps with cooler temperatures of Pink Pumice and Brown Pumice samples. Geothermometry results of titanomagnetite-ilmenite pairs in samples from the ~3,400 yr B.P. Aniakchak II rhyodacite and post-caldera deposits are shown in figure 26B. Most titanomagnetite-ilmenite pairs in ≤3,400 yr B.P. deposits record similar temperatures as the ~400 yr B.P. deposits (888–1049°C). In addition, Fe–Ti oxide pairs in ≤3,400 yr B.P. deposits record two main arrays of fO_2 conditions, one between the NNO buffer and ~0.5 log units above NNO and another array below the NNO buffer (fig. 26B). As observed in the geothermometry results of ~400 yr B.P. deposits, titanomagnetite-ilmenite pairs in ≤3,400 yr B.P. deposits that record lower fO_2 conditions also record a broader range of temperatures (851–1028 °C) compared to pairs that record higher fO_2 conditions.

Pre-Eruption Storage Conditions of the ~400 yr B.P. Half Cone Magmas

Previous studies have described the subvolcanic magma reservoir of Aniakchak volcano as a magma mush column composed of a range of magma compositions that evolve through a

combination of crystal-liquid fractionation, crustal assimilation, and periodic magma recharge (Nye and others, 1997; George and others, 2004; Dreher and others, 2005; Bacon and others, 2014). Such a magma mush probably existed ~400 yr B.P. at a depth of ~3 km below Half Cone based on pre-eruptive concentrations of H_2O and CO_2 melt inclusions in plagioclase from Pink Pumice pyroclasts (Bacon, 2000, 2002). Larsen (2006) proposed slightly greater pre-eruption storage depths (~3–5 km) for magmas emplaced during the 3,430 ^{14}C yr B.P. Aniakchak II caldera-forming eruption. The widespread occurrence of glomerocrysts with interstitial melt in the Pink Pumice and Brown Pumice (fig. 17,18), as well as the Cobweb lava flow (fig. 23), likely represent fragments of this interlocking crystal mush that were disconnected from the mush prior to eruption or during magma ascent and eruption. Textures and compositions of crystals contained in glomerocrysts, such as coarse-grained plagioclase with high-An% cores and lower-An% rims, record a gradual change in the melt composition over time toward a cooler, increasingly felsic residual melt as the reservoir solidified. Common white "felsite" accidental lithics in ~400 yr B.P. tephra—which contain 77.0 wt% SiO_2 and are dominated by quartz and plagioclase with minor mafic silicates, magnetite, ilmenite, and apatite—are also consistent with the presence of a highly crystallized mush column located at shallow depths beneath Half Cone (Bacon and others, 2014).

Different regions of this magma mush column—each the product of slightly different evolution—were tapped by Half Cone over its eruptive history (Bacon and others, 2014). Observations to support this interpretation include (1) some compatible and incompatible elements (e.g., Al_2O_3, MnO, P_2O_5, Sr, Ba, V; figs. 12, 13, 14) and element ratios (e.g., K_2O/P_2O_5; fig. 15) plot along displaced trends, where Pink Pumice and Brown Pumice samples, Cobweb lava flow samples, and Cobweb tuff cone samples plot in linear arrays that are parallel to, but offset from, each other; (2) Cobweb tuff cone samples more closely resemble pre-400 yr B.P. tephra and lava from Half Cone than Pink Pumice and Brown Pumice tephra or Cobweb lava flow; (3) some samples of the Cobweb lava flow have concentrations of elements like Al_2O_3 that plot beyond the compositional range of tephra from either the Pink Pumice or Brown Pumice; (4) scatter in variation diagrams of some major elements (e.g., Al_2O_3, P_2O_5; figs. 12, 13) and trace elements (e.g., Sc); and (5) the span of rare earth element (REE) patterns for Pink Pumice and Brown Pumice, Cobweb lava flow, and Cobweb tuff cone, as well as contrasting Eu anomalies of Brown Pumice agglutinate compared to other ~400 yr B.P. deposits (Bacon and others, 2014).

The dacite magma that erupted during the Pink Pumice phase likely tapped a relatively homogeneous region of the magma mush column based on the narrow range of whole-rock and plagioclase compositions as well as the scarcity of disequilibria mineral textures. However, whereas the high-SiO_2 Brown Pumice reflects the continued eruption of a darker colored Pink Pumice dacite based on similarities in mineral compositions and geochemical profiles, the low-SiO_2 Brown Pumice likely represents a mixture of newly arrived basalt with different pockets of resident dacite mush. A key observation to support a mixing origin is the presence of two plagioclase populations in the low-SiO_2 Brown Pumice and agglutinate. One plagioclase population, defined by ~An_{40}–An_{60} cores, matches those in the Pink Pumice (and high-SiO_2 Brown Pumice) and likely records crystallization in the resident dacite mush (fig. 20). The other plagioclase population is defined by high-An (An_{76}–An_{95}) and high-FeO cores that record crystallization in a basaltic magma. In addition, most high-An plagioclase in low-SiO_2 Brown Pumice and agglutinate display coarsely sieved texture, which is often attributed to nucleation and growth from a high-H_2O basaltic melt in the lower crust followed by ascent to the shallow crust (e.g., Nelson and Montana, 1992; Izbekov and others, 2002; Browne and others, 2006; Viccaro and others, 2010, 2016). The thin (<10 μm) rims with low FeO and An_{55}–An_{65} compositions that enclose calcic plagioclase in

low-SiO_2 Brown Pumice likely formed in response to mixing with with cooler and more felsic dacite magma (fig. 22B). The fact that several major and trace element concentrations in low-SiO_2 Brown Pumice pyroclasts are notably more scattered than those in Pink Pumice pyroclasts (e.g., Al_2O_3, Na_2O, V, Nb) may indicate that crystals from different regions of the magma mush column were incorporated into the mixture of basalt and resident mush during intrusion and withdrawal. Alternatively, it is possible that the low-SiO_2 Brown Pumice andesite may have been drawn-up from greater depths as the Pink Pumice dacite erupted. However, the presence of plagioclase with contrasting textures and core compositions but converging rim compositions within single thin sections suggests that magma mixing and crystal exchange played some role in the generation of the Brown Pumice magma, and possibly the initiation of the eruption. As the eruption continued, deeper and more hybridized mixtures of magma were tapped by the eruption, eventually producing intermediate compositions (e.g., those emplaced as the Cobweb lava flows) that show evidence of abundant mineral disequilibria including oscillatory-zoned, coarsely sieved, and dusty-sieved plagioclase; embayed pyroxenes; and crystals enclosed by reaction rims (Bacon and others, 2014).

Although no basaltic material (*sensu stricto*) was produced during the ~400 yr B.P. eruption, the presence of two plagioclase populations with contrasting compositions and textures in Brown Pumice phase deposits is consistent with the intrusion and mixing of a basalt into host dacite mush prior to, during, and possibly after the eruption. High-An plagioclase (~An_{80}–An_{95}) are also observed in pre-3,400 yr B.P. basalt lavas and 1931 basaltic andesite ballistics (Dreher, 2002; app. B). For this and other reasons, intrusions of basalt magma into the lower subvolcanic magma mush column prior to eruption is a process thought to have occurred throughout the eruption history of Aniakchak volcano (Nye and others, 1997; Dreher, 2002; George and others, 2004; Dreher and others, 2005; Bacon and others, 2014)

We hypothesize that the timescale over which intrusion and mixing associated with the ~400 yr B.P. Half Cone eruption occurred was likely short, possibly days or weeks, although quantitatively constraining the duration would require further *in situ* analysis of minerals coupled with diffusion modeling. Observations to support this hypothesis include (1) the bimodal distribution of Brown Pumice whole-rock compositions; (2) compositions of thin rims surrounding calcic plagioclase in low-SiO_2 Brown Pumice that approach–but generally do not overlap–rim compositions of plagioclase in the Pink Pumice (figs. 20, 22); (3) the wide range of Fe–Ti oxide equilibration temperatures in samples erupted during the Pink Pumice and Brown Pumice phases; and (4) eruption of mingled magma (i.e., banded pumice) was much more common than mixed magma (i.e., hybridized pumice) during the ~400 yr B.P eruption.

Eruption Chronology

We propose the following eruption chronology based on a synthesis of petrological and geochemical observations combined with the stratigraphy of the Pink Pumice and Brown Pumice and subsequently emplaced Cobweb lava flow and Cobweb tuff cone.

The ~400 yr B.P. eruption began as a result of overpressurization of a stagnant and volatile-rich magma mush column, which was likely the combined result of intrusion of mafic magma and crystallization. The intrusion of basaltic magma into the base of the reservoir, possibly over days or weeks prior to eruption, contributed both to the warming of the magma mush and to its overpressurization (e.g., Sparks and others, 1977; Huppert and others, 1982; Folch and Martí; 1998; Degruyter and others, 2017). Over a much longer timescale, prolonged crystallization of anhydrous minerals like plagioclase, OPX, CPX, and FeTi oxides in the dacite magma mush column would also raise the concentration of volatiles in the melt and lead to an increase in the pressure of the magma reservoir on the confining rock (e.g., Tait and others, 1989; Tramontano and

others, 2017). Although they operate on different timescales, intrusion of mafic magma and crystallization together lead to the propagation of a pathway for magma to ascend to the surface.

The fine-grained lithic- and ash-rich fall deposit at the base of the Pink Pumice is consistent with the eruption beginning with phreatomagmatic explosions caused by rising dacite magma encountering near-surface groundwater or ice and snow in a Half Cone vent (or both). This initial series of explosions effectively decompressed the shallow magma reservoir beneath Half Cone prompting further gas exsolution and vesiculation of the magma, which intensified the flux of fragmenting dacite magma exiting the vent. The rapidly expanding jet of gas, rock, and fragmenting magma entrained and warmed surrounding air, forming a buoyant Plinian eruption column that led to dispersal of the ~1.3 km^3 Pink Pumice and, due to the prevailing winds, its deposition of Pink Pumice ash shards at least 230 km from Half Cone to the northeast. Dramatic fluctuations in the diameters of pyroclasts and accidental lithics in the Pink Pumice indicate at least two cycles of waxing and waning mass flux at the Half Cone vent, which produced an eruption column that twice expanded and gained altitude before weakening to lower altitude. Using methods described in Carey and Sparks (1986), which utilize the dispersal and dimensions of the largest accidental lithic fragments in a pyroclastic fall deposit (fig. 11C) to estimate the height of an eruption cloud, the Pink Pumice eruption cloud would have had a maximum height of approximately 15–20 km (fig. 27).

The normally graded top of the Pink Pumice fall coincides with the second waning phase of the Pink Pumice. This portion of the stratigraphy is also marked by the first widespread (albeit in low concentration) occurrence of both brown-colored and compositionally banded pyroclasts, indicating that both dacite and an increasing amount of dacite-andesite mingled magmas were being tapped and erupted simultaneously from the subvolcanic magma mush column. The waning phase of the uppermost Pink Pumice does not, however, appear to have coincided with a pause in the eruption. The strongest evidence for a gradual transition rather than a break between the Pink Pumice phase and the Brown Pumice phase is the consistency of pyroclast and accidental lithic diameters across the Pink Pumice–Brown Pumice stratigraphic boundary. Although the top of the Pink Pumice and base of the Brown Pumice are more fine grained than much of the tephra deposit, indicating some waning in the mass flux of erupting magma, both are far coarser than the base of the Pink Pumice deposit, which reflects the onset of the ~400 yr B.P. eruption. Some studies cite stratigraphic or observational evidence for pauses in explosive eruptions, particularly those that coincide with compositional shifts in fall stratigraphies (e.g., Gardner and Tait, 2000; Andrews and others, 2007; Hildreth and

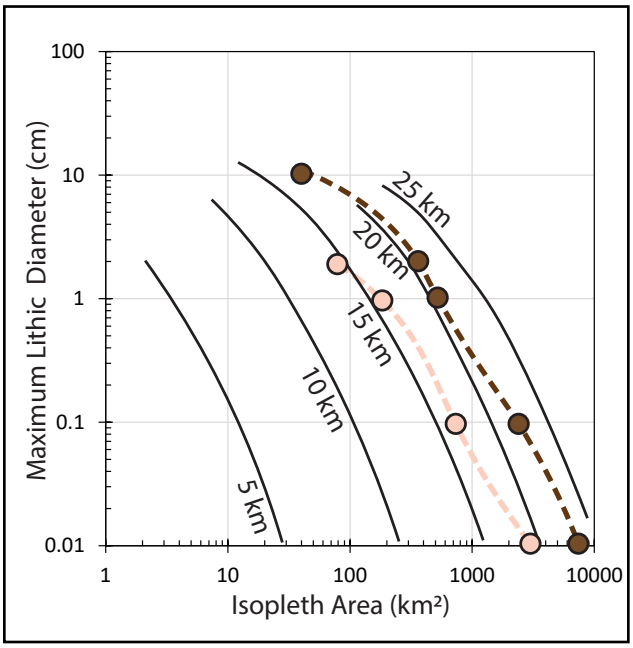

Figure 27. The area within isopleth contours (km^2) versus average of maximum lithic diameters from tephra samples for eruption column heights between 5 and 25 km (solid lines and adjacent labels) based on the fallout and dispersal model of Carey and Sparks (1986). Pink circles indicate lithic isopleth areas for maximum average lithics in the Pink Pumice fall deposit, consistent with an eruption column height of 15–20 km for the Pink Pumice phase of the eruption. Brown circles are lithic isopleths for maximum average lithics in the Brown Pumice fall deposit, consistent with an eruption column height of 20–24 km for the Brown Pumice phase of the eruption.

Fierstein, 2012). However, the stratigraphic record in this case is more consistent with continuation of the eruption, albeit at a reduced intensity, between the Pink Pumice and Brown Pumice phases.

The start of the Brown Pumice phase is marked by the accumulation of both high-SiO_2 and low-SiO_2 brown andesite scoria and a high concentration of accidental lithics and banded pumice, signaling a shift to the eruption of both darker-colored dacite magma (i.e., high-SiO_2 Brown Pumice) and more mafic andesite magma (i.e., low-SiO_2 Brown Pumice) as well as widening of the Half Cone vent. The beginning of the Brown Pumice phase (and end of the Pink Pumice phase) is also marked by an abundance of compositionally banded pumice, further indicating that at least two magma compositions were in molten contact during ascent, fragmentation, and solidification. The reversely graded Brown Pumice fall deposit, corresponds to an intensifying mass flux that initially produced an escalating Plinian column and dispersed Brown Pumice fall to the northeast, blanketing the northern Alaska Peninsula at least as far as 230 km to the northeast and likely beyond. The largest accidental lithic fragments in the Brown Pumice are typically larger in diameter than those in the underlying Pink Pumice (fig. 11D). Their distribution is consistent with a maximum ash cloud height of approximately 20–24 km based on the methodology of Carey and Sparks (1986; fig. 27)—significantly greater than the ash cloud associated with the Pink Pumice.

Over time, the eruption that fed the Brown Pumice eruption column destabilized. One indication of this destabilization is that clast-supported scoria fall deposits in proximal Brown Pumice become increasingly interrupted by cross-bedded ash-rich deposits. It is unlikely that these ash-rich deposits record pauses in the eruption because the diameters of pyroclasts and accidental lithics in the clast-supported scoria immediately above and below the ash deposits show either no change in grading or reverse grading marked by large bread-crust bombs. Instead, the interbedded ash-rich deposits record a destabilizing eruption column that deposited the Brown Pumice. Partial collapse at the margins of an otherwise buoyant eruption column produced short lived, fast moving, ground-hugging pyroclastic density currents that deposited ash-rich beds simultaneously with continued deposition of clast-supported scoria deposits from buoyant regions of an overhead Plinian column.

Except for the northwest caldera rim just above Half Cone, most of these high-energy density currents were confined within the caldera, reaching cumulative thicknesses of at least 40 m in the gullied pyroclastic plain between Vent Mountain and Half Cone. These pyroclastic density current deposits display high-angle cross bedding and are well exposed on the surface of the Vent Mountain lava flow south and southwest of Bolshoi Dome. Sandy surge deposits are also well exposed in gullies above the eastern shore of Surprise Lake. Fossil fumarolic mounds capped by indurated, wind-sculpted, sintered pyroclastic debris are especially abundant in the ash-rich deposits east and southeast of Half Cone. At least one fossil fumarole pipe is exposed in the headwall of the sapping channel that marks the origin of the main drainage into Surprise Lake from the basin northwest of the lake. Based on the preferential distribution of fumarolic features to the southeast and east of Half Cone, Neal and others (2001) inferred that this portion of the caldera was likely wet at the time of the eruption.

The repeated collapse of portions of the Brown Pumice Plinian column over time likely resulted from a combination of factors. One contributing factor was the continued erosion and widening of the Half Cone conduit and vent, and possibly the initiation of new vents, as recorded by high concentrations of accidental lithics in the Brown Pumice. Although we do not observe strong shifts in the proportion of accidental lithic material in the Brown Pumice fall deposit immediately above and below pyroclastic density current deposits–horizons marking partial collapse events–the base of the Brown Pumice contains up to 50 percent lithics in some locations, and the overall concentration of accidental lithics

in the Brown Pumice fall is five to 10 times higher than that observed for the Pink Pumice. In addition, proximal deposits contain >1 m angular blocks of dense lithic material near the Pink-Brown Pumice transition (fig. 6). Another contributing factor may have been the shift to eruption of higher density and more crystal-rich andesite magma compared to the highly vesicular and crystal-poor Pink Pumice dacite. The combination of denser andesite and the widening Half Cone conduit and vent would have effectively destabilized the Brown Pumice eruption column by isolating a greater proportion of hot pyroclasts from the atmosphere and cooling the erupting mixture by increasing the amount of cold accidental lithic material.

Eruptions characterized by collapsing eruption columns typically transition to violent fountains that discharge voluminous quantities of molten lava, gas, and hot rock around the vent (e.g., Sparks and others, 1978; Walker, 1985; Druitt and Bacon, 1986; Browne and Gardner, 2004; Andrews and others, 2007; Suzuki and Koyaguchi, 2012). The uppermost Brown Pumice exposed on the severed flanks of Half Cone and within ~2 km of Half Cone contains variably welded agglutinate and spatter deposits alternating with lithic-rich and nonwelded pumiceous deposits. These welded deposits likely mark a shift in eruption of a Plinian eruption column during the Pink Pumice and early Brown Pumice phases to a Strombolian or Hawaiian-style eruption of andesite magma by the end of the Brown Pumice phase. Thick packages of agglutinate formed through a combination of an extremely high accumulation rate, the molten state of andesite pyroclasts, and the thickness of amassed material. Together, these factors led to a high degree of heat retention in the resulting deposits, allowing for the plastic deformation and partial welding of Brown Pumice pyroclasts as well as their multicolored oxidation to crimson, orange, and yellow. Interestingly, the thickness of the agglutinate is relatively constant across the 1.5-km-long Half Cone edifice, which would be unusual if it had originated through eruptions from a single centralized vent, as agglutinate deposits tend to thin rapidly with distance from the vent due to the high density of the molten blobs (Sumner and others, 2005; Valentine and Connor, 2015). It is possible that the uniformity of the agglutinate thickness also signifies a change in the vent conditions to an aligned array of vents or an elongate fissure, both of which are consistent with Strombolian and Hawaiian eruption styles (Valentine and Connor, 2015). The presence of nonwelded lithic-rich tephra interbedded with the partially welded agglutinate packages also suggests a Strombolian to Hawaiian eruption style punctuated by dynamic changes in eruption intensity.

We do not know what Half Cone looked like prior to the ~400 yr B.P. eruption, but with remnant features in the wall of Half Cone as a guide, we surmise that Half Cone formed a significant topographic high composed of several thick dacite lava flows and domes flanked by an apron of tephra. Andesite and dacite vitrophyre exposed in the Half Cone walls show subhorizontal and subvertical columns, respectively, suggesting that the Half Cone flanks may have been wet or partially covered by snow and ice at the time they effused (Bacon and others, 2014). Prior to collapse, Half Cone was probably about 2–2.5 km across at its base and extended ~400 m up the northwest wall of the caldera. It may have had a small crater at the top with rims of coarse pyroclastic material—or the summit may have been a positive feature composed of a lava dome. We estimate a pre-400 yr B.P. Half Cone volume of ~0.5–0.6 km^3, notably smaller than modern Vent Mountain (~0.8 km^3). By the end of the Brown Pumice phase, we know that the majority of the Half Cone edifice had been destroyed and the Cobweb lava flow filled the basin left behind. What happened to Half Cone? Two commonly observed deposits linked to the destructive collapse of volcano edifices are voluminous debris avalanches (e.g., Crandall and others, 1984; Glicken, 1996) and lithic breccias associated with pyroclastic density currents (e.g., Walker, 1985; Druitt and Bacon, 1986; Browne and Gardner, 2004; Simmons and others, 2016). Deposits consistent with a debris avalanche have not been recognized at Half Cone; however, the

high abundance of poorly sorted, dense, and angular lithics in the upper ~30 m of the cliff-forming agglutinate on the rim of Half Cone resembles chaotic breccias associated with volcanic edifice failures that have been described elsewhere (see references above). The volume of lithics in cliff-forming agglutinate deposits is estimated to be ~0.03 km^3—too small to account for the missing volume of Half Cone. What if the Half Cone edifice was removed progressively during the Brown Pumice phase of the eruption? The total volume of accidental lithics in deposits erupted during the Brown Pumice phase is ~0.4 km^3—more in line with Half Cone's missing volume if ~70–80 percent of the pre-400 yr B.P. Half Cone edifice was removed during the eruption. Further work is necessary to investigate how the Half Cone edifice was destroyed during the ~400 yr B.P. eruption.

Sometime after the emplacement of coarse, lithic-rich fall deposits, which probably coincides with the collapse of Half Cone, a small explosion crater formed within the thick pyroclastic density current deposits about halfway between Vent Mountain and Half Cone. The crater is ~330 m across and has been mostly filled by 1931 tephra. It is breached downslope to the northeast and incised on the south by a steep-walled gulley that drains from the north flank of Vent Mountain. A 1–2-m-thick deposit of coarse, lithic-rich debris caps the rim and overlies 10s of centimeters of laminated, undulatory, oxidized, fine, and coarse ash. A pink-colored silt and sand is also distributed widely over the Half Cone pyroclastic plain in the vicinity of this explosion crater. Neal and others (2001) interpreted this feature and adjacent deposits as a secondary, phreatic explosion pit that partially filled with rain and snow following the ~400 yr B.P. eruption. Over time, the small crater walls breached, leading to the deposition of the boulder-rich alluvial fan to the northeast. Similar secondary explosion craters within the Half Cone pyroclastic density current deposits occur on the southwest rim of Surprise cone (Neal and others, 2001).

The effusion of the ~0.2 km^3 crystal-rich Cobweb lava flow followed by formation of the small Cobweb tuff cone represent the final activity in the Half Cone eruption. Mineral compositions and textural disequilibria of the Cobweb lava flow suggest that it is a mixture of Pink Pumice and Brown Pumice magmas, basaltic magma, and residual pre-400 yr B.P. Half Cone magmas. The Cobweb lava flow and Cobweb tuff cone may not have immediately followed the Brown Pumice phase and collapse of Half Cone, however, based on two main observations. First, the rims enclosing high-An plagioclase cores in the Cobweb lava flow are notably thicker than those observed in low-SiO_2 Brown Pumice (fig. 22), suggesting a longer period of crystal growth following a mafic magma recharge event. Second, several major and trace element concentrations in samples of Cobweb lava flow and Cobweb tuff cone pyroclasts trend separately from Pink Pumice and Brown Pumice samples, suggesting slightly different differentiation histories. When the Cobweb lava flow finally did erupt, it was emplaced as a series of radiating lobes that extend ~1.2 km east and ~0.8 km west from a central vent located slightly west of the center of the lava field. Although flow lobes do not touch the walls, lava essentially filled the collapse basin created by the explosive destruction of Half Cone. Each successive flow lobe must have advanced until progress was slowed by cooling and collision with the topographic rim of the basin edge, prompting a lateral "step" in effusion direction at the vent. Phreatomagmatic explosions of steam, rock, ash, and andesite pyroclasts–many with mingled swirls of residual Half Cone dacite–produced the 190-m-wide and 40-m-tall unconsolidated tuff cone atop the Cobweb lava flow. These small explosions may have been initiated by an accumulation of meltwater as precipitation fell on the Cobweb lava vent. Like the Cobweb lava flow, andesite pyroclasts in the Cobweb tuff cone have a complex mixing history that likely involves a higher proportion of basalt and pre-400 yr B.P. Half Cone magmas. In any case, the Cobweb tuff cone marks the end of the ~400 yr B.P. eruption. No evidence has been found that supports other eruptions from Aniakchak

volcano until the 1931 eruption, which blanketed the western flanks of Half Cone and the surface of the Cobweb lava flow and Cobweb tuff cone as well as the northern Alaska Peninsula (Hubbert, 1932a, 1932b; Neal and others, 2001; Nicholson and other, 2011). Aniakchak volcano continues to show episodic signs of unrest, suggesting that variably explosive eruptions will occur in the future (Bacon and others, 2014).

SUMMARY

Aniakchak volcano is a historically active caldera located ~670 km southwest of Anchorage on the central Alaska Peninsula between Veniaminof volcano to the south and Chiginagak volcano to the north. Port Heiden, located 25 km west where the Meshik River enters the Bering Sea, and Chignik, located 60 km southwest within Chignik Bay along the Pacific coast, are the nearest inhabited areas to Aniakchak volcano. The oldest known eruptions of Aniakchak volcano occurred approximately 850,000 years ago (Nye and others, 1997). Several Holocene eruptions, including two large caldera-forming eruptions—one between ca. 9,500 and 7,000 years ago (Bacon and others, 2014) and the other 3,400 ^{14}C yr B.P. (Miller and Smith, 1987)—have occurred from Aniakchak volcano, the latter of which is recorded by the current ~10-km-diameter and 0.5–1.0-km-deep caldera (Smith, 1925). Since the 3,400-yr B.P. eruption, at least a dozen separate vents within the Aniakchak caldera have erupted, including the most recent in 1931, which erupted from the vents on the southern caldera floor, lasted over eight weeks, and dispersed ash to distances of more than 600 km (Nicholson and others, 2011).

The largest post-caldera eruption yet identified from Aniakchak volcano occurred ~400 yr B.P. from Half Cone, an intracaldera composite cone on the northwest floor of the Aniakchak caldera that was largely destroyed by the eruption. This eruption produced two pumice fall deposits known as the Pink Pumice and Brown Pumice that were widely dispersed to the northeast on the Alaska Peninsula and possibly as far as southcentral Alaska. The Pink Pumice and overlying Brown Pumice deposits occur as two fall deposits and are easily distinguished within ~80 km of Half Cone. At distances greater than ~80 km from Half Cone, however, the Pink Pumice and Brown Pumice occur as one stratigraphic layer. Following small phreatomagmatic explosions, a buoyant Plinian eruption column that reached an altitude of 15–20 km combined with southwesterly winds to disperse ~1.3 km^3 of beige to pink dacite pumice fall (Pink Pumice) to the northeast of Half Cone. Over time, the appearance and composition of magma being erupted from Half Cone changed to a darker brown andesite scoria (Brown Pumice). The Brown Pumice fall deposit records an escalating Plinian column that reached altitudes of ~20–24 km and emplaced at least ~3.5 km^3 of scoria fall deposits at least as far away as 230 km to the northeast. Over time, the Brown Pumice eruption column partially collapsed, producing thick pyroclastic density current deposits, most of which were confined to within the caldera. Lithic-rich agglutinate and spatter exposed in 60-m-thick deposits atop the severed flanks of Half Cone and within ~2 km of Half Cone was emplaced at the end of the Brown Pumice phase. Most of the Half Cone edifice was destroyed by the end of the Brown Pumice phase followed by effusion of the ~0.1 km^3 crystal-rich dacitic Cobweb lava flow, which filled the basin formed by the destruction of Half Cone with a series of radiating lobes. The formation of a small andesitic tuff cone over the Cobweb lava flow vent represents the last known eruption of Half Cone. In all, we estimate that at least ~5.4 km^3 of tephra and ~0.1 km^3 of lava erupted during the ~400 yr B.P. eruption, yielding a total magmatic volume (DRE) of ~1.5 km^3.

Previous studies have described the subvolcanic magma reservoir of Aniakchak volcano as a magma mush column composed of a range of magma compositions that evolved through a combination of crystal-liquid fractionation, crustal assimilation, and periodic magma recharge (Nye and others, 1997; Dreher and others, 2005; Bacon and others,

2014). Such a magma mush probably existed ~400 yr B.P. at a depth of ~3 km below Half Cone based on pre-eruptive concentrations of H_2O and CO_2 in melt inclusions in plagioclase from Pink Pumice pyroclasts (Bacon, 2000, 2002). Different regions of this magma mush column—each the product of slightly different evolution—were likely tapped over the eruption history of Half Cone.

Pre-eruptive magmatic temperatures recorded by titanomagnetite-ilmenite pairs in Pink Pumice and Brown Pumice samples record similar temperature ranges (944–997°C and 959–985°C, respectively) but different fO_2 conditions, whereas Pink Pumice pairs plot between the NNO buffer and NNO +0.5, Brown Pumice pairs plot below the NNO buffer. Titanomagnetite-ilmenite pairs in Brown Pumice agglutinate record a wider range of temperatures than either Pink Pumice or Brown Pumice samples (899–1018°C) but include two populations of fO_2—one that overlaps the Pink Pumice array at higher fO_2 and one that overlaps the Brown Pumice array at lower fO_2. Titanomagnetite-ilmenite pairs from the Cobweb lava flow have the largest fO_2 range (NNO -0.5 to NNO +0.5) although most pairs overlap Brown Pumice samples at lower fO_2 conditions near NNO -0.5. Pairs in Cobweb lava flow samples record temperatures from 837°C to 1054°C, which is the largest temperature range and includes both the lowest and the highest temperatures recorded in deposits emplaced during any phase of the ~400 yr B.P. eruption. Geothermometry results of titanomagnetite-ilmenite pairs in samples of magmas erupted ≤3,400 yr B.P. from Aniakchak volcano record a similar temperature range and the presence of two fO_2 arrays as observed in ~400 yr B.P. samples, implying the existence of two regions of the mush column—each the product of slightly different evolution.

The ~400 yr B.P. eruption was likely initiated, at least in part, by the intrusion of a more mafic magma into the lower subvolcanic magma mush column prior to and during eruption. One line of evidence for this is textures and compositions of plagioclase crystals that record a change in the surrounding melt composition from a cooler felsic melt to a warmer mafic melt prior to the eruption. Another line of evidence is the occurrence of a unique population of high-anorthite plagioclase crystals in deposits emplaced during the Brown Pumice phase. Textures and compositions of these plagioclase are consistent with a crystallization history involving nucleation and growth of plagioclase in a basaltic magma at high pressures and high H_2O content in the lower crust followed by ascent of that basaltic magma to the shallow crust where it intruded into a more felsic magma. As the eruption continued, deeper and more hybridized mixtures of magma were tapped, eventually producing intermediate mixtures like the Cobweb lava flow. Aniakchak volcano continues to show episodic signs of unrest, suggesting that eruptions will occur in the future.

ACKNOWLEDGMENTS

The region we investigated for this study is the original homeland of the Alutiiq/Sugpiaq people who have inhabited the coastal environments of southcentral Alaska for over 7,000 years (Ringsmuth, 2007). We acknowledge the complex history and rich culture of the Alutiiq/Sugpiaq people and honor the families and tribal members still connected to this land. In particular, we are grateful to the people of Port Heiden for their generosity in sharing their insights and memories of Aniakchak volcano and for allowing us to base our field campaigns in their community.

Fieldwork was supported by the Alaska Volcano Observatory, the U.S. Geological Survey, and the University of Alaska Fairbanks Department of Geosciences and Geophysical Institute. This work was also partially supported by the U.S. Geological Survey under Cooperative Agreement No. G19AC00171. We especially thank Game McGimsey and Tom Miller for sharing their knowledge of Aniakchak volcano's geology, and pilots Howard Reed (Maritime Helicopters, Homer,

Alaska) and Sam Egli (Egli Air Haul, King Salmon, Alaska) for safe transport during field work. We also appreciate assistance from Game McGimsey, Rob Nicholson, James Gardner, and Tom Miller during field campaigns. We thank several colleagues for their scientific discussions, analytical assistance, and assistance with sample preparation, including Pavel Izbekov, Ken Severin, Frank Kyte, Kristi Wallace, Fiona Eberhardt, Manny Nathenson, Jessica Larsen, Chris Nye, Cheryl Cameron, Kate Bull, and Matthew Loewen. Brandon Browne also thanks Patricia Ekberg, John Perreault, Kristen Janssen, Simone Montayne, and Dennis Hojna. Thoughtful and constructive reviews by Tim Orr (USGS/Alaska Volcano Observatory), Nathan Andersen (USGS/Cascades Volcano Observatory), Ellen Daley, and Janet Schaefer (DGGS/Alaska Volcano Observatory) improved the report. Any use of trade, firm, or product names is for descriptive purposes only and does not imply endorsement by the State of Alaska or U.S. Government.

REFERENCES

Andersen, D.J., Lindsley, D.H., 1985, New (and final!) models for the Ti–magnetite/ilmenite geothermometer and oxygen barometer: Eos, Transactions, American Geophysical Union, v. 66, p. 416.

Andrews, B.J., Gardner, J.E., Tait, S., Ponomareva, V.V., and Melekestsev, I.V., 2007, Dynamics of the 1800 ^{14}C yr BP caldera-forming eruption of Ksudach volcano, Kamchatka, Russia: AGU Geophysical Monograph Series v. 172, p. 325–342.

Bacon, C.R., 2000, Preeruptive volatiles in the most recent eruptions of Aniakchak volcano, Alaska [abs.]: Eos, Transactions, American Geophysical Union, v. 81, no. 48, p. 1,376–1,377.

———2002, Depths of magma reservoirs inferred from preeruptive dissolved volatiles in the most recent postcaldera eruptions of Aniakchak volcano, Alaska [abs.]: Eos, Transactions, American Geophysical Union, v. 83, no. 19, p. S378.

Bacon, C.R., Hirschmann, M.M., 1988, Mg/Mn partitioning as a test for equilibrium between coexisting Fe–Ti oxides: American Mineralogist, v. 73, p. 57–61.

Bacon, C.R., Neal, C.A., Miller, T.P., McGimsey, R.G., Nye, C.J., 2014, Postglacial eruptive history, geochemistry, and recent seismicity of Aniakchak volcano, Alaska Peninsula: US Geological Survey Professional Paper 1810.

Bacon, C. R., Neal, C.A., Nye, C.J., McGimsey, R.G., 1997, Pre-eruptive temperatures for postcaldera magmas of Aniakchak Volcano, Alaska: Eos, Transactions, American Geophysical Union, v. 78, p. 792–793.

Begét, J., Mason, Owen, Anderson, Patricia, 1992, Age, extent and climatic significance of the c. 3400 BP Aniakchak tephra, western Alaska, USA: The Holocene, v. 2, no. 1, p. 51–56

Best, M.G., Christiansen, E.H., 1997, Origin of broken phenocrysts in ash-flow tuffs: Geological Society of America Bulletin, v. 109, p. 63–73.

Browne, B.L., 2006, Investigating Magma Withdrawal Dynamics During Plinian Eruptions Through Mineral and Eruptive Stratigraphies: Examples From the Chemically Zoned 400 yr BP Eruption of Half Cone Volcano, Aniakchak National Park, Alaska: Eos, Transactions, American Geophysical Union, v. 87.

Browne, B.L., Becerra, R., Campbell, C., Saleen, P., and Wille, F.R., 2017, Quaternary basaltic volcanism in the Golden Trout Volcanic Field, southern Sierra Nevada, California: Journal of Volcanology and Geothermal Research, v. 343, p. 25–44.

Browne, B.L., Eichelberger, J.C., and Neal, C.A., 2004, The ~400 yr BP caldera-forming eruption of Half Cone Volcano, Aniakchak National Park, Alaska: General Assembly of the International Association of Volcanology and Chemistry of the Earth's Interior, p. 14–19.

Browne, B.L., Eichelberger, J.C., Patino, L.C., Vogel, T.A., Uto, K., and Hoshizumi, H., 2006, Magma mingling as indicated by texture and Sr/Ba ratios of plagioclase phenocrysts from Unzen volcano, SW Japan: Journal of Volcanology and Geothermal Research, v. 154, p. 103–116.

Browne, B.L., and Gardner, J.E., 2004, The nature and timing of caldera collapse as indicated by accidental lithic fragments from the AD~ 1000 eruption of Volcán Ceboruco, Mexico: Journal of Volcanology and Geothermal Research, v. 130, p. 93–105.

Carey, S., and Sparks, R.S.J., 1986, Quantitative models of the fallout and dispersal of tephra from volcanic eruption columns: Bulletin of Volcanology, v. 48, p. 109–125.

Coombs, M.L., Sisson, T.W., Bleick, H.A., Henton, S.M., Nye, C.J., Payne, A.L., Cameron, C.E., Larsen, J.F., Wallace, K.L., and Bull, K.F., 2009, Andesites of the 2009 eruption of Redoubt Volcano, Alaska: Journal of Volcanology and Geothermal Research, v. 259, p. 349–372.

Crandell, D.R., Miller, C.D., Glicken, H.X., Christiansen., R.L., and Newhall, C.G., 1984, Catastrophic debris avalanche from ancestral Mount Shasta volcano, California: Geology, v. 12, p. 143–146.

Degruyter, W., Huber, C., Bachmann, O., Cooper, K.M. and Kent, A.J., 2017, Influence of exsolved volatiles on reheating silicic magmas by recharge and consequences for eruptive style at Volcán Quizapu (Chile). Geochemistry, Geophysics, Geosystems, v. 18, p. 4,123–4,135.

DeMets, C., Gordon, R.G., Argus, D.F., and Stein, S., 1994, Effect of recent revisions to the geomagnetic reversal timescale on estimates of current plate motions: Geophysical Research Letters, v. 21, no. 20, p. 2,191–2,194.

Detterman, R.L., Case, J.E., Miller, J.W., Wilson, F.H., and Yount, M.E., 1996, Stratigraphic framework of the Alaska Peninsula: U.S. Geological Survey Bulletin 1969-A, 74 p.

Douglas, D., 1932, In the Land of the Thunder Mountains: Adventuring with Father Hubbard Among the Volcanoes of Alaska: New York: Brewer, Warren and Putnam, p. 4–5.

Dreher, S.T., 2002, The physical volcanology and petrology of the 3400 y BP caldera-forming eruption of Aniakchak volcano, Alaska: Fairbanks, University of Alaska Fairbanks, Ph.D. dissertation, 174 p.

Dreher, S.T., Eichelberger, J.C., and Larsen, J.L., 2005, The petrology and geochemistry of the Aniakchak caldera-forming ignimbrite, Aleutian arc, Alaska: Journal of Petrology, v. 46, p. 1,747–1,768.

Druitt, T.H., and Bacon, C.R., 1986, Lithic breccia and ignimbrite erupted during the collapse of Crater Lake Caldera, Oregon: Journal of Volcanology and Geothermal Research, v. 29, p. 1–32.

Dumond, D.E., 1979, People and pumice on the Alaska Peninsula, *in* Volcanic activity and human ecology, p. 373–92.

———1987a, The Eskimos and Aleuts (vol. 180): London, Thames and Hudson.

———1987b, Prehistoric human occupation in Southwestern Alaska: A study of resource distribution and site location: University of Oregon anthropological papers, no. 36, 190 p.

Evans, W.C., Bergfeld, D., Neal, C.A., McGimsey, R.G., Werner, C.A., Waythomas, C.F., Lewicki, J.L., Lopez, T., Mangan, M.T., Miller, T.P., Diefenbach, A., Schaefer, Janet, Coombs, M.L., Wang, B., Nicolaysen, K., Izbekov, P., Maharrey, Z., Huebner, M., Hunt, A.G., Fitzpatrick, J., and Freeburg, G., 2015, Aleutian Arc geothermal fluids: chemical analyses of waters and gases: U.S. Geological Survey Data release. dx.doi.org/10.5066/F74X55VB

Farmer, G.L., Glazner, A.F., and Manley, C.R., 2002, Did lithospheric delamination trigger late Cenozoic potassic volcanism in the southern Sierra Nevada, California?: Geological Society of America Bulletin, v. 114, p. 754–768.

Fierstein, Judy, and Nathenson, Manuel, 1992, Another look at the calculation of fallout tephra volumes: Bulletin of Volcanology, v. 54, p. 156–167.

First, E.C., Hammer, J.E., Ruprecht, P., and Rutherford, M., 2021, Experimental constraints on dacite magma storage beneath Volcán Quizapu, Chile: Journal of Petrology, v. 62, egab027.

Folch, Arnau, and Martí, J., 1998, The generation of overpressure in felsic magma chambers by replenishment: Earth and Planetary Science Letters, v. 163, p. 301–314.

Gardner, J.E., and Tait, S., 2000, The caldera-forming eruption of Volcan Ceboruco, Mexico: Bulletin of Volcanology, v. 62, p. 20–33.

George, Rhiannon, Turner, Simon, Hawkesworth, Chris, Bacon, C.R., Nye, Chris, Stelling, Pete, and Dreher, Scott, 2004, Chemical versus temporal controls on the evolution of tholeiitic and calc-alkaline magmas at two volcanoes in the Alaska–Aleutian arc: Journal of Petrology, v. 45, p. 203–219.

Ghiorso, M.S., and Evans, B.W., 2008, Thermodynamics of rhombohedral oxide solid solutions and a revision of the Fe–Ti two-oxide geothermometer and oxygenbarometer: American Journal of Science, v. 308, p. 957–103.

Glicken, Harry, 1996, Rockslide-debris Avalanche of May 18, 1980, Mount St. Helens Volcano, Washington: U.S. Geological Survey Open-File Report 96-677, 90 p., 5 plates.

Henn, Winfield, 1978, Archaeology on the Alaskan Peninsula: The Ugashik Drainage, 1973–1975: University of Oregon anthropological papers, no.14, p. 182.

Hildreth, Wes, and Fierstein, Judy, 2012, The Novarupta-Katmai eruption of 1912: Largest eruption of the twentieth century: Centennial perspectives: U.S. Geological Survey Professional Paper 1791, 259 p.

Hubbard, B.R., 1931, A world inside a mountain-Aniakchak, the new volcanic wonderland of the Alaska Peninsula, is explored: National Geographic v. 60, no. 3, p. 319–345.

Hubbard, B.R., 1932a, Aniakchak, the moon crater explodes: Saturday Evening Post, January 2, p. 6–7 and 68–71.

———1932b, Flying the moon craters: Saturday Evening Post, January 16, p. 30, 46, 48.

Huppert, H.E., Sparks, R.S.J., and Turner, J.S., 1982, Effects of volatiles on mixing in calc-alkaline magma systems: Nature, v. 297, p. 554–557.

Izbekov, P.E., Eichelberger, J.C., Patino, L.C., Vogel, T.A., and Ivanov, B.V., 2002, Calcic cores of plagioclase phenocrysts in andesite from Karymsky volcano: evidence for rapid introduction by basaltic replenishment: Geology, v. 30, p. 799–802.

Johnson, D.M., Hooper, P.R., and Conrey, R.M., 1999, XRF method XRF analysis of rocks and minerals for major and trace elements on a single low dilution Li-tetraborate fused bead: Advances in X-ray Analysis, v. 41, p. 843–867.

Kienle, Juergen, and Swanson, S.E., 1983, Volcanism in the eastern Aleutian Arc: late Quaternary and Holocene centers, tectonic setting and petrology: Journal of Volcanology and Geothermal Research, v. 17, no. 1–4, p. 393–432.

Larsen, J.F., 2006, Rhyodacite magma storage conditions prior to the 3430 y BP caldera-forming eruption of Aniakchak volcano, Alaska: Contributions to Mineralogy and Petrology, v. 152, p. 523–540.

Le Bas, M.J., LeMaitre, R.W., Streckeisen, A., Zanettin, B., and IUGS Subcommission on the Systematics of Igneous Rocks, 1986, A chemical classification of volcanic rocks based on the total alkali-silica diagram: Journal of Petrology, v. 27, no. 3, p. 745–750. doi.org/10.1093/petrology/27.3.745

Lepage, L.D., 2003, ILMAT: an Excel worksheet for ilmenite-magnetite geothermometry and geobarometry: Computers & Geosciences, v. 29, p. 673–678.

Le Maitre, R.W., 1989, A classification of igneous rocks and glossary of terms. Recommendations of the International Union of Geological Sciences Subcommission on the Systematics of Igneous Rocks, 193.

McGimsey, R.G., Waythomas, C.F., and Neal, C.A., 1994, High stand and catastrophic draining of intracaldera Surprise Lake, Aniakchak Volcano, Alaska, *in* Till, A.B., and Moore, T.E., eds., Geologic studies in Alaska by the U.S. Geological Survey, 1993: U.S. Geological Survey Bulletin 2107, p. 59–71.

Miller, T.P., and Smith, R.L., 1977, Spectacular mobility of ash flows around Aniakchak and Fisher calderas, Alaska: Geology, v. 5, p. 434–438.

———1987, Late Quaternary caldera-forming eruptions in the eastern Aleutian arc, Alaska Geology, v. 15, p. 173–176.

Miyashiro, Akhio, 1974, Volcanic rock series in island arcs and active continental margins American Journal of Science, v. 274, p. 321–355.

Nathenson, Manuel, and Fierstein, Judy, 2015, Spread sheet to calculate tephra volume for exponential thinning. vhub.org/resources/3716

Neal, C.A., McGimsey, R.G., Miller, T.P., Riehle, J.R., and Waythomas, C.F., 2001, Preliminary volcano-hazard assessment for Aniakchak Volcano, Alaska: U.S. Geological Survey Open-File Report 2000-519.

Nelson, S.T., and Montana, A., 1992, Sieve-textured plagioclase in volcanic rocks produced by rapid decompression: American Mineralogist, v. 77, p. 1,242–1,249.

Nicholson, R.S., Gardner, J.E., and Neal, C.A., 2011, Variations in eruption style during the 1931 AD eruption of Aniakchak volcano, Alaska: Journal of Volcanology and Geothermal Research, v. 207, p. 69–82.

Nowak, Michael, 1968, Archeological dating by means of volcanic ash strata: Eugene, Oregon, University of Oregon, Ph.D. dissertation, 413 p.

Nye, C.J., Neal, C.A., Miller, T.P., and McGimsey, R.G., 1995, Extreme tholeiitic to calcalkaline transition at Aniakchak volcano, east-central Aleutian arc [abs.]: Geological Society of America, Abstracts with Programs, v. 27, p. 69.

Nye, C.J., Miller, T.P., and Layer, P.W., 1997, Chemically and temporally distinct magma series at Aniakchak Volcano and the role of crustal mixing: Eos, Transactions, American Geophysical Union, v. 78, p. 816.

Nye, C.J., Scott, W.E., Neill, O.K., Waythomas, C.F., Cameron, C.E., and Calvert, A.T., 2017, Geology of Kasatochi volcano, Aleutian Islands, Alaska: Alaska Division of Geological & Geophysical Surveys Professional Report 123, 127 p., 1 sheet, scale 1:5,000. doi.org/10.14509/29718

Nye, C.J., Begét, J.E., Layer, P.W., Mangan, M.T., McConnell, V.S., McGimsey, R.G., Miller, T.P., Moore, R.B., and Stelling, P.L., 2018, Geochemistry of some Quaternary lavas from the Aleutian arc and Mt. Wrangell: Alaska Division of Geological & Geophysical Surveys Raw Data File 2018-1, 29 p. doi.org/10.14509/29843

Pearce, N.J., Westgate, J.A., Preece, S.J., Eastwood, W.J., and Perkins, W.T., 2004, Identification of Aniakchak (Alaska) tephra in Greenland ice core challenges the 1645 BC date for Minoan eruption of Santorini: Geochemistry, Geophysics, Geosystems, v. 5.

Pearce, T.H., Gorman, B.E., and Birkett, T.C., 1975, The TiO_2–K_2O–P_2O_5 diagram: a method of discriminating between oceanic and non-oceanic basalts: Earth and Planetary Science Letters, v. 24, p. 419–426.

Power, J.A., Stihler, S.D., White, R.A., and Moran, S.C., 2004, Observations of deep long-period (DLP) seismic events beneath Aleutian arc volcanoes; 1989–2002: Journal of Volcanology and Geothermal Research, v. 138, p. 243–266.

Putirka, Keith, Jean, Marlon, Cousens, Brian, Sharma, Rohit, Torrez, Gerardo, and Carlson, Chad, 2012, Cenozoic volcanism in the Sierra Nevada and Walker Lane, California, and a new model for lithosphere degradation: Geosphere, v. 8, p. 265–291.

Pyle, D.M., 1989, The thickness, volume and grainsize of tephra fall deposits Bulletin of Volcanology, v. 51, p. 1–15.

Riehle, J.R., Meyer, C.E., Ager, T.A., Kaufman, D.S., and Ackerman, R.E., 1987, The Aniakchak tephra deposit, a late Holocene marker horizon in western Alaska, *in* Hamilton, T.D., and Galloway, J.P., eds., Geologic studies in Alaska by the U.S. Geological Survey during 1986: U.S. Geological Survey Circular 998, p. 19–22.

Riehle, J.R., Dumond, D.E., Meyer, C.E., and Schaaf, J.M., 2000, Tephrochronology of the Brooks River Archaeological District, Katmai National Park and Preserve, Alaska: what can and cannot be done with tephra deposits: Geological Society, London, Special Publications, v. 171, no. 1, p. 245–266.

Reimer, P.J., Austin, W.E., Bard, E., Bayliss, A., Blackwell, P.G., Ramsey, C.B., Butzin, M., Cheng, H., Edwards, R.L., Friedrich, M. and Grootes, P.M., 2020. The IntCal20 Northern Hemisphere radiocarbon age calibration curve (0–55 cal kBP). Radiocarbon, 62(4), pp.725–757.

Ringsmuth, K.J., 2007, Beyond the Moon Crater Myth: A New History of the Aniakchak Landscape: A Historic Resource Study for Aniakchak National Monument and Preserve: Anchorage, Alaska: National Park Service, U.S. Dept. of the Interior, Research/Resources Management Report AR/CRR-2207-63, 262 p.

Schaefer, J.R., Scott, W.E., Evans, W.C., Jorgenson, J., McGimsey, R.G., and Wang, B., 2008, The 2005 catastrophic acid crater lake drainage, lahar, and acidic aerosol formation at Mount Chiginagak volcano, Alaska, USA: Field observations and preliminary water and vegetation chemistry results: Geochemistry Geophysics, Geosystems, v. 9, no. 7, 29 p.

Shennan, Ian, Bruhn, R.L., and Plafker, George, 2009, Multi-segment earthquakes and tsunami potential of the Aleutian megathrust: Quaternary Science Reviews, v. 28, p. 7–13.

Simmons, J.M., Cas, R.A.F., Druitt, T.H. and Folkes, C.B., 2016, Complex variations during a caldera-forming Plinian eruption, including precursor deposits, thick pumice fallout, co-ignimbrite breccias and climactic lag breccias: The 184 ka Lower Pumice 1 eruption sequence, Santorini, Greece: Journal of Volcanology and Geothermal Research, v. 324, p. 200–219.

Smith, W.R., 1925, Aniakchak Crater, Alaska Peninsula: U.S. Geological Survey Professional Paper 132-J, p. 139–149.

Sparks, R.S.J., Sigurdsson, Haraldur, and Wilson, Lionel, 1977, Magma mixing: a mechanism for triggering acid explosive eruptions: Nature, v. 267, p. 315–318.

Sparks, R.S.J., Wilson, L., and Hulme, G., 1978, Theoretical modeling of the generation, movement, and emplacement of pyroclastic flows by column collapse: Journal of Geophysical Research: Solid Earth, v. 83, p. 1,727–1,739.

Stormer, J.C., 1983, The effects of recalculation on estimates of temperature and oxygen fugacity from analyses of multicomponent iron-titanium oxides: American Mineralogist, v. 68, p. 586–594.

Stuiver, M., and Reimer, P. J., 1993, Extended 14C database and revised CALIB radiocarbon calibration program, Radiocarbon 35:215–230.

Sumner, J.M., Blake, S., Matela, R.J., and Wolff, J.A., 2005, Spatter: Journal of Volcanology and Geothermal Research, v. 142, p. 49–65.

Suzuki, Y.J., and Koyaguchi, T., 2012, 3-D numerical simulations of eruption column collapse: Effects of vent size on pressure-balanced jet/plumes: Journal of Volcanology and Geothermal Research, v. 221, p. 1–13.

Syracuse, E.M., and Abers, G.A., 2006, Global compilation of variations in slab depth beneath arc volcanoes and implications: Geochemistry, Geophysics, Geosystems, v. 7. doi.org/10.1029/2005GC001045

Tait, S., Jaupart, C., and Vergniolle, S., 1989, Pressure, gas content and eruption periodicity of a shallow, crystallising magma chamber: Earth and Planetary Science Letters, v. 92, p. 107–123.

Tramontano, S., Gualda, G.A., and Ghiorso, M.S., 2017, Internal triggering of volcanic eruptions: Tracking overpressure regimes for giant magma bodies: Earth and Planetary Science Letters, v. 472, p.142–151.

Valentine, G.A., and Connor, C.B., 2015, Basaltic Volcanic Fields, *in* Sigurdsson, Haraldur, Houghton, Bruce, McNutt, Steve, Rymer, Hazel, and Stix, John, eds., The encyclopedia of volcanoes (2nd ed): Academic Press, p. 423–439.

VanderHoek, Richard, 2009, The role of ecological barriers in the development of cultural boundaries during the later Holocene of the central Alaska Peninsula: Urbana, Illinois, University of Illinois at Urbana-Champaign, Ph.D. dissertation, 413 p.

VanderHoek, Richard, and Myron, R., 2004, An archaeological overview and assessment of Aniakchak National Monument and Preserve: U.S. National Park Service Research/Resources Management Report AR/CRR-2004-47.

VanderHoek, Richard, and Nelson, R.E., 2007, Ecological roadblocks on a constrained landscape: The cultural effects of catastrophic Holocene volcanism on the Alaska Peninsula, southwest Alaska: Walnut Creek, CA, Left Coast Press.

Venezky, D.Y., and Rutherford, M.J., 1999, Petrology and Fe–Ti oxide reequilibration of the 1991 Mount Unzen mixed magma: Journal of Volcanology and Geothermal Research, v. 89, p. 213–230.

Viccaro, Marco, Barca, Donatella, Bohrson, W.A., D'Oriano, Claudia, Giuffrida, Marisa, Nicotra, Eugenio, and Pitcher, B.W., 2016, Crystal residence times from trace element zoning in plagioclase reveal changes in magma transfer dynamics at Mt. Etna during the last 400 years: Lithos, v. 248, p. 309–323.

Viccaro, Marco, Giacomoni, P.P., Ferlito, Carmelo, and Cristofolini, Renato, 2010, Dynamics of magma supply at Mt. Etna volcano (Southern Italy) as revealed by textural and compositional features of plagioclase phenocrysts: Lithos, v. 116, p. 77–91.

Walker, G.P.L., 1985, Origin of coarse lithic breccias near ignimbrite source vents: Journal of Volcanology and Geothermal Research, v. 25, p. 157–171.

Waythomas, C.F., and Neal, C.A., 1998, Tsunami generation by pyroclastic flow during the 3500-year B.P. caldera-forming eruption of Aniakchak volcano, Alaska: Bulletin of Volcanology, v. 60, no. 2, p. 110–124.

Waythomas, C.F., Walder, J.S., McGimsey, R.G., and Neal, C.A., 1996, A catastrophic flood caused by drainage of a caldera lake at Aniakchak Volcano, Alaska, and implications for volcanic hazards assessment: Geological Society of America Bulletin, v. 108, no. 7, p. 861–871.